UNIVERSITEIT GENT

FACULTY OF SCIENCES

Department of Analytical Chemistry
Research group Atomic and Mass Spectrometry

Method development for Li isotopic analysis via multi-collector ICP-mass spectrometry application to Cretaceous-Paleogene boundary clays from the Umbria-Marche sequence.

Thesis submitted to obtain
the degree of Master of Science in Chemistry by

Tom Croymans-Plaghki

Academic year 2012 - 2013

Promoter: prof. dr. Frank Vanhaecke
Copromoter: prof. dr. Philippe Claeys
Supervisor: Karen Van Hoecke

UNIVERSITEIT GENT

FACULTY OF SCIENCES

Department of Analytical Chemistry
Research group Atomic and Mass Spectrometry

Method development for Li isotopic analysis via multi-collector ICP-mass spectrometry application to Cretaceous-Paleogene boundary clays from the Umbria-Marche sequence.

Thesis submitted to obtain
the degree of Master of Science in Chemistry by

Tom Croymans-Plaghki

Academic year 2012 - 2013

Promoter: prof. dr. Frank Vanhaecke
Copromoter: prof. dr. Philippe Claeys
Supervisor: Karen Van Hoecke

Life is no straight and every corridor along
which we travel free and unhampered,
but a maze of passages,
through which we must seek our way,
lost and confused, now and again
checked in a blind alley.

But always, if we have faith,
God will open a door for us,
Not perhaps one that we ourselves
would ever have thought of,
But one that will ultimately
prove good for us.

A. J. Cronin

Dankwoord – Acknowledgement

Gedurende de verschillende stappen van mijn Masterscriptie hebben veel mensen mij gesteund elk op hun eigen manier.

Om te beginnen wil ik graag Prof. Dr. Frank Vanhaecke en Prof. Dr. Philippe Claeys bedanken. De bovenstaande quote is een verwijzing naar de zoektocht en belevenis die is voorafgegaan aan enerzijds het vinden van een thesisonderwerp en anderzijds naar het vinden van een buitenlandse ervaring die ik graag wenste op te doen. Het onderzoeksonderwerp heeft mij gedurende de hele rit uitermate geïnteresseerd. Het verblijf aan de universiteit van Cambridge was een impressionante ervaring die een blijvende indruk op mij heeft achtergelaten. Bedankt voor jullie inzet, motivatie en vertrouwen.

Verder wil ik Prof. Dr. Karel Strijckmans bedanken voor de infrastructuur en de goede leiding van de vakgroep.

Een hele grote dankjewel aan Karen. Ze heeft mij de afgelopen maanden ontzettend veel bijgeleerd. Bedankt om altijd klaar te staan voor advies en raad. Bedankt voor de leuke tijden, met als hoogtepunt ons verblijf aan de universiteit van Cambridge samen met Sambuddha. Wat zeker niet in de vergetelheid mag geraken is de toffe momenten die we beleefd hebben met de software van ICP-OES en het verplaatsen van de centrifuge uit de “sauna” ;) .
Hartelijk bedankt voor alles, Karen!

As mentioned previously, during my Master's thesis I enjoyed a two-week stay in Cambridge. Sambuddha was the best host & mentor who taught me all the tricks to successfully separate lithium from sodium by column chromatography. In addition to all the work in the lab we also had a lot of good non-scientific moments, mostly at lunch & dinner. The very best of these was when we were able to clear our heads and eat some delicious blueberry or chocolate muffins.

Daarnaast een dankwoord aan alle collega’s van de S12 voor de leuke werkomgeving en hulp doorheen het gehele jaar. Met de medestudenten heb ik een zeer toffe tijd beleefd. De XMI groep wil ik bedanken voor het computeradvies. Rosie, bedankt voor de overheerlijke en leuke tea times.

Verder wil ik ook graag Evelyn bedanken. De lekkere maaltijden als ik s’avonds laat in Antwerpen toekwam vielen altijd in de smaak. Maar waar ik haar vooral voor wil prijzen is haar geduld, dat telkens op de proef gesteld werd wanneer ik zei: “ ik ga dit nog “snel” eventjes afwerken”.

Last but not least wil ik mijn moeder bedanken voor ik het verkrijgen van de opportuniteit om gedurende vijf jaar van deze interessante studie te hebben mogen genieten. Daarnaast wil ik haar bedanken voor alle goede zorgen en steun doorheen deze academisch studiecarrière.

Table of contents

1. Introduction and aims

1.1 Cretaceous-Paleogene boundary

Two large asteroids collided in the Main Asteroid belt between Mars and Jupiter approximately 160 million years ago [1–3]. The collision of these two bodies with diameters of 60 and 170 km produced over 1000 of fragments with a diameter of more than 1 km. Work done by Bottke et al. (2007) [3] and Reddy et al. (2013) [4] showed that one of these fragments was the 10 km diameter Chicxulub projectile which collided with our planet 66 million years ago [5]. The impact of this collision changed the geological history of planet Earth significantly. The impact and its effects caused one of the largest mass extinctions on planet Earth, including the demise of the dinosaurs [1–3]. This impact reshaped the global ecosystem and marked the start of the Paleogene period and the end of the Cretaceous period. This chronological transition is called the K/Pg boundary. The 180 km diameter Chicxulub crater located on the Yucatán peninsula (Mexico) still witnesses to this event today. However, to date, the severity of indirect effects of the meteorite impact on, e.g., continental denudation, deforestation and continental weathering on a global scale are largely unknown.

1.2 Introduction to stable isotope research

Determination of the variations in the isotopic composition of elements such as H, Li, B, C, N, O, Mg, Si, S, Cl, Ar, K, Ca, V, Fe, Cu and Zn has proven its value in all branches of geological and space sciences [6,7]. These isotope ratios form the subject and the tool in research regarding many scientific hypotheses, e.g., in paleoclimate research. Abrupt temperature changes on Earth were, e.g., revealed based on ∂^{15}N and ∂^{40}Ar determination [8].

1.3 Li isotope ratio as a proxy for weathering

Lithium (Li) has two stable isotopes: ^{6}Li (~7.5 %) & ^{7}Li (~92,5 %) [9]. The relative mass difference between these two isotopes is approximately 16 %. The lithium isotope ratio, expressed as ∂^{7}Li (‰), in geological samples acts as a promising proxy to answer questions in Earth and planetary sciences [10–13]. ∂^{7}Li is expressed as the relative deviation from L-SVEC standard (expressed in per mil) as shown in equation 1.1.:

$$\partial^{7}Li\ (‰) = \left\{\left[\frac{\left(\frac{^{7}Li}{^{6}Li}\right)_{sample}}{\left(\frac{^{7}Li}{^{6}Li}\right)_{standard}}\right] - 1\right\} \text{x } 1000 \qquad \text{Eq. 1.1.}$$

Lithium is known as an indicator for weathering processes of different kinds of rocks, as these processes are often accompanied by fractionation between the lithium isotopes [9,10,14–16]. Weathering is a surface process, which breaks down rocks through physical and chemical influences. More intensive weathering is linked to larger negative shifts in ∂^{7}Li values, because the heavier ^{7}Li

isotope is preferably lost during weathering, while the lighter ^{6}Li isotope is preferably retained by the mineral undergoing the weathering process [15].

1.4 Research topic and experimental approach

This work focuses on lithium isotopic analysis of geological samples via multi collector - inductively coupled plasma - mass spectrometry (MC-ICP-MS).

The main aim was to determine the lithium isotopic composition of clay fractions extracted from limestone deposits. The limestone samples originated from the Umbria-Marche region (Italy), which are linked in age to the Chicxulub impact event.

A possible link between the impact of the extra-terrestrial body and a shift in ∂^{7}Li values was investigated. The Chicxulub impact suddenly changed the global ecosystem leading to a(n) (in)direct perishing of the fauna and flora living at the time. A large deforestation took place, which potentially led to increased weathering. Hence, the goal of this thesis was to test the hypothesis of increased global weathering across the K/Pg boundary, using the lithium isotope ratio proxy method. A significant negative ∂^{7}Li shift at the K/Pg boundary would serve as a criterion to validate the hypothesis.

Since accurate and precise determination of lithium isotope ratios is crucial, MC-ICP-MS was selected as analytical technique. This technique was developed in the nineties of the previous century. It is able to determine isotope ratios of a broad range of elements with high accuracy and precision. MC-ICP-MS has the advantage to be less time-consuming than thermal ionization mass spectrometry (TIMS) [6]. In addition, the ICP source provides higher ionization efficiency, such that elements that are difficult to be measured by TIMS can be analysed in a straightforward way, e.g., Hf [17]. The simultaneous measuring of the different ion beams in a MC-ICP-MS allows the noise originating from the ICP source to be compensated for [17,18].

However, for accurate and precise determination of lithium isotope ratios with MC-ICP-MS, the analyte is preferably introduced as acidic solution only containing the analyte and the counter ion, free from any matrix elements. Hence, development of a suited sample preparation method was an important part of this project. Individual steps consisted of (1) isolation of the clay fractions from the limestone deposits, (2) acid digestion of the clay fraction, (3) isolation of lithium from its clay matrix using ion exchange chromatography, aiming at quantitative recovery, and (4) evaporation and final re-dissolution in diluted acid.

In addition, the optimization of lithium isotope ratio determination with MC-ICP-MS was an equally important goal of this research project. A series of experiments aimed at (1) optimization of the measurement conditions, (2) evaluation of different correction methods for mass discrimination, (3) selection of appropriate amplifiers for the Faraday cup detector configuration and (4) determination of maximum allowable sodium (Na) concentration in the final sample solutions.

Finally, a depth profile of lithium isotope ratios across a 10 m limestone deposit section from Umbria-Marche was composed. In cooperation with geologists, it was attempted to discuss the results obtained in light of the paleo-characteristics of the Umbria-Marche samples.

Figure 1.1 modified from Don DAVIS/NASA via [19]: an artist's impression of the impact of the extra-terrestrial object (with a diameter of 10 km) leading to the Chicxulub crater.

2. Instrumentation

Six large segments can be distinguished in an ICP-MS instrument: (1) the sample introduction system, (2) the ionization source, (3) the interface, (4) the lens system, (5) the mass spectrometer and (6) the detector. To obtain valuable results, these segments have to work as one harmonic entity. Each of the numbered segments mentioned above is shown in Figure 2-1.

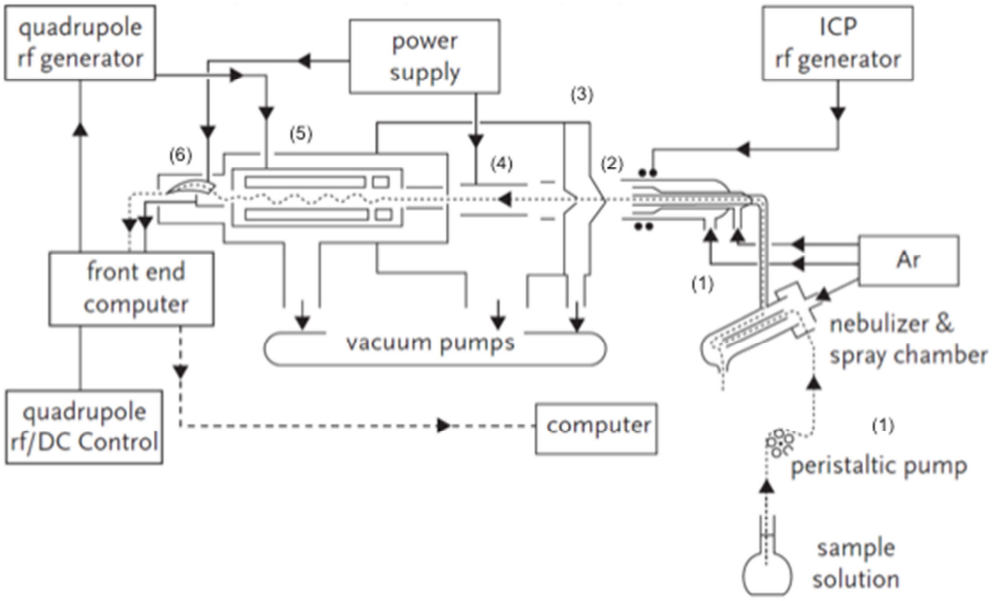

Figure 2-1 Modified from Vanhaecke (2012) [23]: schematic overview of an ICP-MS instrument; the instrument shown is a quadrupole-based instrument (Q-ICP-MS).

2.1. Sample introduction system

The sample introduction system transports the sample or a representative part of it to the ionization source. Different types of introduction systems exist. The standard sample introduction system consists of three major parts through which the liquid sample passes chronologically: (1) pump, (2) nebulizer and (3) spray chamber. Two important functions of the introduction system are: (1) aerosol generation and (2) selection of droplets.

A constant introduction rate of liquid sample into the system, is regulated by a peristaltic pump [20]. The liquid flow is introduced into a pneumatic nebulizer [20]. The pneumatic nebulizer consists of a combination of a liquid sample capillary and an argon gas tube and creates an aerosol. The gas tube becomes narrow towards the end [20]. Two main types of pneumatic nebulizers exists: (1) the cross-flow and (2) the concentric nebulizer, both shown in §9.2 [20]. In a cross-flow nebulizer, the liquid sample capillary tube and argons gas tube are placed perpendicularly, while, on the other hand, in a concentric nebulizer both tubes run parallel [20]. In both cases, the aerosol is generated by interaction with a high speed argon gas flow, which disperses the liquid into tiny aerosol droplets [20]. Also a micro-concentric design exists, which requires lower sample introduction flow rates *i.e.* 0.1 ml/min instead of 1 ml/min [20]. The aerosol droplets generated are not uniform in size, with droplets up to

100 µm. To select only the smallest droplets and thereby prevent overload of the plasma, a spray chamber is placed after the nebulizer [21]. In this way, the overall sample introduction efficiency is only 1-2 % [20]. To increase the thermal stability, reduce oxide formation and allow aspiration of volatile organic solvents, the spray chamber is sometimes cooled by an external cooling element, typically to 2-5°C [20].

A variety of spray chamber types exists. The most widely used are the double-pass Scott-type spray chamber and the cyclonic spray chamber. Another type of spray chamber offering improved stability consists of cyclonic and Scott-type sub-units [20]. In the cyclonic part, centrifugal forces, originating from the tangential flow of aerosol and argon gas, remove the larger droplets [20]. Smaller droplets move along with the gas [20]. The gas flow proceeds through the central tube of the double-pass Scott-type segment. The smaller droplets are separated from the larger ones by gravity, as the larger droplets collide with the wall of the central tube or are removed by gravitational settling [20], such that only the sufficiently small particles are transferred towards the ICP source [20]. Both spray chambers are shown separately in § 9.2.

2.2. Ionization source

2.2.1. Ionization source

The function of the ionization source is to ionize the analyte elements. The ionization source of an ICP-MS is an inductively coupled plasma. Other ionization sources exist, such as a heating filament, used in TIMS, a direct current plasma (DCP) or a microwave-induced plasma (MIP) [22].

The ionization source consists of a (1) plasma torch, (2) radiofrequency (RF) coil and (3) power supply. The plasma torch consists of three concentric tubes: (1) sample injector tube, (2) middle tube and (3) outer tube. Argon gas flows through each of these concentric tubes at different flow rates. Each argon flow has a different function within the torch. The most inner tube, called the sample injector, contains the argon nebulizer gas, which carries the sample aerosol [22–24]. The nebulizer gas originates from the spray chamber flows at ~1 l/min and punctures a channel into the plasma [22–24]. Within this channel, the analyte ionization takes place [23]. Between the sample injector and the middle tube, the auxiliary gas flows at a rate of ~1 l/min. The plasma position, relative to the torch and the coil, can be adapted by modifying this flow rate [22,23]. Between the middle tube and the outer tube, the plasma gas flows tangentially at a flow rate between 12 and 20 l/min [22,23]. The function of the plasma gas is to maintain the plasma (discussed further in §2.2.2.) and to form a thermal barrier between the torch and the plasma. Figure 2-2 shows a schematic overview of a quartz torch.

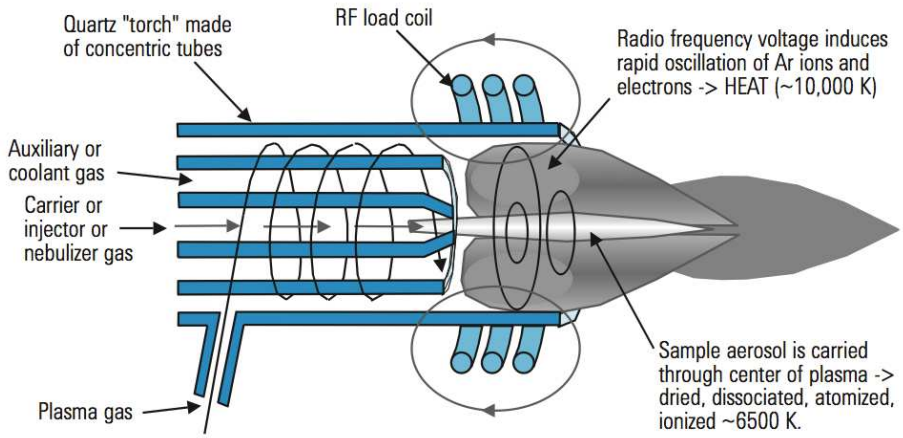

Figure 2-2 from Agilent Technologies (2005) [26]: schematic presentation of a quartz.

The tubes are typically manufactured from quartz, although the sample injector can also exist of alumina, platinum or sapphire, depending on the sample characteristics. Measurements in HF solution, e.g., require a sapphire sample injector [22].

The RF coil, which mostly consists of copper, is supplied by RF power by a generator [22]. An alternative current, with the same frequency as the RF generator, oscillates through the coil [22,23]. This oscillation generates an electromagnetic field at the top of the torch [22,23].
In most ICP-MS systems, the RF generator works with frequencies of 27.12 or 40.68 MHz and output powers between 1000 and 2000 W [25]. These two frequencies don't interfere with frequencies for other applications [22].

2.2.2. Plasma Formation

Uncharged plasma gas is introduced tangentially into the outer tube of the torch, while the radio frequent coil generates a strong electromagnetic field varying at RF frequency [22,23]. A tesla generator creates a high voltage spark [22,23]. Some electrons of this spark are able to ionize a small amount of argon atoms, each releasing an additional electron [22,23]. The magnetic field accelerates both the electrons and positively charged argon atoms, but due to the lower mass of the electrons, the latter acquire a higher acceleration [22]. The accelerated electrons undergo new collisions with argon atoms, giving rise to new electrons and argon ions through the process of electron impact ionization: $Ar + e^- \rightarrow Ar^+ + 2e^-$ [23]. These new electrons, on their turn, are also accelerated and the process sustains itself [22,23]. This process continues as long as RF energy is added to the load coil and new argon atoms are supplied. Eventually, the plasma reaches a steady state when the amount of electrons supplied is equal to the amount of electrons leaving the system [22,23]. The motion of the free electrons heats up the argon gas reaching a temperature up to ~10000 K, although temperatures vary greatly according to the exact position in the plasma [24].

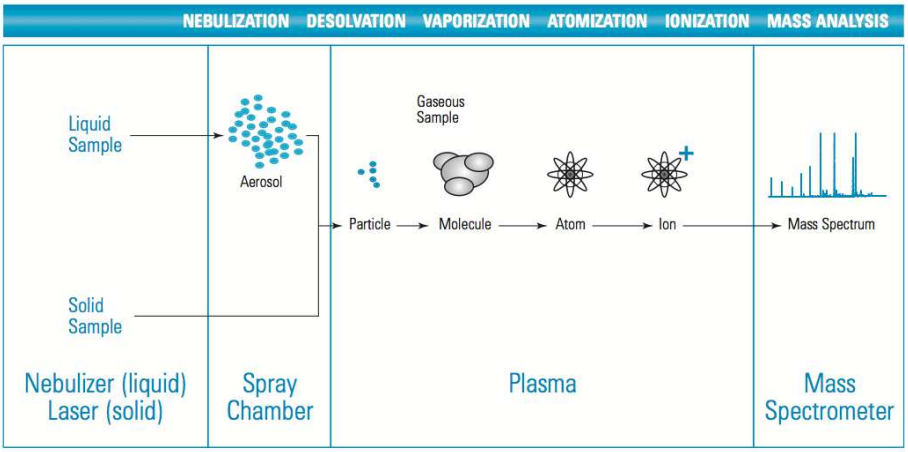

Figure 2-3 from Agilent Technologies (2005) [26]: different steps occurring within the central channel of the plasma.

The nebulizer gas containing the sample aerosol is introduced into the plasma, and the sample aerosol is desolvated, the molecules vaporized and atomized and the atoms formed ionized; droplets of ≤ 10 µm are processed efficiently [21]. This process is shown in Figure 2-3.

Often, the torch is equipped with a platinum guard electrode, which is able to reduce the kinetic energy spread by capacitive decoupling [24].

A typical ionization temperature of 7500 K is able to ionize most elements with high efficiency, making the ICP source suitable for multi-element analysis [23].

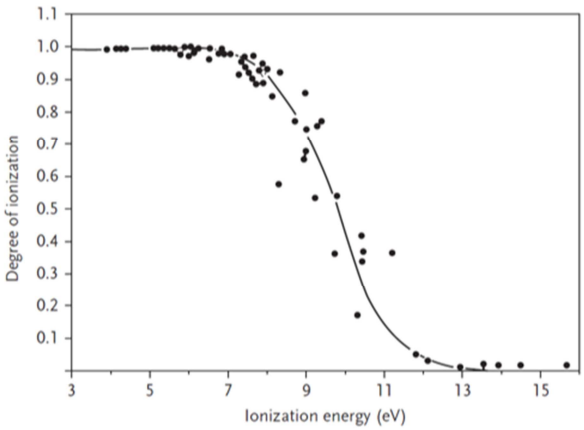

Figure 2-4 from Taylor (1992) [27]: degree of ionization in an ICP as a function of the element's ionization energy.

2.3 Interface

The interface region plays a crucial role in the transfer of ions from the plasma, operated at atmospheric pressure, to the mass spectrometer, operated under high vacuum conditions, 10^{-5} - 10^{-9} mbar [23,28]. An interface is built in-between the plasma and mass spectrometer to reduce the pressure stepwise. The interface region contains two cones: (1) the sampler cone and (2) the skimmer cone. These cones have small orifices, typically 0.8-1.2 mm and 0.4-0.8 mm, respectively [28]. The cones are manufactured from Ni or Pt [24].

The ion beam, generated by the plasma, first passes through the sampler cone and then through the skimmer cone [28]. Between these two cones, a pressure of 1-3 mbar is maintained by vacuum pumps [24]. After the skimmer cone, fore vacuum conditions of 10^{-4} mbar are prevalent [24].

Supersonic expansion of the ion beam takes place between the two cones. Supersonic expansion is the phenomenon that occurs when an ion beam passes through the orifice of the sampler cone towards vacuum conditions. During this expansion, the chance of recombination between an electron and an ion is strongly reduced, and a representative fraction of the sample, ionized in the plasma, passes through the skimmer cone aperture [23].

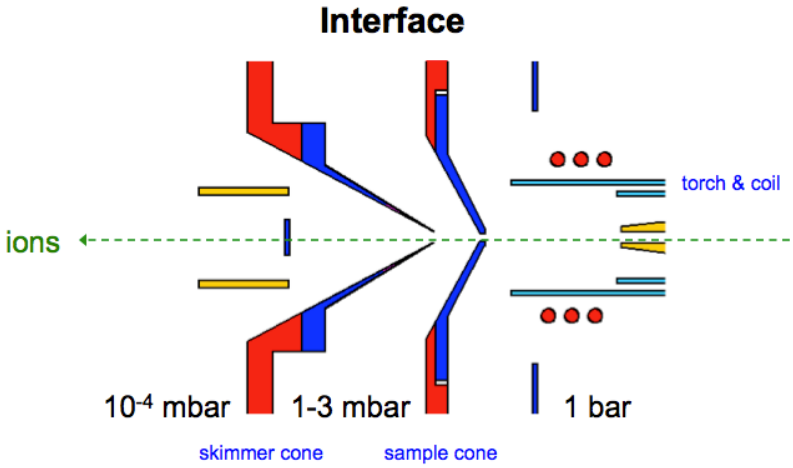

Figure 2-5 from Bouman (2008) [24]: schematic overview of the interface region.

2.4. Ion focusing system

An electrostatic lens, placed after the interface system, selectively attracts the positively charged ions [29]. In addition to the extraction lens, the ion focusing system consists of a series of electrostatic lenses. This system is located between the skimmer cone and the mass spectrometer (Figure 2-1). The ion focusing system consists of metallic parts maintained at a certain voltage. The main functions of the focusing system are to (1) efficiently transport ions to the mass spectrometer and (2) to remove particles other than ions before reaching the mass spectrometer.

After the interface, there are still some neutral species and photons present, which can elevate the background signal and cause signal instability [29]. Removal of these interfering particles can be achieved in different ways. A first approach is to place the ion extraction lens slightly off axis. Under these conditions, the positive ions are deflected by the presence of the extraction lens and are able to reach the mass spectrometer, while the other particles are not deflected and therefore don't reach the mass spectrometer [29]. A second approach is a metal disk. The ions are deflected around the disk, while the other particles collide with the disk and are physically stopped [29].

In addition, the lens system needs to compensate for space-charge effects. After the skimmer cone, a pressure drop results in a diffusion of electrons out of the ion beam, while the extraction lens electrostatically attracts the positively charged species [29]. Consequently, space charge effects occur,

i.e. positively charged particles repel each other, resulting in a favoured preservation of high-mass elements in the central ion beam [29]. The lens system focuses the beam to compensate for these repelling Coulomb forces [29].

2.5 Mass spectrometer

The mass spectrometer selects ions according to their mass-to-charge ratio and passes them towards the detector. The mass spectrometer typically operates under high vacuum conditions [23].
In the following paragraphs, the concepts of mass resolution and mass range are explained first, followed by the basic principles of different types of mass spectrometers.

2.5.1. Mass resolution

Mass resolution, R, expresses the extent to which two peaks are separated from each other in the mass spectrum [23]. Higher R values indicate that two peaks are more separated. The concept of mass resolution can be approached in two different ways, *i.e.* (1) an experimental approach and (2) a theoretical approach. The first approach calculates the resolution based on an experimentally observed peak. This is accomplished via the equation given below:

$$R = \frac{m}{\Delta m} \qquad \text{Eq. 2.1.}$$

Δm is the width of the peak at 5 % peak height at mass m.

The second approach uses the masses of two peaks, equal in intensity, to calculate which resolution is required to separate them [23]. A threshold value of 10 % of the maximum peak height intensity is set. The peaks are considered to be separated if the height of the valley between the two peaks is at or below this threshold value [23]. This approach is called the 10 % valley definition [23]. The corresponding calculation is illustrated by Eq. 2.2.

$$R = \frac{\left(\frac{m_1 + m_2}{2}\right)}{m_2 - m_1} \qquad \text{Eq. 2.2.}$$

Three modes of mass resolution can be achieved: low (300-400), medium (3000-4000) and high (≥10000) [30].

2.5.2. Mass range

The mass range of interest within an ICP-MS instrument ranges between 0 and 250 amu, as only elemental ions are studied [23].

2.5.3. Quadrupole filter

A quadrupole filter is a mass spectrometer consisting of four cylindrical or hyperbolic rods made from a conductive material [23,31]. The rods are all of the same length and diameter, typically 15-20 cm and 1 cm, respectively [31].

The rods are placed two by two, opposite to each other, forming two pairs of electrically connected rods [23]. A positive voltage (+ U), resulting from a direct current (DC) power source, in combination with an alternating current (AC) voltage is applied to the first pair. The ions will be focused towards the axis of the quadrupole by the applied positive voltage. The AC will defocus the ions for half a period and refocus them during the second part of the period. Lighter ions are more influenced by the AC component and will therefore be defocused, whereas heavier ions are less influenced by the AC component and stay focused as a result of the applied positive DC voltage (+ U). A negative DC voltage (- U), of the same magnitude as applied onto the first pair, in combination with an AC voltage, shifted 180° with respect to that applied onto the first pair, is applied to the second pair [23]. Both heavy and light ions will be deflected through the influence of the applied negative voltage [23]. Nevertheless, light ions are able to pass through the mass filter as their deflections are sufficiently corrected for the influence of the AC component [23]. Therefore, the rods operated with a positive voltage act as a high mass filter, whereas the rods operated with a negative voltage act as a low mass filter [23]. By changing the voltages, only ions with a certain mass-to-charge ratio are able to pass the quadrupole filter towards the detector [23]. The deflected ions leave the quadrupole filter through one of the openings, or they collide against one of the rods.

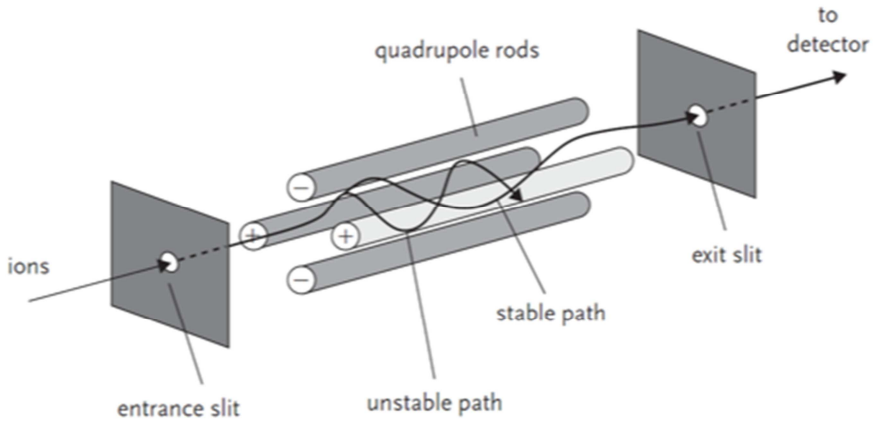

Figure 2-6 from Gates (2013) [86] : stable and unstable ion paths in a quadrupole.

2.5.5. Sector field mass spectrometers

These types of mass spectrometers consist of a magnetic sector and an electrostatic sector. The magnetic sector separates the ions according to their mass-to-charge ratio. The electrostatic sector selects the ions by their kinetic energy. Both sectors are discussed below and shown in figure 2.7.

2.5.5.1. Electromagnetic sector

Before entering the mass spectrometer, the ions are accelerated through an entrance slit with a potential difference V [V] [23]. The accelerated ions are subsequently introduced into a magnetic field [23]. The field lines of the magnetic field are perpendicularly oriented to the plane in which the ions enter the mass spectrometer [23]. Due to the Lorentz force, incoming ions are forced to move in a circular path [23]. This is shown in Eq. 2.3.

$$F = \frac{mv^2}{r} = qvB \qquad \text{Eq. 2.3.}$$

F [N] is the force exerted on the ion, m [kg] is the ion mass, v [m s^{-1}] is the velocity, r [m] is the radius of the circular path along which the ion moves, q [C] is the ion charge and B [T] is the magnetic field.

The radius can be expressed as:

$$r = \frac{mv}{qB} \qquad \text{Eq. 2.4.}$$

The kinetic energy [J] the ion obtained upon acceleration is expressed by:

$$E_{kin} = \frac{1}{2}mv^2 = qV \qquad \text{Eq. 2.5.}$$

The velocity of the ion is thus given by:

$$v = \sqrt{\frac{2qV}{m}} \qquad \text{Eq. 2.6.}$$

Substituting Eq.2.6. in Eq.2.4. gives:

$$r = \frac{\sqrt{2Vm}}{B\sqrt{q}} \qquad \text{Eq. 2.7.}$$

The radius of an ion can be expressed as a function of its mass. By keeping the magnetic field and the applied potential difference at the entrance slit constant, ions can be separated according to their mass–to-charge ratio, as they move according to a different radius in the magnetic field.

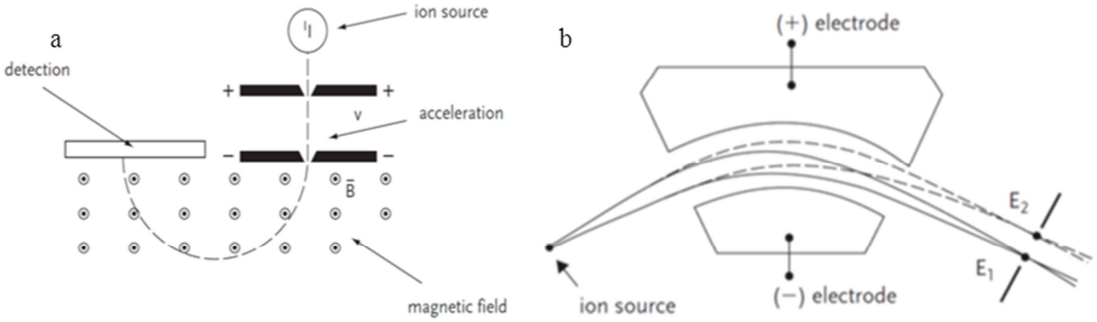

Figure 2-7: (a) from Vanhaecke (2012) [23]: process of an ion deflected in an electromagnetic sector (b) from Vanhaecke (2012) [23]: process of an electrostatic sector filtering ions with different kinetic energy.

An exit slit is placed after the mass spectrometer. The width of the slit determines the transmission efficiency and the resolution of the mass spectrometer. The strength of the magnetic field, B, and potential difference, V, are adapted for selecting the desired mass-to-charge ratio of the ion [23].

2.5.5.2. Electrostatic sector

Ions entering the magnetic sector can show a small spread in their kinetic energy [23]. A lighter ion with a higher kinetic energy is able to show the same radius as a heavy ion with lower kinetic energy, and vice versa. The presence of an electrostatic sector counteracts this effect by focusing the ions according to their kinetic energy independently of their mass-to-charge ratio [23]. The ions move through two bended electrodes with the same, though opposite, potentials [23]. Under influence of the electric field, the ions are forced to follow a circular path [23].

$$F = \frac{mv^2}{r} = qE \qquad \text{Eq. 2.8.}$$

E is the strength of the electric field.

Taking the kinetic energy into account, the radius of the ions throughout the electrostatic sector is described by:

$$r = \frac{mv^2}{qE} = \frac{2\,E_{kin}}{qE} \qquad \text{Eq. 2.9.}$$

Hence, ions with the same kinetic energy will be focused in one point [23].An exit slit is placed after the electrostatic sector. The width of the slit determines the transmission efficiency of the ions and the allowable spread in kinetic energy [23].

A magnetic sector in combination with an electrostatic sector has an improved resolution compared to mass separation with a magnetic sector only [23]. Certain combinations of the magnetic and electrostatic sector, which meet specific requirements both in combination of these sectors and in these sectors individually, are called double focusing setups [23]. Different double focusing geometries exist; two of them are described further [23]. A double focusing geometry realises both energy focusing and directional focusing, as a consequence ions of the same mass-to-charge ratio,

showing a spread in kinetic energy and/or direction, are focused into one point [23]. This double focusing setup allows the use of a wider slit between the magnetic and electrostatic sector without largely compromising ion transmission efficiency and still attaining high mass resolution [23].

2.5.5.3. Double-focusing geometries

Different double-focusing setups can constructed [23]. In Nier-Johnson geometry, the electrostatic sector is placed in front of the magnetic sector [23]. This geometry is used in MC-ICP-MS [23]. Only a part of the mass spectrum can be measured simultaneously in this setup [23]. In reverse Nier-Johnson geometry, the magnetic sector is placed in front of the electrostatic sector [23]. This geometry is mostly used in single-collector (SC) ICP-MS [23].

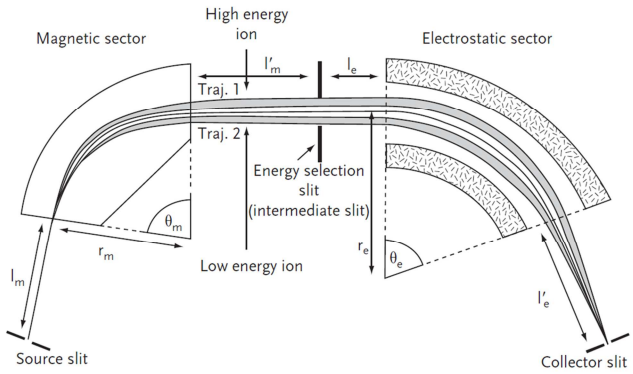

Figure 2-8 from Vanhaecke (2012) [23]: reverse Nier-Johson geometrie.

2.6. Detector

Subsequently, the separated ions have to be detected. In the following paragraphs, the electron multiplier and Faraday cup are discussed. Finally the detector output is further handled by the software of the instrument.

2.6.1. Electron multiplier

When an ion strikes the surface of an electron multiplier, one or more electrons are released [23]. A potential difference across the electron multiplier attracts the electrons towards the end of the detector. As the electron moves towards the end of the detector, it collides several times with the surface of the electron multiplier [23]. With each of these collisions, more electrons are released from the surface [23]. The incoming ion generates an "avalanche" of 10^7 - 10^8 electrons, which can be converted into a measurable electrical pulse [23]. The detector can be used in two modes: (1) pulse counting mode and (2) analog mode [18].

In pulse counting mode, every ion is counted individually [18]. Every counted ion requires a certain treatment time, during which no other ions can be detected. This period is called the dead time [18]. A correction is required for the lost measurement time [18].

In analog mode, the electron multiplier is used as an analog multiplier [18].

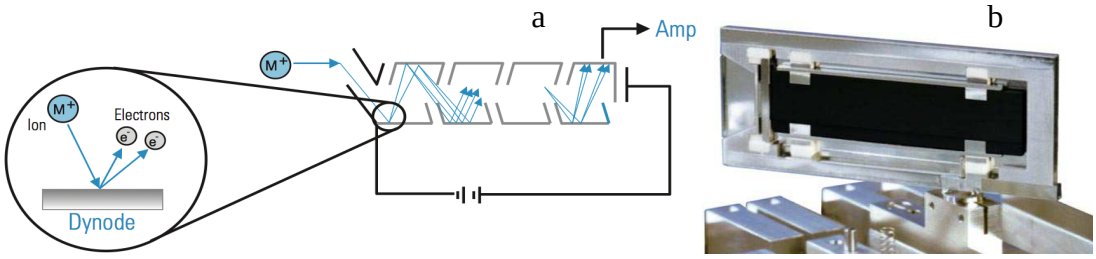

Figure 2-9 (a) from Agilent technologies (2005) [26]: electron multiplier (b) from Bouman (2008) [24]: Faraday cup.

2.6.2. Faraday cup

A Faraday cup is a metal or graphite electrode connected to ground via a high ohmic resistor [32]. An impacting ion is neutralized by electrons flowing through the high ohmic resistor, leading to a measurable potential difference over the resistor [23]. This potential difference has to be amplified, as discussed in §5.3. [23]. Faraday cups are less sensitive than the electron multipliers described above and hence, require higher ion currents [32]. Faraday cups have a longer lifetime than electron multipliers and do not suffer from dead time [32].

2.7. Instruments used during this work.

During this work, three different types of ICP-MS instrumentation were used: (1) quadrupole-based inductively coupled plasma - mass spectrometry (Q-ICP-MS), (2) single-collector sector-field inductively coupled plasma - mass spectrometry (SC-ICP-MS) and (3) multi-collector sector-field inductively coupled plasma - mass spectrometry (MC-ICP-MS).
In addtion, also an inductively coupled plasma – optical emission spectrometer (ICP-OES) was used.

2.7.1. Q-ICP-MS

The Q-ICP-MS instrument used during this work is the *X-Series 2 (Thermo Scientific* (Bremen, Germany)) in operation at the Analytical Chemistry department of Ghent University. The instrument was equipped with a peristaltic pump for sample introduction, a 1 ml/min concentric nebulizer and an impact bead spray chamber cooled to 1 °C. The mass spectrometer is a quadrupole, used in combination with an electron multiplier detection system. For each measured element, a calibration curve has to be constructed. In addition, an internal standard is necessary. Different parameters are adapted to obtain optimal output signals; the instrument settings are listed in §9.2. Figure 2-1 shows the setup of a Q-ICP-MS instrument.
Before each measurement, a performance test is done to check if background signals, the levels of doubly charged species and of oxides are below a threshold level set by the manufacturer.

2.7.2. SC-ICP-MS

The SC-ICP-MS instrument used during this work is an *Element XR (Thermo Scientific* (Bremen, Germany)) in operation at the Earth Sciences department of the University of Cambridge. The instrument was equipped with a micro-concentric nebulizer and a Scott-type spray chamber. The mass

spectrometer is a sector field analyser of reverse Nier-Johnson geometry in combination with an electron multiplier and an additional Faraday cup.

2.7.3. MC-ICP-MS

The MC-ICP-MS instrument used during this work is a *Neptune (Thermo® scientific, (Bremen, Germany))* in operation at the Analytical Chemistry department of Ghent University. The instrument was equipped with a micro-concentric nebulizer and a high-stability spray chamber, consisting of a cyclonic and a Scott-type sub-unit. The mass spectrometer is a double-focusing sector field analyzer in Nier-Johnson geometry in combination with nine Faraday cups and four ion counters. In this work, a maximum of two Faraday cups were used at the same time. The multi-collector setup is able to compensate for the influence of drift as it measures the signals of the isotopes of interest simultaneously.

Different parameters are adapted to obtain optimal output signals; the settings of the instrument are listed in § 9.2.

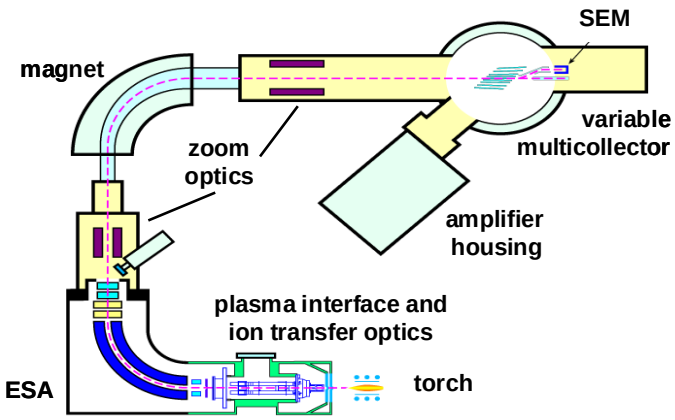

Figure 2-10 from Bouman (2008) [24]: instrumentation of the Neptune, MC-ICP-MS

2.7.4. ICP-OES

In this section, we focus on the characteristics of the *Spectro® Arcos* ICP-OES instrument *(Kleve, Germany)* used during this work.

The sample introduction system and ICP parts of the instrument are similar to those used in ICP-MS. Only, the plasma torch can be placed in axial or radial position [33]. The axial position results in better limits of detection, but has limited robustness against samples with a heavy matrix [33]. The radial position results in higher limits of detection and is mostly used for samples with high salinity and organics content [33]. The ICP source is used to excite the atoms and ions. Analyte atoms and ions emit light of typical wavelengths. The emitted light is guided through a system of lenses and mirrors to a polychromator. The polychromator separates the light beam according to wavelength. A Paschen-Runge mounting of detectors is used in the Arcos instrument, as shown in Figure 2-11 [33]. The emission lines of interest are measured simultaneously using a linear array consisting of 32 CCD

detectors [33]. This detector array is able to measure the whole spectrum between 130 nm and 770 nm [33]. The resolution in the range of 130 to 340 nm is 8.5 pm, whereas in the range of 340 to 770 nm, it is 15 pm [33].

For each measured element, a calibration curve needs to be constructed. In addition, an internal standard is necessary. Different parameters are adapted to obtain optimal output signals.

Before each measurement, a test is done to check if different parameters, are meeting the corresponding threshold values, set by the manufacturer. The different parameters are shown in § 9.2.

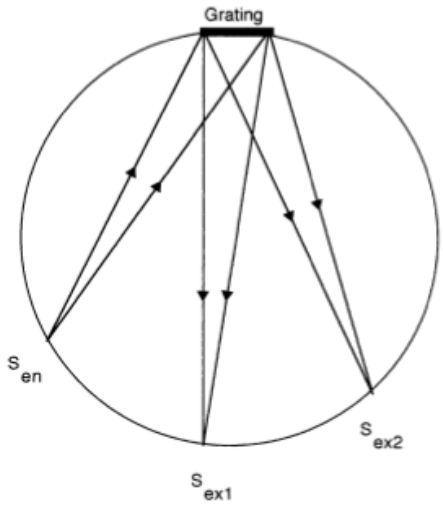

Figure 2-11 from IUPAC [34] : Pasche-Runge mounting in an ICP-OES.

3. Reagents and standards

This Chapter describes both the reagents and instrument parameters used throughout this work. If conditions differ from those described below, it will be explicitly mentioned. During this work, experimental work was carried out at the department of Analytical Chemistry of Ghent University and at the Earth Sciences department of the University of Cambridge. A distinction between these two universities is made.

3.1. Acids

3.1.1. Department of Analytical Chemistry, Ghent University

Single-distilled hydrochloric acid was prepared from pro-analysis grade hydrochloric acid using a quartz sub-boiling distillation setup.
Single-distilled nitric acid was prepared from pro-analysis grade nitric acid using a Teflon® sub-boiling distillation setup (Cupola still, *PicoTrace*®). All dilutions were prepared using 18.2 MΩ.cm Milli-Q water. All sample preparations were performed under class-10 clean lab conditions.

3.1.2. Earth Science department, University of Cambridge:

Double-distilled hydrochloric acid was prepared from reagent grade hydrochloric acid, *Fischer*®, using a Teflon® sub-boiling still.
All sample preparations and column chemistry were performed under class-100 clean lab conditions.

3.2. Isotopic Standards

IRMM-016 Li_2CO_3 (IRMM, Geel, Belgium) isotopic reference material was used as lithium isotopic standard. NIST 951 boric acid was used as boron isotopic standard. The $^{7}Li/^{6}Li$ ratio is 12.177 ± 0,013 and $^{11}B/^{10}B$ ratio is 4.043 ± 0,003 [35,36].
The L-SVEC lithium standard *(NIST, Gaithersburg USA)* is the internationally accepted Li isotopic reference material relative to which the $\delta^{7}Li$ values are calculated. Both L-SVEC and IRMM standards are Li_2CO_3. Both originate from the same geological source material: Spodumenen and petalite from the Foote Mine, Kings Mountain, NC, USA [37]. Grégoire et al. (1996) [37] reported isotopic uniformity between these standards. Thus, $\partial^{7}Li$ values calculated against these respective standards are supposed to be equal.

3.3. Elemental standards

Elemental standard solutions of 1 g/l (Inorganic Ventures (Nieuwegein, The Netherlands)) of Li, Be, Na, Mg, Al, P, K, Ca, Sc, Ti, Cr, Mn, Fe, Co, Ni, Cu, Sr and Y were used. All standards, except for Be, were used for calibration curves relied upon for ICP-OES and Q-ICP-MS analysis. Be was used as an internal standard.

4. Description of K/Pg boundary samples and optimization of the isolation and digestion of the clay fraction

4.1. Geological background of the K/Pg boundary

The K/Pg boundary is linked to the fifth and most recent mass extinction on planet Earth [38]. For a long time, volcanic activity was considered to be the cause of this mass extinction [39,40]. However, Alvarez et al. proposed a hypothesis of an extra-terrestrial event in 1980 [38]. Alvarez et al. (1980) [38] discovered an anomaly of iridium (Ir) and other platinum group elements (PGE) in the K/T clay layer of the Umbrian region (Italy). These elements are classified as siderophile according to their geochemical behaviour and therefore, natural concentrations of these elements are low in the Earth's crust, but enriched in extra-terrestrial objects [41]. In 1991, Hildebrand et al. (1991) [42] linked the 180 km diameter impact crater located on the Yucatán peninsula (Mexico) to the K/T boundary impact event [42,43].Figure 4-1 shows the locality of the Chicxulub impact crater.

Nowadays, the largest part of the scientific community agrees that an impact event took place and that it was the primary cause of the mass extinction [40]. The iridium originating from the Chicxulub projectile has been homogenously spread out across the planet [44].

An iridium anomaly was found across more than 120 different marine and continental sections across the globe [44,45]. Next to the Ir anomaly, also other evidence for a K/T boundary impact at Yucatán peninsula (Mexico) exists: e.g. minerals that acquired shock metamorphic features, impact glass, impact-derived diamonds and Ni-rich spinels [40,43,44,46].

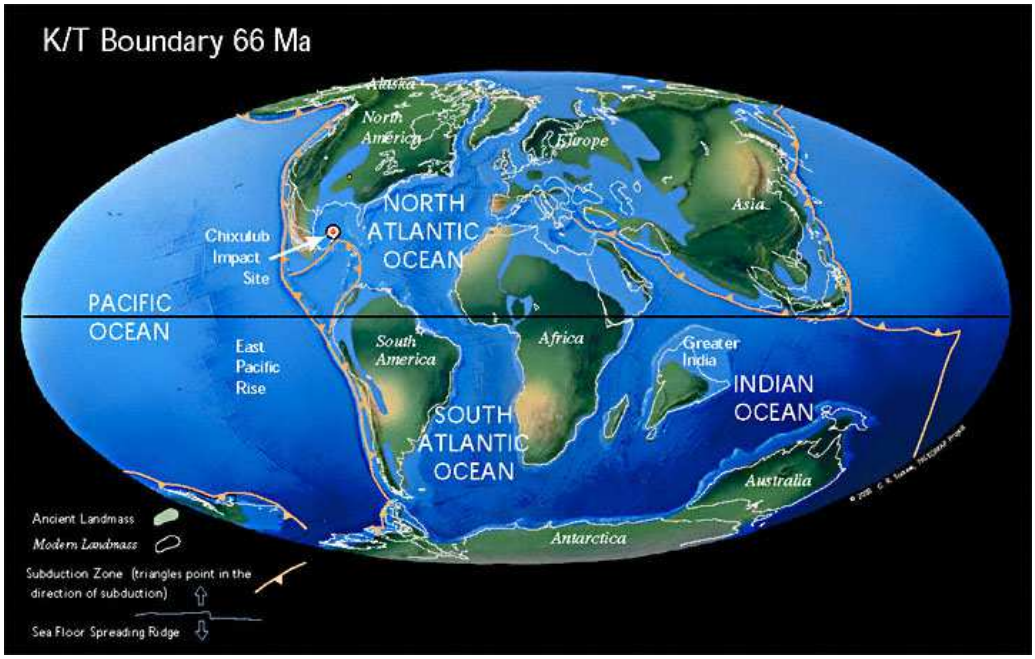

Figure 4-1 from [87]: map of planet Earth showing the situation 66 million years ago.

4.2. Description of the samples

4.2.1. Geological background of the samples

The samples analysed during this Master thesis are geological samples originating from different sites in the Umbria-Marche region (Italy). The Umbria-Marche region consists of marine sedimentary rocks. The region was an epeiric sea from the Late Triassic (~235 million years ago) to the Pleistocene (~2.58 million years ago) [47]. A map showing the palaeography of the world 66 million years ago is shown in Figure 4-1. The samples used in this work are between ~64.7 and ~71 million years of age and originate from the following localities (1) Petriccio (PTC), (2) Furlo Pietralata (FPL), and (3) Fonte d'Olio (FDO), all indicated on Figure 4-2.

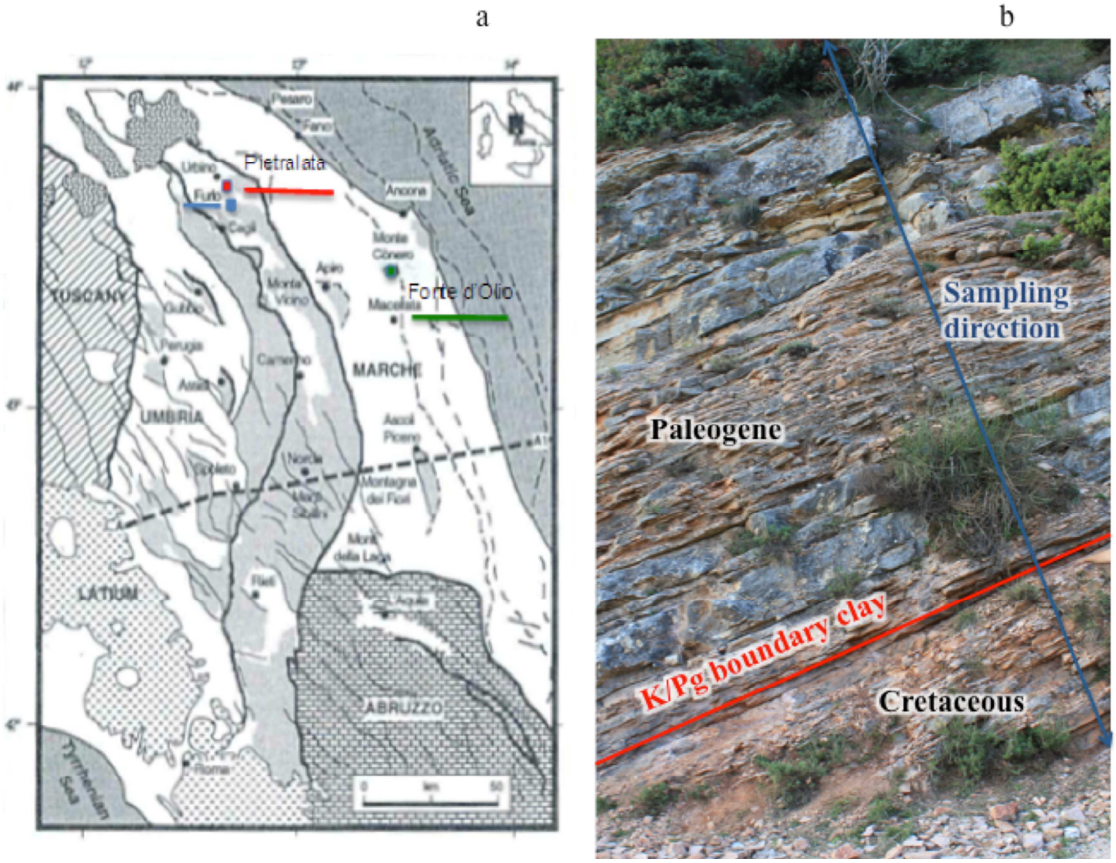

Figure 4-2: (a) from Montanari 2000 [47]: map with indication of the different sampling sites, (b): depth profile of FPL sampling site with indications.

From the sampling localities Petriccio (F1/PTC) and Fonte d'Olio (F3/FDO), only geological samples at the K/Pg boundary were used for analysis. §9.4 shows a detailed picture of the clay layer at FDO.

The sampling site Furlo Pietralata was studied in more detail. The K/Pg boundary (F2/FPL) was set as the chronological reference point and is considered to represent a depth of zero, as shown in Table 4-1. Different depth intervals up to 5 m below and above the K/Pg boundary samples were also studied. Samples below the K/Pg boundary were linked to the Cretaceous (K/FPL), while on the other, samples above the K/Pg boundary were linked to the Paleogene (P/FPL). The sampling depth and estimated age of deposition of each individual sample is shown Table 4-1.

Table 4-1: information on the depth of the samples relatively to F2/FPL (K/Pg boundary) and their ages (estimations based on mean sedimentation rates of few mm/1000 years for carbonates in the Umbria-Marche section).

Sample	Depth (m)	Age (million years)
P1/FPL	5	~64.7
P2/FPL	4	65
P3/FPL	3	~65.3
P4/FPL	2	~65.5
P5/FPL	1	~65.8
P6/FPL	0.1	65.95
F2/FPL	0	66
K7/FPL	-0.1	~66.1
K8/FPL	-1	~67
K9/FPL	-2	~68
K10/FPL	-3	~69
K11/FPL	-4	~70
K12/FPL	-5	~71
F1/PTC	0	66
F3/FDO	0	66

The geological samples are all composed of clay in a limestone matrix. But the ratio of clay/limestone differs for each sampling depth and/or site. The ratio of clay to limestone ranged between < 1 % and 87.6 % taking all samples into account.

The different sampling sites contain clay minerals of the illite, smectite, kaolinite and mixed layered illite-smectite type [48]

4.2.2. Platinum group elements in the clay samples from the Umbria-Marche sequence

The worldwide deposition of clay at the K/Pg boundary is considered to caused by the impact [44]. Samples of the same locality and section as described in Goderis et al. (2013) [44] were used in this work. Goderis et al.(2013) have shown that these samples contain higher amounts of Ir and other PGE, as shown in Figure 4-3. The red hexagons indicate the concentrations of different PGEs in the average continental crust. The blue pentagons indicate the concentrations present in the average continental crust mixed with 5% of a CM-type carbonaceous chondrite meteorite (the meteorite type suggested to have impacted [49,50]). The values for the clay samples originating from different sampling sites are shown in purple. Not only are the PGE concentrations of the clay samples elevated, they also show a flat (*i.e.* chondritic) signature, different from the fractionated pattern typically observed for terrestrial rocks.

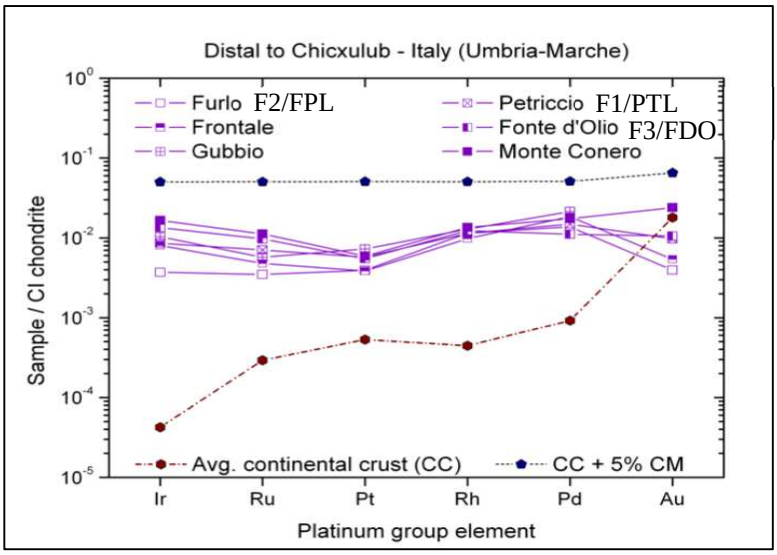

Figure 4-3: from Goderis (2013) [44]: Different platinum group element concentrations on a CI group carbonaceous chondrite-normalized logarithmic scale.

4.2.3. Position of lithium in clays

Two types of lithium exist in minerals: (1) structural lithium and (2) exchangeable lithium, as shown in Figure 4-4 (a). Structural lithium is incorporated in tetrahedrons or octahedrons as the central cation bound to oxygen or hydroxyl, where it replaces a central silicon atom [10].

This is also demonstrated by Vigier et al. (2008) [51]: during smectite formation, lithium is incorporated into the octahedral sites of the clay mineral as shown in Figure 4-4 (a) [51]. It is preferentially the ^{6}Li that acts as the central atom, which leads to isotope fractionation and forms the basis of the lithium isotope proxy [9,10,51]. In contrast with structural lithium, the exchangeable lithium in clays is easily replaced with other cations in solution [51]. There, it is part of the interlayer between two tetrahedron/octahedron sheets.

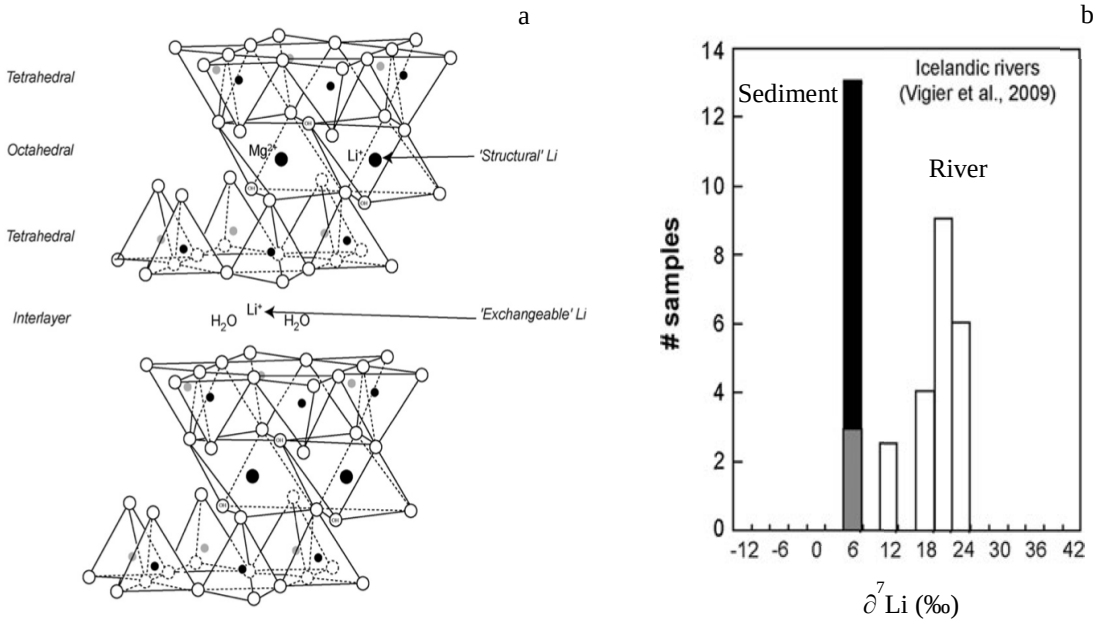

Figure 4-4 : (a) from Vigier (2008) [51]: black and gray circles are Si^{4+} cations, white circles are oxygen. (b) from Burton (2011) [10]: white = river water, grey = suspend sediment and black = bedload sand.

4.2.4. Lithium as an indicator for weathering

The occurrence of lithium fractionation during weathering has been proven by (1) comparing the ∂^7Li values in waters with ∂^7Li values in the neighbouring bedrocks and (2) looking at seawater ∂^7Li values. A general trend of higher ∂^7Li values for waters, compared to their parent carbonate or silicate rock, was observed [10,13,52]. This trend is illustrated in Figure 4-4 (b), where a difference can be seen between, on one side, the parent rock, *i.e.* the suspended sediment and bedload sand, and, on the other side, the water phase. In addition, by looking at planktonic foraminifera, Misra and Froelich (2012) [12] found increasing ∂^7Li values of seawater from the Paleogene (~22 ‰) until present (~31 ‰). This increase in ∂^7Li values of seawater also supports the influence of silicate weathering and the fractionation process occurring during the weathering.

4.3 Experimental

4.3.1. Sample preparation

The sample preparation consists of four major parts: (1) sampling, (2) homogenization of the geological samples, (3) separation of the clay out of the limestone matrix and (4) destruction of the clay structure.

4.3.1.1. Sampling

Samples were taken from different K/Pg sections in the Umbria-Marche region (Italy). Sampling was done every 1 m in a 10 m interval across the boundary, resulting in a set of 10 samples. In addition, at 0.1 m above and below the K/Pg clay boundary, samples were taken. The depth profile was perpendicular to the bedding, shown in Figure 4-2 (b). Large chunks of carbonate rocks were removed from the bedding using a hammer and crowbar; the boundary clay was removed using a small spatula.

4.3.1.2. Homogenization of the geological samples

Samples from different depth intervals were sawn into smaller pieces of approximately 5 g by a diamond saw. These parts were homogenized with an agate pestle in an agate mortar. Between every homogenization step, both mortar and pestle were rinsed with Milli-Q water, scrubbed with pro analysis quartz, *Merck* (Darmstadt, Germany) and rinsed again with Milli-Q water.

4.3.1.3. Isolation of the clay

Limestone mainly consists of calciumcarbonate ($CaCO_3$). The $CaCO_3$ readily reacts with diluted acid to CO_2, H_2O and free cations.

Dissolution of the limestone matrix was performed using different batches of 0.14 M HNO_3. At least ten additions of 2 ml 0.14 M HNO_3 were required for complete removal of the limestone for the

Cretaceous and Paleogene samples. The K/Pg boundary samples contained less limestone, 5 batches of 2 ml 0.14 M HNO_3 were added in these cases.

After each acid addition, the samples were vortexed and placed in a sonication bath for approximately 15 to 20 min. The sonicated samples were centrifuged by a fixed angle centrifuge, *(Heraeus Sepatech®, Labofuge 200)* for 10 min at 5300 rpm. The supernatant was removed with a Pasteur pipet and the procedure was repeated.

Dissolution profiles of Ca, Na, Mg, Mn, P, Sr and K were constructed for samples P5/FPL and K8/FPL via 10 collected batches of acid fractions. These batches were diluted 5 times prior to analysis. All steps were performed in centrifugation tubes *(VWR International®, 15 ml metal free centrifuge tubes).* Measurements were performed with ICP-OES. The isolated clay fractions were dried in a stove for 24 h at 105 °C, weighed and transferred to 15 ml Savillex® Teflon® beakers.

4.3.1.4. Destruction of the clay structure

4.3.1.4.1. Clay digestion procedure

Clay fractions were destructed via two closed vessel digestion steps using concentrated strong acids.

In the first step, 3 ml of a 2:1 HF:HNO_3 mixture was added to the samples. This solution was first kept on a hot plate at 110 °C during 24 h, then allowed to cool to room temperature and subsequently evaporated to dryness at 80 °C. In the second step, the residue was re-digested using 3 ml of aqua regia at 95 °C for 24 h, allowed to cool to room temperature and evaporated to dryness at 80 °C. Finally, the digested clay sample was re-dissolved in 0.28 M HCl to a final volume of 750 µl. All steps were performed under class-10 clean lab conditions in 15 ml Savillex® Teflon® beakers. The final samples were transferred to acid-cleaned Eppendorf tubes before transport to the University of Cambridge (UK), where they underwent a cation exchange chromatography procedure.

4.3.1.4.2. Li spike recovery experiments

The digestion procedure described above might induce fractionation [37]. Therefore, full recovery of lithium during the whole digestion procedure was aimed at.

Six digestions of ± 40 mg of NIST® 679 Brick Clay were performed in parallel in a lithium recovery experiment. Three of these samples were spiked with 2 µg of lithium IRMM-016 standard, whereas no lithium was spiked to the three other samples. In addition, a blank and two lithium-spiked blanks, containing 50 ng of lithium each, were treated using the same digestion procedure.

Final samples were diluted 50-fold prior to lithium concentration determination with the *X-Series 2* Q-ICP-MS.

4.4. Results and discussion

4.4.1. Isolation of clay fraction

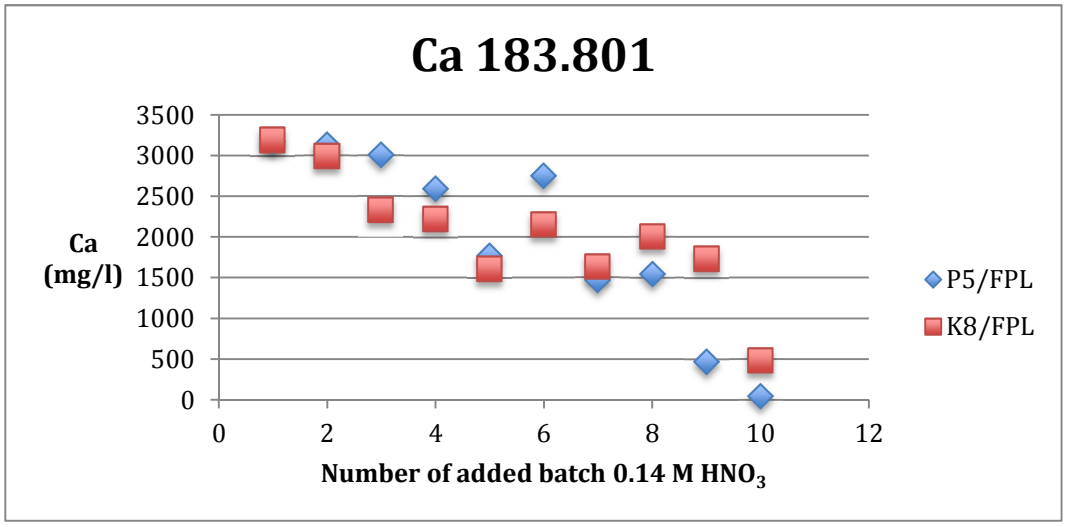

Figure 4-5 : calcium concentration as a function of the added batch of acid.

A leaching profile of ten additions of 0.14 M HNO_3 for calcium is shown in Figure 4-5. For each samples the dissolvation of the limestone was visually determinated, as no more CO_2 gas bubbles were observed during the treatment with the last fraction. This was confirmed by the concentration profile of Ca in the acid fractions for P5/FPL, shown in Figure 4-5, and the low calcium concentrations in the digested clay fractions in table 4.3., (except for K11/FPL and K12/FPL). K8/FPL required additional acid fractions to eliminate the limestone matrix. Higher sonication times during batch six can explain an increase in the dissolved calcium concentration at that stage. Leaching profiles of Na, Mg, Mn, P, Sr and K are shown in §9.4.

4.4.2. Exchangeable Lithium

From §4.2.3, it is clear that two types of lithium exist in clay minerals. However, the lithium proxy is applicable to the structural lithium only. It was reported by Vigier et al.(2008) [51] that structural and exchangeable lithium in clays have a different isotopic composition. The authors synthesized smectite clay structures and incorporated lithium into the octahedral sites, using a 3 M LiCl solution.

After synthesis, exchangeable lithium concentrations varied between 120 ppm and 3400 ppm and were completely removed by three treatment steps with saturated 1 M NH_4Cl solution. The ∂^7Li difference between the structural lithium and the lithium of the LiCl solution was -10.1 ‰ at a synthesis temperature of 25°C.

During this work, between 5 and 10 batches of 0.14 M HNO_3 were used to dissolve the limestone and to remove interstitial Li. However, no specific experiments have been performed yet in order to determine whether all interstitial Li was removed, without loss of structural lithium.

Nevertheless, an indication that the free cations, originating from the acid and limestone dissolution, were sufficient to remove the exchangeable lithium is supported by the following reasoning. The exchangeable lithium in the clay samples is expected to have ∂^7Li values close to those of seawater, *i.e.* 31.0 ± 0.5 ‰. On the other hand, the ∂^7Li values obtained for the clays were all slightly negative, while the ∂^7Li values of the upper continental crust are 0 ± 2 ‰ [15,53]. Hence, the lower ∂^7Li values obtained for the clays are perfectly in line with values that might be expected from continental crust subjected to weathering processes. Substantial contamination of the samples with interstitial lithium would inevitably have resulted in positive ∂^7Li values. This suggests that no or negligible exchangeable lithium was present after limestone dissolution.

4.3.3. Chemical Composition of the clays

The composition of the clay was determined with Q-ICP-MS and ICP-OES. Q-ICP-MS was used for determination of the Li, P, Sc, Ti, Cr, Mn, Co, Ni, Cu and Y concentrations. ICP-OES was used for measuring the Ca, Na, Mg, Fe, Sr, K and Al concentrations. Instrumental settings are mentioned in § 9.4. The clay fraction digests of the Cretaceous and Paleogene were diluted 100-fold, those of the K/Pg boundary 200-fold.

The chemical composition of the different clay samples differed very much, as shown in Table 4-2 and Table 4-3. Lithium concentrations ranged between 84 µg/l and 2440 µg/l.
The lithium concentrations in the digested clays were used as a reference for the load volume during column chemistry, this is further explained in chapter 7.

Table 4-2: Chemical composition of the clays into solution. All shown concentrations are undiluted and expressed in µg/l. Also the corresponding LODs and LOQs have been added. Samples of the Paleogene and Cretaceous were diluted 100 times. K/Pg boundary samples were diluted 200 times.

Concentration µg/l in clay digests measured via Q-ICP-MS

Sample	Li	P	Sc	Ti	Cr	Mn	Co	Ni	Cu	Y
P1/FPL	84	465	140	12800	450	700	205	720	720	720
P2/FPL	22	415	125	9690	305	550	59	655	655	655
P3/FPL	745	1600	240	58600	1960	3440	480	2530	2530	2530
P4/FPL	590	1660	220	51300	1980	3520	440	2740	2740	2740
P5/FPL	405	950	180	38800	1330	2140	510	2100	2100	2100
P6/FPL	495	2370	190	43900	3180	5900	470	1970	1970	1970
F2/FPL	1250	3710	300	104000	6540	12100	955	4620	4620	4620
K7/FPL	465	1700	180	34500	2220	4130	315	1870	1870	1870
K8/FPL	540	1990	210	42100	3650	6870	420	2380	2380	2380
K10/FPL	530	1650	210	38100	2200	4030	370	2080	2080	2080
K11/FPL	545	2200	200	41100	3670	6920	420	2530	2530	2530
K12/FPL	860	4700	260	54200	5740	11000	505	4320	4320	4320
F1/PTC	1150	2600	255	72100	4410	7950	875	3520	3520	3520
F3/FDO	2440	4960	420	133000	2430	3810	1050	6460	6460	6460
LOD	0.001	0.02	0.008	0.004	0.020	0.02	0.001	0.006	0.01	0.0005
LOQ	0.004	0.06	0.03	0.01	0.07	0.06	0.005	0.019	0.04	0.002
Nuclides monitored	7	31	45	47	52, 53	55	59	60, 62	63, 65	89

The results show a typically relative uncertainty of a couple of %.

Table 4-3: Chemical composition of the clays into solution. All shown concentrations are undiluted and expressed in mg/l. Also the corresponding LODs and LOQs have been added. Samples of the Paleogene and Cretaceous were diluted 100 times. K/Pg boundary samples were diluted 200 times.

Concentration mg/l in clay digests measured via ICP-OES

Sample	Ca	Na	Mg	Fe	Sr	K	Al
P1/FPL	44	3	31	97	<LOQ	81	295
P2/FPL	120	4	16	51	0.05	59	200
P3/FPL	<LOQ	20	165	675	0.37	315	1210
P4/FPL	84	20	160	610	0.47	300	1040
P5/FPL	<LOQ	19	110	360	0.29	300	825
P6/FPL	87	23	120	595	0.38	280	800
F2/FPL	<LOQ	71	495	2840	1.72	1270	3290
K7/FPL	93	23	120	485	0.54	310	850
K8/FPL	180	24	145	550	0.67	350	915
K10/FPL	5	27	130	435	0.40	330	870
K11/FPL	420	24	125	505	0.99	310	900
K12/FPL	3530	30	175	725	5.54	410	1230
F1/PTC	<LOQ	44	360	1850	1.31	755	2600
F3/FDO	<LOQ	19	920	3010	1.03	1330	4140
LOD	0.005	0.03	0.00009	0.005	0.0001	0.05	0.01
LOQ	0.02	0.08	0.0003	0.02	0.0004	0.2	0.04
Emmision line (nm)	183.801	589.592	279.553 280.270	238.204 239.562	407.771 421.552	766.491	176.641 308.215

The results show a typically relative uncertainty of a couple of %.

4.3.4. Recovery after clay destruction.

In the NIST brick clay, an average lithium concentration of 64.6 ± 0.9 µg/g (n=3) was found. The certified value (for a minimum sample amount of 250 mg) is 71.7 ± 6.2 µg/g.

The 95 % confidence intervals of both results do not overlap, but do touch each other.

The recovery of 2 µg lithium spiked to the three NIST brick clay samples was 98.0 ± 3.0 %. The recovery of 50 ng of lithium in the spiked blank was 103.9 ± 1.4 %.

These results show that lithium is not lost during the digestion process. As far as the NIST 679 brick clay material is concerned, more experimental work on larger masses have to be performed to determine whether lithium can be fully recovered from the clay matrix. No recovery test with spikes was performed for the clay samples. A recovery of 100 % was assumed.

4.4. Summary of Chapter 4

This chapter described the origin of the samples. Their relation with the extra-terrestrial impact was proven by elevated concentrations of Ir and other PGE in earlier work.

Sample preparation consisted of four steps: (1) sampling, (2) homogenization, (3) isolation of clay from limestone matrix, (4) digestion of clay samples.

Two types of lithium in clays occur: structural lithium, *i.e.* Li^+ is incorporated in tetrahedrons or octahedrons and exchangeable lithium, *i.e*. as free cation in the interlayer between two tetrahedron/octahedron layers.

The clay fractions were successfully separated from their limestone matrix and acid-digested. Exchangeable lithium was assumed to have been washed out of the clay matrix, although this must be confirmed experimentally in the near future. In lithium spike recovery experiments, full lithium recovery was obtained during the digestion process.

The composition of the clay digest was determined. Lithium concentrations ranged between 84 µg/l and 2440µg/l. These concentrations were of importance when performing the column chromatography, as described in chapters 5 and 7.

5. Optimization of lithium isotopic analysis by MC-ICP-MS

MC-ICP-MS analysis suffers from several sources of bias that influence the isotope ratio results obtained. This chapter will focus on the different sources of bias and the various methods to overcome them, both from a theoretical and an experimental point of view. In addition, the influence of the amplifier resistance and sodium concentrations on lithium isotope ratio measurements were studied.

5.1. Spectral interferences and mass discrimination

5.1.1. Spectral interferences

In mass spectrometry, analyte ions are separated according to their mass-to-charge ratios. As a result, any positively charged species with the same mass-to-charge ratio as the analyte nuclide can give rise to spectral interference, sometimes also called isobaric or spectroscopic interference, thus affecting the isotope ratio measurement result. Since in MC-ICP-MS, the analyte is isolated from the matrix compounds, the remaining interfering species mostly originate from Ar, the acid, the solvent and/or entrained air [54]. Specifically for Li isotopes, $^{12}C^{2+}$ and $^{14}N^{2+}$ ions can cause spectral overlap with $^{6}Li^{+}$ and $^{7}Li^{+}$, respectively.

5.1.2. Mass discrimination

When determining isotope ratios with ICP-MS, mass discrimination causes the measurement result to show a bias with respect to the corresponding true isotope ratio. This effect on in isotope ratios originates from differences in the efficiency of ion extraction, transmission and detection as a function of the analyte mass [18,55]. Moreover, also (1) the matrix and (2) the analyte concentration have been shown to affect the extent of mass discrimination. Different mathematical correction methods have been developed to correct for instrumental mass discrimination [18]. In addition, various rules for good practice regarding sample preparation and measurement sequence have to be taken into account.

5.1.2.1. Instrumental mass discrimination

Instrumental mass discrimination is often called mass bias. Mass bias is thought to be a result from (1) the supersonic expansion occurring in the interface, described in §2.3. and (2) the space-charge effects in the positive ion beam, described in §2.4. [54–56]. Both effects result in higher losses of lighter elements, so mass bias is more pronounced for lighter elements, as shown in Figure 5-1 (b) [54,56].

The magnitude of this type of mass discrimination is influenced by the configuration of the instrument and the instrument settings, e.g., ion-lens voltages, aerosol carrier gas flow rate, position of the torch, type of nebulizer & spray chamber, type & conditions of the cones, *etc.* [37,55]. Optimizing the instrument before use is necessary, but completely eliminating these effects is impossible [37]. Nevertheless, various mathematical procedures to correct isotope ratios obtained with MC-ICP-MS

for mass discrimination have been described in the literature [56–58]. Some of these approaches were evaluated in this work. Theory and practice are described further in this chapter.

5.1.2.2. Matrix-induced mass discrimination

The matrix accompanying the analyte and the solvent in which it is dissolved can influence the isotope ratio result. For example, space-charge effects, described in §2.4., are more pronounced when a high concentration of a heavy matrix element is present [55,56,59]. Also other types of matrix effects, e.g., caused by the presence of easily ionisable elements (EIEs) have an, affect isotope ratio results. High concentrations of Na^+ and/or K^+, e.g., decrease the $^7Li/^6Li$ ratio, while high concentrations of Sr increase the $^7Li/^6Li$ ratio [37], until present no explanation for these opposite effects is described. Both matrix-matching of standards and working with ultra-clean matrices after analyte isolation offer a solution to deal with these effects [37]. However, as the chemical composition of clays originating from the Umbria-Marche sequence is very variable, matrix-matching would be a very inefficient approach. Therefore, in this work, a single-step cation exchange chromatography isolation procedure was applied to all clay samples in order to achieve a purified lithium fraction. Although lithium is isolated, certain ions will always be present in the ion beam*: i.e.* $^{40}Ar^+$, $^{12}C^+$, $^{14}N^+$, $^{16}O^+$, H^+ and polyatomic ions that consists of combinations of these elements [53].

5.1.2.3. Concentration-dependent mass discrimination

Next to matrix elements, also the concentration of the pure analyte itself can affect the extent of mass discrimination. For lithium, two studies, one by Grégoire et al. (1996) [37] and another by Sun et al. (1987) [60], reported anomalies in the $^7Li/^6Li$ ratio with varying Li concentrations. While the study of Grégoire et al. (1996) [37] indicated a decrease of the ratio with increasing concentration of lithium, as shown in Figure 5-1 (a), Sun et al. (1987) [60] drew the opposite conclusion.

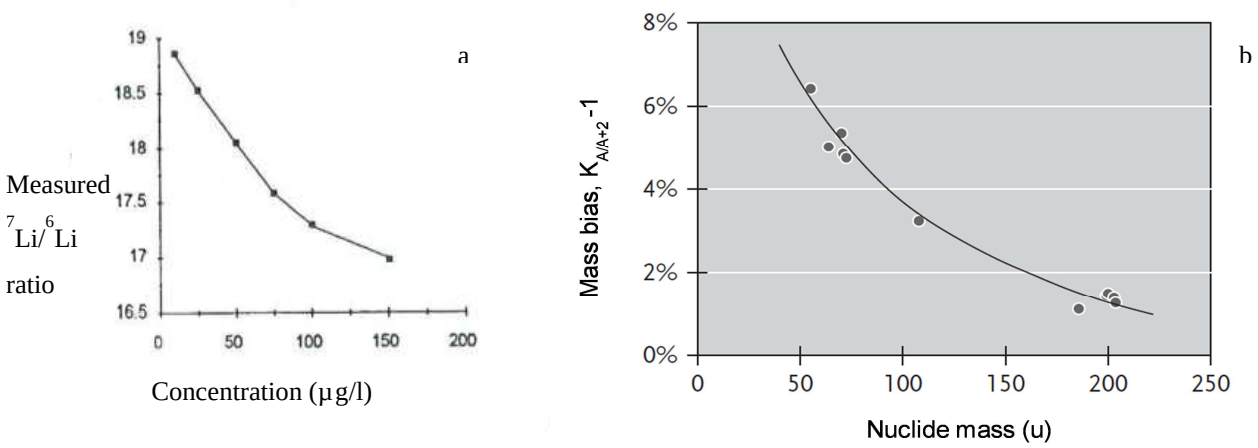

Figure 5-1 (a) from Grégorie (1996) [37]: a decrease in the $^7Li/^6Li$ is measured with increasing concentration. (b) From Vanhaecke (2012) [61]:typical bias in isotope amount ratio measurement results using a Neptune MC-ICP-MS instrument. Isotope ratios $N(^AE)/N(^{A+2}E)$ are considered here.

5.2. Testing of different correction models

5.2.1. Theoretical background

Two main types of correction models were used in this Master thesis to correct for mass bias, *i.e.* (1) external correction and (2) internal correction type II.

External correction uses the data obtained for an isotopic standard of the same element to correct for mass discrimination in the sample. 'External' refers to the fact that standard and sample solutions are different.

In the standard-sample bracketing technique, the most widely used external correction method, the sample is preceded and followed by a standard solution of known isotopic composition. The principle of interpolation is then used to obtain the correction factor for the sample. Mathematical equation of the bracketing model:

$$\text{Bracketing: } R_{true,s} = \frac{R_{true,std}}{\frac{R_{obs,std\,1}+R_{obs,std2}}{2}} * R_{obs,s} \qquad \text{Eq. 5.1.}$$

$R_{true,s}$ = true isotope ratio of the sample, $R_{true,std}$ = isotope ratio of certified reference material, $R_{obs,std\,1}$ = observed isotope ratio for the standard measured before actual sample, $R_{obs,std}$ = observed isotope ratio for the standard measured after actual sample, $R_{obs,s}$ = observed isotope ratio for the sample.

It is important that the concentration of the standard and sample match within a range of ± 30 % to avoid an effect of the analyte concentration on the extent of mass discrimination [18,37]. In addition, the type and concentration of the acid matrix can also affect the extent of mass bias [37]. Therefore, standard and sample solutions should be prepared with the same acid type and concentration. This correction type hence requires matrix matching of samples and standards [54].

Internal correction type II uses the mass bias of an isotope pair of another element (the internal standard) to correct for the mass bias affecting the analyte [62]. 'Internal' refers to the fact that the internal standard is present in the sample solutions.

The internal standard, added to the solution, has to be close in mass to the analyte, as correction models assume that relative instrumental mass discrimination for both the internal standard and analyte isotopes are similar, as was shown in Figure 5-1(b) [18,54]. Of course, the isotope ratio of the internal standard isotope pair has to be well known.

Four internal correction models were used in this work *i.e.* the (1) the exponential law, (2) Russell's law, (3) the Baxter-Woodhead approach and (4) CAIS (common analyte internal standardization) [18,57,58].

The exponential law is described by the following equation:

$$\text{Exponential: } R_{true} = e^{\varepsilon_{expon} * \Delta m} * R_{obs} \qquad \text{Eq. 5.2.}$$

R_{true} = true isotope ratio for the sample, R_{obs}= observed isotope ratio for the sample, Δm = difference in mass between heavy and light isotope, ε_{expon} = exponential mass discrimination factor.

The exponential model (Eq. 5.2.) takes into account the mass difference between the heavy and the light isotope, whereas Russell's law (Eq. 5.3.) takes into account the mass ratio of the two isotopes.

$$\text{Russell: } R_{true} = \left(\frac{m2}{m1}\right)^{\beta} * R_{obs} \qquad \text{Eq. 5.3.}$$

R_{true} = true isotope ratio for the sample, R_{obs}= observed isotope ratio for the sample, m1 = mass of the lighter isotope, m2 = mass of the heavier isotope, ß = Russell mass discrimination factor

Both the exponential law (ε_{expon}) & Russell's law (ß) define a mass discrimination factor, however, two approaches can be distinguished: (1) the original approach(=), whereby the mass discrimination factor of the analyte is assumed to be the same as the one of the internal standard and (2) the empirical approach(≠), where both mass discrimination factors are assumed to be different. Herein, the slope and intersect of a linear relationship between the mass discrimination factors of the analyte and internal standard are established based on the measurement of standard solutions and are subsequently used to calculate a new mass discrimination factor for the analyte in the sample based on the experimentally determined mass discrimination factor for the internal standard.

The next model applied in this work, is the Baxter-Woodhead approach:

$$\text{Baxter-Woodhead: } R_{true,s} = \frac{R_{obs,s} * R_{true,std}}{e^{b0} * R_{obs,IS}{}^{b1}} \qquad \text{Eq. 5.4.}$$

$R_{true,s}$ = true isotope ratio for the sample, $R_{obs,s}$ = observed isotope ratio for the sample, $R_{true,std}$ = isotope ratio for the certified reference material, $R_{obs,IS}$ = observed isotope ratio for the internal standard, b_0 and b_1 represent the intersect and slope, respectively, of a linear calibration line between $\ln(R_{obs,s})$ and $\ln(R_{obs,IS})$.

The final correction method used here is the CAIS model [58]. A series of standard solutions, of which some were spiked with various concentrations of HCl, with known isotopic composition of lithium and boron was measured, wherein lithium was the analyte and boron was the internal standard. The observed lithium ratios ($^7Li/^6Li_{std,obs}$) and the observed internal standard ratios ($^{11}B/^{10}B_{std,obs}$) were plotted against each other to construct a linear relationship. For each sample, the intersect and the slope of this linear relationship together with the observed internal standard ratio ($^{11}B/^{10}B_{std,obs}$) was used to calculate the expected lithium isotope ratio of the standard as if it would be present in that sample ($^7Li/^6Li_{std,calc}$). The ratio of the true lithium ratio of the standard ($^7Li/^6Li_{std}$) to the calculated expected lithium ratio ($^7Li/^6Li_{std,calc}$) was set as a correction factor for that particular sample. Finally, the multiplication of this correction factor with the observed lithium ratio in the sample ($^7Li/^6Li_{sample,obs}$) resulted in the corrected lithium ratio ($^7Li/^6Li_{sample,corr}$) of the sample.

Additionally, both external and internal correction methods can be used in combination, e.g., through application of standard bracketing after the results have been treated according to any of the internal correction type II methods. In this work, both the result obtained without and with additional external calibration after application of an internal correction model are reported.

5.2.2. Experimental

5.2.2.1. Reagents

Hydrofluoric acid, *Fischer*®, of ultrapure grade was used.

5.2.2.2. Sample preparation

Six solutions (15 ml) with different concentration Li:B ratios ranging from 1:5 (50 µg/l : 250 µg/l) to 5:1 (250 µg/l : 50 µg/l) were prepared. Another two sets of six solutions (5 ml) with the same Li:B ratios and concentrations were prepared, one set of which was spiked with 0.5 M HCl and the other spiked with 2 M HCl. The latter solutions were prepared to deliberately induce different extents of mass discrimination compared to the non-spiked solutions, for application of empirical models. All solutions were prepared in 1 % (v/v) HF.

Table 5-1: Li:B ratio in solutions and corresponding concentrations of Li and B.

Solutions for correction model testing						
Li:B	**1:5**	**1:2**	**1:1**	**2:2**	**2:1**	**5:1**
Li (µg/l)	50	50	50	100	100	250
B (µg/l)	250	100	50	100	50	50

5.2.2.3. MC-ICP-MS measurements

The prepared solutions were measured using the Neptune MC-ICP-MS instrument. The introduction system consisted of a Teflon® micro-concentric nebulizer in combination with a Scott Teflon® spray chamber. The sample introduction rate was 100 µl/min. A plasma torch with a sapphire injector tube was used.

Eleven replicate measurements were performed for each non-spiked solution. The mean ∂^7Li and the standard deviation (s) were calculated from 11 ∂^7Li results in case no bracketing was applied after internal correction and from 9 measurements in case bracketing was applied, with or without internal correction. HCl-spiked solutions were randomly measured three times in-between every set of 11 duplicate measurements of non-spiked solutions. The instrumental settings used are shown in §9.5.

5.2.3. Results & discussion

The results obtained via different correction models are shown in Table 5-1. The theoretical ∂^7Li value of the IRMM-016 isotopic reference material is zero. The mean ∂^7Li values and uncertainties,

calculated as two times the standard deviation, are shown per correction model for the various Li:B concentration ratios.

Table 5-2: results for each different correction model.

Overview of results via various correction models

			Li: B					
			1:5	**1:2**	**1:1**	**2:2**	**2:1**	**5:1**
Bracketing	Bracketing	Mean δ^7Li (‰)	0.0	0.0	0.0	0.0	0.0	0.0
		Uncertainty	0.3	0.4	0.3	0.3	0.3	0.3
Original exponential law (ƐLi = ƐB)	Without bracketing	Mean δ^7Li (‰)	72.2	72.1	72.8	74.2	74.3	75.0
		Uncertainty	0.2	0.4	0.6	0.5	0.5	0.7
	With additional bracketing	Mean δ^7Li (‰)	0.0	0.0	0.0	0.0	0.0	0.0
		Uncertainty	0.2	0.4	0.4	0.2	0.3	0.4
Empirical exponential (ƐLi≠ƐB) law, empirical Russell law (ßLi≠ßB□ and Baxter-Woodhead	Without bracketing	Mean δ^7Li (‰)	0.0	-0.1	-0.2	0.0	-0.1	-0.1
		Uncertainty	0.3	0.3	0.6	0.4	0.5	0.6
	With additional bracketing	Mean δ^7Li (‰)	0.0	0.0	0.0	0.0	0.0	0.0
		Uncertainty	0.2	0.5	0.5	0.2	0.4	0.4
Original Russell Law (ƐLi = ƐB)	Without bracketing	Mean δ^7Li (‰)	-13.5	-13.5	-12.6	-11.5	-11.1	-10.4
		Uncertainty	0.3	0.3	0.5	0.3	0.5	0.6
	With additional bracketing	Mean δ^7Li (‰)	0.0	0.0	0.0	0.0	0.0	0.0
		Uncertainty	0.2	0.5	0.5	0.2	0.5	0.5
CAIS	Without bracketing	Mean δ^7Li (‰)	0.0	-0.1	-0.2	0.0	-0.1	-0.1
		Uncertainty	0.3	0.3	0.6	0.4	0.5	0.6
	With additional bracketing	Mean δ^7Li (‰)	0.0	0.0	0.0	0.0	0.0	0.0
		Uncertainty	0.2	0.5	0.5	0.2	0.4	0.4

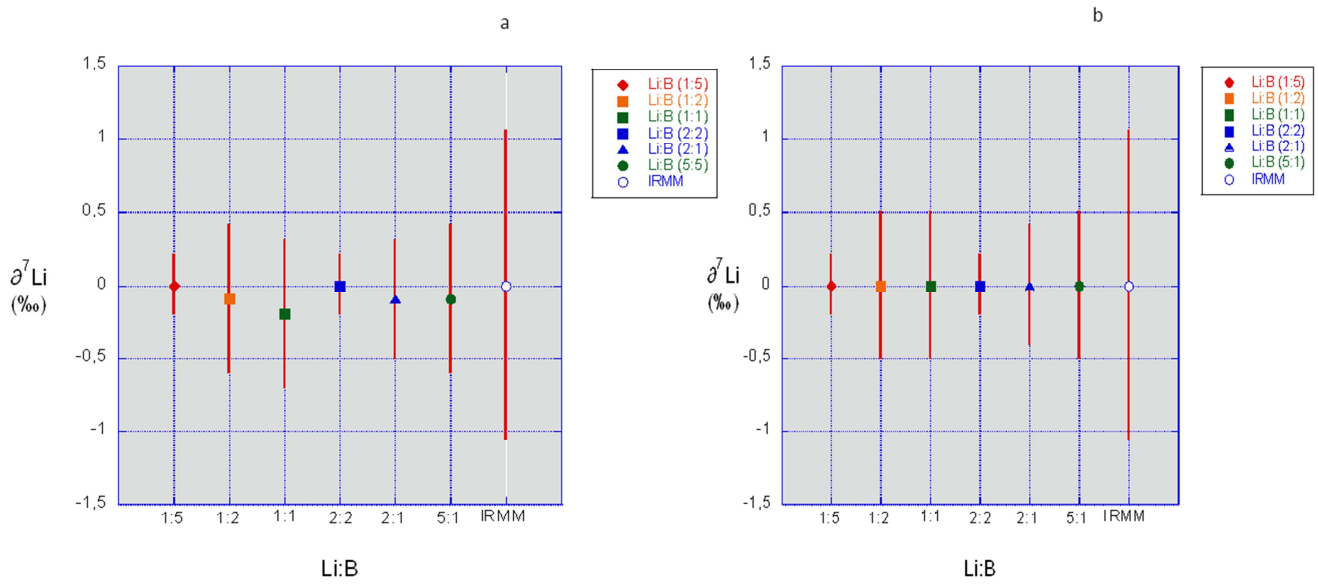

Figure 5-2 (a): ∂^7Li values obtained according to the empirical exponential law (ƐLi ≠ ƐB) as a function of the Li concentrations(b): ∂^7Li values obtained according to the empirical exponential law (ƐLi ≠ ƐB) model in combination with standard bracketing as a function of the Li concentration. Uncertainty is two times the standard deviation (s)

Results comparable to published values, both in terms of accuracy and precision, were obtained for all the models tested, except for the original Russell's law (ßLi = ßB) and the exponential law (ƐLi = ƐB) without additional bracketing. This indicates that the original exponential law and Russell's law are essentially inappropriate for mass discrimination correction of lithium isotope ratios in MC-ICP-MS. When bracketing was applied in addition to the original exponential law and Russell's law, better results were obtained in terms of both accuracy and precision that are similar to those obtained via the other correction models.

The empirical exponential law (ƐLi ≠ ƐB), empirical Russell's law (ßLi ≠ ßB) and Baxter-Woodhead approach, both with and without additional bracketing gave the same results This shows that the assumption of equal mass discrimination factors for boron and lithium, as made in the original exponential law and Russell's law, is not valid. For both the exponential law and Russell's law, documenting and exploiting the linear relationship between the mass discrimination factors of boron and lithium leads to better results. An example of such a linear relationship is shown in §9.5

It is clear that additional external correction improves the results obtained after internal correction. This is also illustrated in Figure 5-2. More graphical overviews can be consulted in §9.5.

Because simple external correction in a sample-standard bracketing approach, gave accurate results and provide the best precision, including constant values despite various Li:B concentrations ratios, this correction method was selected for further experiments.

5.3. Selection of amplifier resistance

The MC-ICP-MS Neptune instrument is equipped with nine Faraday cups, which can be placed in different positions relative to each other. Because the signal in this multiple collectors is a very low current, an amplifier system is used. From Ohm's law (V = IR) can be derived that the magnitude of the resistor governs the amplification [63]. Therefore, the measured voltage is proportional to both the intensity of the ion beam striking the Faraday cup and the applied resistance [64].
Different amplifiers, each with a different resistance (10^{10} – 10^{12} Ω), can be connected to the faraday cups. Switching from a 10^{11} to a 10^{12} Ω amplifier increases the signal ten-fold, whereas the noise is increased with a factor of √10 [24,64]. In practice, the signal-to-noise ratio is improved by a factor of two [64].

In a series of experiments performed at the same day, different amplifiers were linked to the Faraday cups. Lithium solutions of various concentrations, with known isotopic composition, were analyzed. The purpose was to check which combination of amplifier and Li concentration in solution gave acceptable precision and accuracy.

5.3.1. Experimental

5.3.1.1. Reagents and sample preparation

IRMM-016 Li isotopic reference material was used for the preparation of 0.5; 5; 50; 200 µg/l lithium solution in 0.28 M HNO_3.

5.3.1.2. MC-ICP-MS measurements

Measurements were performed with a Neptune MC-ICP-MS. Measurements of different lithium concentrations were performed in combination with different sets of amplifiers. These combinations (together with the results) are shown in Table 5-3.
Blank solutions were analyzed in-between standard solutions. Eleven replicate measurements were performed for each combination of concentration and amplifiers. External correction in a sample-standard bracketing approach was used for calculating the corrected ∂^7Li values. The mean ∂^7Li and standard deviation (s) were calculated from the 9 bracketed ∂^7Li results. Instrumental parameters are shown in § 9.5.

5.3.2. Results & discussion

Table 5-3: results of the MC-ICP-MS amplifier test. Uncertainty was calculated as two times the standard deviation (s).

MC-ICP-MS amplifier test				
Concentration	^{7}Li amplifier	^{6}Li amplifier	∂7Li	Uncertainty
IRMM-016			0.0	1.1
0.5 µg/l	10^{12} Ω amplifier	10^{12} Ω amplifier	-7.5	15.8
5 µg/l	10^{11} Ω amplifier	10^{11} Ω amplifier	0.2	3.9
5 µg/l	10^{12} Ω amplifier	10^{12} Ω amplifier	-0.1	1.7
50 µg/l	10^{11} Ω amplifier	10^{11} Ω amplifier	-0.2	0.3
50 µg/l	10^{12} Ω amplifier	10^{11} Ω amplifier	0.1	0.2
50 µg/l	10^{12} Ω amplifier	10^{12} Ω amplifier	-0.1	0.1
200 µg/l	10^{11} Ω amplifier	10^{11} Ω amplifier	0.0	0.2

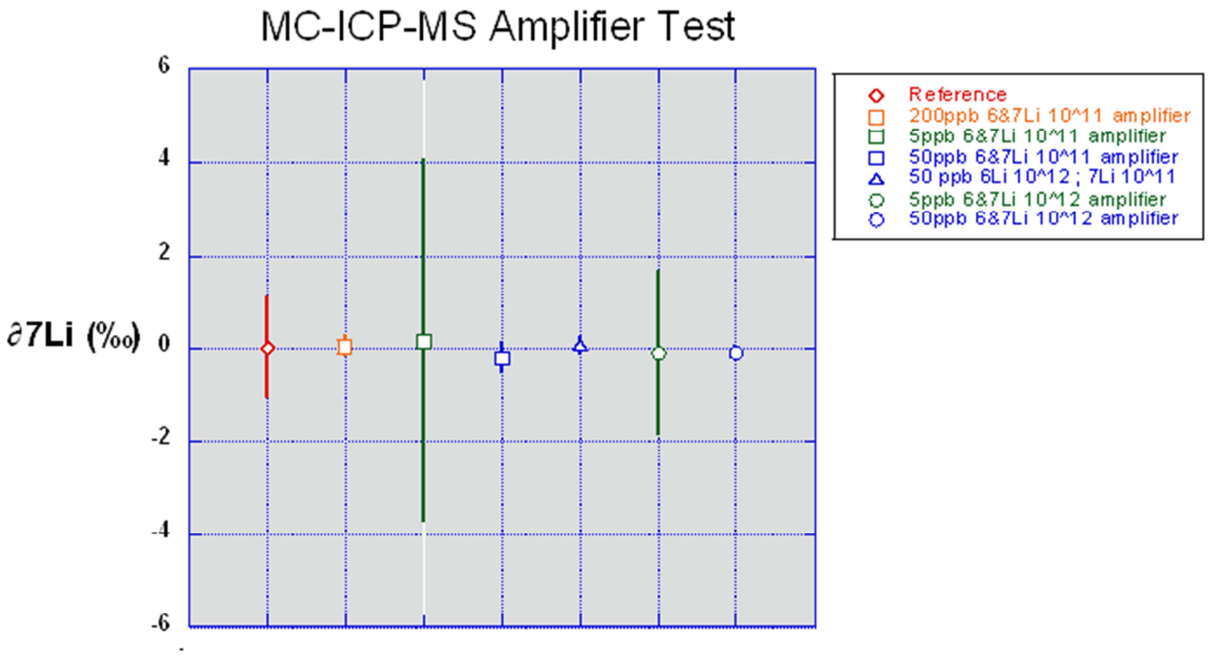

Figure 5-3 graphical representation of the results from the MC-ICP-MS amplifier test, 0.5 µg/l solution is not shown. Uncertainty is two times the standard deviation (s).

Precisions of 0.1 and 0.2 ‰ were obtained for the 50 µg/l solutions lithium in combination with 10^{12} Ω amplifiers for both ^{6}Li and ^{7}Li and a 10^{12} Ω amplifier for ^{6}Li together with a 10^{11} Ω amplifier for ^{7}Li, respectively. Results with ∂^{7}Li precision of 0.2 ‰ were obtained for the 200 µg/l solution lithium in combination with 10^{11}Ω amplifiers. This is shown in Figure 5-3. As the amount of lithium in the clay samples is limited, solutions with 50 µg/l lithium are more representative for the final samples to be analyzed in this work. When looking into more detail at the results for the 50 µg/l lithium

solutions, no substantial differences in accuracy and precision between the different amplifier configurations were observed, although the use of 10^{12} Ω amplifiers can offer an advantage, especially for quantification of ^{6}Li. It was decided to use a 10^{12} Ω amplifier for ^{6}Li detection and a 10^{11} Ω amplifier for ^{7}Li detection.

5.4. Influence of sodium concentration on Li isotope ratios

Measurements of lithium isotopes in ultraclean solutions is preferred to avoid the effect that matrix may exert on the extent of mass bias. In the next chapter, a cation exchange column chromatography technique is described to isolate lithium from its clay matrix. Herein, separation of lithium from sodium is the limiting factor. However, due to contamination or incomplete separation, the presence of sodium in the final samples cannot always be avoided.

Therefore, a sodium tolerance test was performed to determine the highest sodium concentration that does not alter the corrected ∂^{7}Li values by more than ± 0.3 ‰.

5.4.1. Experimental:

5.4.1.1. Reagents and sample preparation

Both standards and samples were prepared from IRMM-016 standard solution and were dissolved in 0.28 M HNO_3. All solutions contained 50 µg/l lithium. The samples were spiked with different concentrations of sodium, ranging from 0 to 20,000 µg/l.

5.4.1.2. MC-ICP-MS measurements

Measurements were performed with a MC-ICP-MS Neptune. Blank solutions were introduced in-between standards and samples. External correction using the sample-standard bracketing approach was used for calculating the corrected ∂^{7}Li values of both bracketing standards and samples. The standard deviation (s) was calculated from all the bracketing standards measured during the experiment (n=25). Instrumental parameters are shown in § 9.5.

5.4.2. Results & discussion

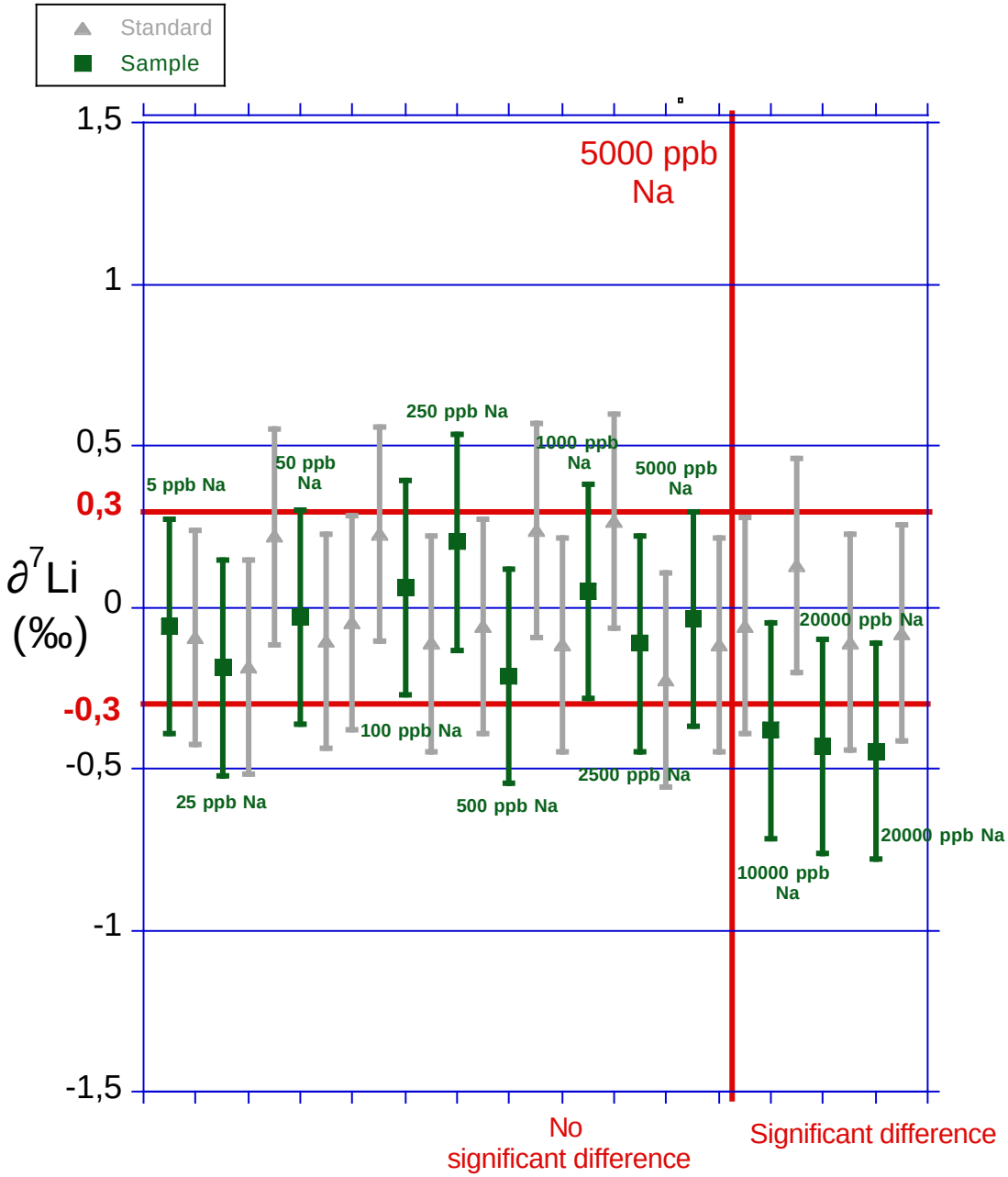

Figure 5-4: grey solid triangles are IRMM-016 standard solutions containing 50 µg/l Li. Green solid squares are IRMM-016 standard solutions containing 50 µg/l Li plus different concentrations of Na, as noted in the figure. Error bars represent two times the standard deviation.

The precision obtained during that measurement day was 0.3 ‰. No significant deviations between the ∂^7Li results for standard solutions and spiked samples, respectively, were found until a concentration of 5,000 µg/l sodium was exceeded. From a concentration of 10,000 µg/l Na onwards, the mean ∂^7Li value obtained for the spiked samples fell outside of the 95 % confidence interval of the pure standard solution, *i.e.* 0.0 ± 0.3 ‰. Nevertheless, the error bars of the standards and all samples still overlap. Though, it is clear that at high concentrations of sodium, the mass discrimination is affected, leading to an erroneous decrease in the measured lithium isotope ratio. This decrease was

also reported by Grégoire et al.(1996) [37], as described in § 5.1.2. and cannot be explained by space-charge effects.

In conclusion, the maximum allowable sodium concentration in samples containing 50 µg/l lithium was set at 5,000 µg/l.

5.5. Summary of chapter 5

An overview of possible sources of bias during ∂^7Li measurement by MC-ICP-MS and how they can be dealt with were described. Several internal correction models were evaluated, i.e. the exponential law, Russell's law, the Baxter-Woodhead approach and CAIS, however, external correction in a standard-sample bracketing approach was found to be the most efficient method, giving rise to best accuracies and precisions. The concentration of Li in the bracketing standards should always have similar (± 30%) concentration as the analyte.

Additionally, a concentration of 50 µg/l lithium was set as a suitable concentration to perform measurements. Considering the detector configuration, the Faraday cup collecting the ^{6}Li signal is best operated with a 10^{12} Ω amplifier, while the ^{7}Li signal can be amplified using a 10^{11} Ω amplifier. Finally, the sodium tolerance test indicated that up to sodium concentrations of 5,000 µg/l in samples containing 50 µg/l lithium no bias in the lithium isotope ratio is to be feared.

6. Column Chromatography

6.1. Introduction

Isotopic analysis via MC-ICP-MS suffers from instrumental mass discrimination and the extent of the phenomenon is affected by the matrix. Therefore, a crucial step in the sample preparation process is the isolation of Li from all matrix elements [53,65–67].

Ion exchange column chromatography is able to provide the necessary separations [53,65–68]. This chapter describes the necessary column calibration and performance checks carried out before loading any actual samples. The calibration was performed with a mixture of digested clay fractions of the samples and has the intention to evaluate if complete isolation of lithium is achieved. The performance check was done with seawater to make sure that ∂^7Li values are consistent with published measurements.

6.2. Principle of cation exchange column chromatography

Chromatography is based on exchange of the analyte between a mobile and a stationary phase.A suitable resin packed in a tube acts as a stationary phase, while the liquid phase running through the tube is called the mobile phase or the eluent. A dissolved sample containing a mixture of cations and anions is introduced on top of the column. The cations in the sample solution can be exchanged with cations of the resin. When a suitable mobile phase runs through the column, remobilizing the cations that show affinity for the stationary phase. The elution order depends on the relative affinity for the stationary phase and the affinity can be influenced by changing the composition of the mobile phase. The rate at which a specific cation passes through the column depends on (1) the resin, (2) the eluent and (3) the cation [69].

6.3. Ion chromatographic isolation of Li: theoretical approach

The isolation of lithium was performed using a single-step cation exchange procedure, based on the principles of Strelow (1960) [70], who described the isolation for large amounts of lithium, in the order of mg to µg [68]. Additionally, Misra & Froelich (2009) [53] developed a procedure for isolation of small amounts of lithium, in the order of ng, giving 100 % recovery [53]. The setup described by Misra & Froelich (2009) [53] was used in this work.

Also other techniques or chromatographic procedures are used as isolation tool for lithium, e.g. solvent extraction [71], multi-stage ion exchange chromatography, *i.e.* by using separate stages of column chromatography wherein the different columns are packed with the same resin [66], inorganic cation exchange, *i.e.* by using an inorganic resin instead of organic resin [72], double column i.e. by using two columns packed with a different resin [73].

$$^{6}Li^{+} + HR \leftrightarrows {}^{6}LiR + H^{+}$$
$$-(^{7}Li^{+} + HR \leftrightarrows {}^{7}LiR + H^{+}) \qquad \text{Eq. 6.1.}$$
$$^{6}Li^{+} + {}^{7}LiR \leftrightarrows {}^{6}LiR + {}^{7}Li^{+} \qquad K > 1$$

Isotopic fractionation process shown as an equilibrium process. ^{6}Li is preferentially retained in the stationary phase. R=Resin, K=equilibrium constant.

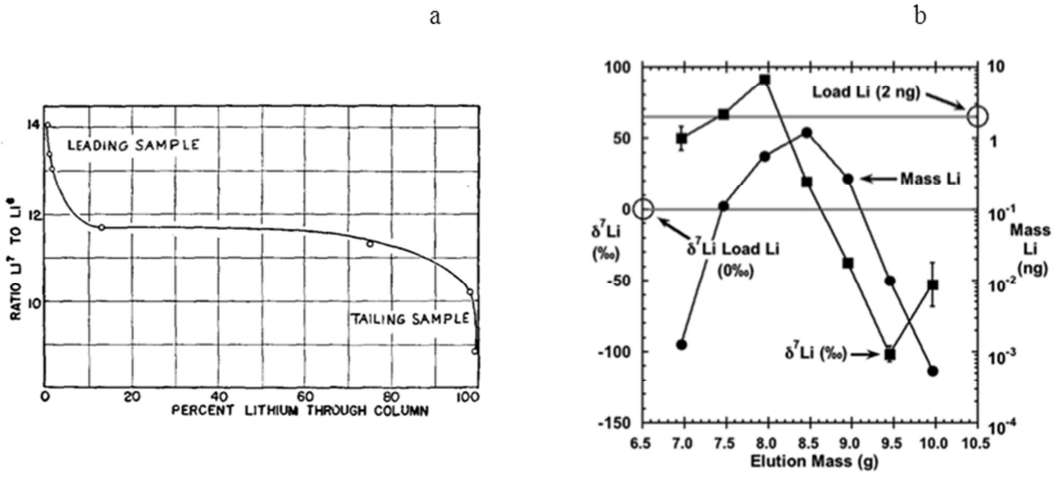

Figure 6-1 (a) from Taylor & Urey (1938) [74]: lithium isotope ratio as a function of fractional elution of lithium. ^{7}Li/^{6}Li of the loaded lithium is 11.7 (b) from Misra (2009) [53]: Lithium isotope ratio as a function of fractional elution of lithium. ∂^{7}Li values are indicated as solid squares.

Quantitative lithium recovery (100%) is crucial since pronounced on-column isotope fractionation occurs during the isolation process. Reactions responsible for the fractionation are shown in Eq. 6.1. The pioneering study by Taylor and Urey (1938) [74] shows that ^{6}Li shows higher affinity towards the stationary phase than ^{7}Li. Therefore, the lithium fraction eluted first is isotopically heavier; this fraction is called the leading sample. The lithium fraction eluted last is isotopically lighter; this fraction is called the tailing sample [74]. This is illustrated in Figure 6-1 (a). The ^{7}Li/^{6}Li ratio of the leading & tailing sample are approximately 14.1 and 8.8, respectively. Hence, a difference of 5.3 in ^{7}Li/^{6}Li ratio was found throughout the Li elution profile. In addition, Misra & Froelich (2009) [53] calculated that the difference in ∂^{7}Li value between the leading and the tailing sample can be as high as 200 ‰ [53], as shown in Figure 6-1 (b). Consequently, if the recovery is less than 100 %, isotopic analysis after the chromatographic separation will not be correct, as it would be affected by an artificial column-induced bias.

The interaction of each cation with the stationary phase and mobile phase can be summarized by the distribution coefficient K_d [75]:

$$K_d = \frac{Amount\ of\ ion\ on\ resin\ x\ volume\ of\ water\ phase\ (ml)}{Amount\ of\ ion\ in\ water\ phase\ x\ gram\ dry\ resin} = \frac{[C_{resin}]}{[C_{water\ phase}]} \qquad \text{Eq. 6.2.}$$

Distribution coefficients are influenced by (1) type of resin, (2) molarity of the acid in the mobile phase, (3) type of acid in the mobile phase and (4) ratio of amount of loaded cations to amount of resin, both expressed as number of equivalents of positive charges (q) [70].

Different resins are on the market, but those most commonly used for cation exchange are listed in Table 6-1 [53,68,70,76,77].

Cation exchange resins are characterized by different specifications & applications [77]. Resins used for isolating lithium are AG 50W-X8/X12, AG MP 50 and BIOREX 70. The resins have different capacities, which affect the amount of cations that can be exchanged. The AG 50W resin, which was used throughout this work, is available with various degrees of crosslinking. Less crosslinking indicates a more open structure of the resin. Also, the AG 50W resin is available in different mesh sizes. The mesh size is a unit for the particle size of the resin, where higher mesh size resins are characterized by smaller particles, have lower flow rates and offer higher chromatographic resolution [78].

Table 6-1: specifications ion exchange resins.

Specifications ion exchange resins				
Resin	**Crosslinkage**	**Min. Wet Capacity (meq/ml)**	**Ionic Form**	**PH Range**
AG 50W	2,00%	0,60	Hydrogen	0-14
	4,00%	1,1	Hydrogen	0-14
	8,00%	1,7	Hydrogen	0-14
	12,00%	2,1	Hydrogen	0-14
AG MP-50	Macroporous	1,5	Hydrogen	0-14
BIO REX 70	Macroreticular	2.4	Hydrogen	5-14

The molarity of the mobile phase has a large influence on the distribution coefficients. With increasing molarity of the eluent, K_d decreases [70,79]. This can be seen in table 6.2. A stronger competition between the cations of the sample and the H^+ in the mobile phase occurs with increasing molarity. As a result, the amount of cations in the mobile phase increases and K_d decreases.

The type of acid plays a role in complex formation and ion pairing. With HCl, distribution coefficients of Hg^{2+}, Cd^{2+}, Fe^{3+} and Mg^{2+} will be lower than when using HNO_3 due to complex formation of these ions with Cl^-. Lower values of K_d for Ca^{2+}, Sr^{2+} and Ba^{2+} in HNO_3 compared to HCl are explained by a higher amount of ion pair formation with NO_3^- than with Cl^-. Nevertheless, there is still an increase in the amount of cation in the mobile phase with higher molarities of acid [70,79].

The distribution coefficient K_d is used for calculating the eluted volume ($\bar{v}$) corresponding with maximum peak height of the cation of interest [70,75].

$$\bar{v} = K_d \, x \, (mass \; of \; dry \; resin \; in \; the \; column) \qquad \text{Eq. 6.3.}$$

The ratio of cations in equivalents between load and resin, q, also changes the K_d values. In general, a decrease of q, gives an increase of K_d. For K_d values below 20, the influence of q is rather small, but K_d values around 50 tend to change a lot with changing q. So, as the total amount of cation loaded on the column increases, a shift occurs in the position of the elution maxima towards lower elution

volumes. This effect is more pronounced for elements with higher K_d values. On the other hand, the tail of the elution curve stays on the same position in the elution profile. Hence, increasing the total cation load with the same amount of resin and composition of the eluent, will give rise to broader and unsymmetrical peaks, this is shown in Figure 6-2. This phenomenon is called tailing.

In practice, ion selectivity stays unaffected if the amount of cation equivalents of the sample load is less than 0.1 times the total amount of equivalents of the resin [80]. In other words, sample load must not exceed 10 % of the column capacity.

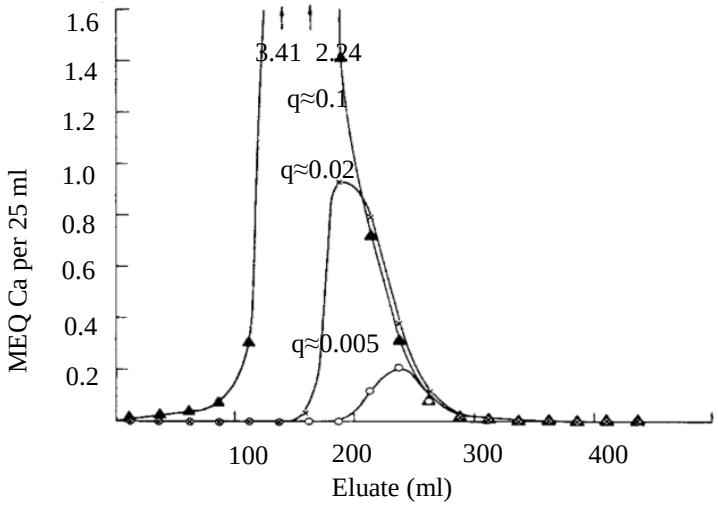

Figure 6-2: from Strelow (1960) [70]. effect of increasing load on the chromatographic peak.

In addition, the separation factor indicates how well peaks of different cations are separated.

$$\alpha = \frac{K_d^{c1}}{K_d^{c2}} = \frac{v_1}{v_2} \qquad \text{Eq. 6.4.}$$

The higher the separation factor, the better the cations of different elements can be separated. When working with inorganic acids, such as HCl or HNO_3, distribution coefficients of lithium are slightly lower than those of sodium [66,70,79], therefore $\alpha_{Li,Na}$ values are slightly larger then 1, indicating that Na^+ is eluted after Li^+ [37,66,81]. As the separation factors between lithium and other elements are higher [70,79], a successful Li isolation always depends on whether complete separation between Li^+ and Na^+ can be accomplished.

Although the separation factors of lithium and sodium are not affected to a large extent by varying the molarities, the elution volume corresponding to maximum peak height does. This is shown in Table 6-2 with data from Strelow (1960) [70], calculated with Eq. 6.3. and 6.4.

Table 6-2: different influences of the molarity of the inorganic acid on sodium and lithium. Used distribution coefficients are from Strelow (1960) [70]. Full data available in § 9.6.

Kd values at different molarities of hydrochloric acid

	Molarity HCl				
Element	**0.1**	**0.2**	**0.5**	**1**	**2**
Sodium	52	28.3	12	5.59	3.6
Lithium	33	18.9	8.1	3.83	2.5

Eluted volume at maximum peak height v̄ (ml) at different molarities of hydrochloric acid

	Molarity HCl				
	0.1	**0.2**	**0.5**	**1**	**2**
v̄Na	520	283	120	55.9	36
v̄Li	330	189	81	38.3	25
v̄Na - v̄Li	190	94	39	17.6	11

Separation factor α at different molarities of hydrochloric acid

	Molarity HCl				
	0.1	**0.2**	**0.5**	**1**	**2**
$\alpha_{Li\text{-}Na}$	1.58	1.50	1.48	1.46	1.44

As the molarity of the inorganic acid increases, the distance between the Li^+ & Na^+ peaks decreases and the eluted peaks become sharper [81].

Also the separation factor α decreases slightly with stronger inorganic acid, as can be seen in Table 6-2. It has been demonstrated that variations in α values are small between various inorganic acids [70,79,82]. Separation factors can be increased by a factor of 2 to 3 by working with a mixture of inorganic acids and organic compounds, such as acetone, ethanol or methanol [83]. Although the separation factors increase, some negative effects appear, *i.e.* (1) faster degradation of the resin, (2) unstable distribution coefficients leading to migration of the peaks, (3) high and variable lithium and sodium blanks and (4) larger eluent volumes further increasing lithium blanks [53,66,73,84,85]. Therefore, it was decided not to use organic solvents for lithium isolation.

6.4. Ion chromatographic isolation of Li: experimental

6.4.1. Eluent preparation

Double-distilled hydrochloric acid, used for calibrating, conditioning and eluting of the columns, was prepared from reagent grade HCl (Fischer). It was diluted to a concentration of 0.5 M.
Hydrochloric acid Optima® 6M was used for pre-washing the columns.

6.4.2. Column specifications

Table 6-3 Column characteristics and specifications

Column Characteristics	Specifications
Column material	Teflon® (Savillex®) columns with Teflon® frits
Internal diameter	3.2 mm
Resin type	AG 50W-X8 (100-200 mesh size)
Resin volume	2.0 ml (wet)
Resin capacity	3.4 meq (1.74 meq/ml wet capacity)
Resin height	250 mm
Resin mass	1.6 g
Eluent flow rate	0.025 ml/min
Load volume	22 µl to 108 µl (dissolved individual clay samples) 50 µl to 125 µl (column calibration)
Equivalent load	0.0041 meq to 0.0307meq
Pre-wash	6 M HCl (6 ml)
Conditioning	0.5 M HCl (6 ml)
Load matrix	0.5 M HCl
Elution matrix	0.5 M HCl
Li fraction	5 ml to 10 ml
Operational temperature	20 °C

Teflon® columns with Teflon® frits with an internal diameter of 3.2 mm and a height of 250 mm were packed with 2 ml of Bio Rad® AG 50W–X8 (100-200 mesh size) cation exchange resin in the hydrogen form. The resin consists of a styrene/divinylbenzene copolymer lattice to which sulfonic acid functional groups are attached [78]. The total capacity of the resin is 3.4 meq (1.74 meq/ml). Cation equivalents of the loaded samples are less than 1 % of the capacity of the total resin, as shown in Table 6-4. The total sample cation loads were estimated using the elemental composition of each clay fraction as determined in chapter 4. Elements taken into acount were Li, Na, Mg, Al, P, K, Ca, Sc, Ti, Cr, Mn, Fe, Co, Ni, Cu, Sr and Y. All total cation equivalent loads were calculated by taking the highest oxidation state into account. Nine columns were calibrated, eight of which were used for final sample treatment.

Table 6-4: mili-equivalent of loaded samples. P1/FPL and P2/PFL were concentrated 6.5 times. F3/FDO was diluted 2 times.

Capacity of loaded samples

Name	Load volume (µl)	Meq	Percentage of 3.4 meq
P1/FPL	50	0.0299	0.881
P2/FPL	50	0.0226	0.664
P3/FPL	65	0.0131	0.384
P4/FPL	82	0.0147	0.432
P5/FPL	107	0.0142	0.417
P6/FPL	91	0.0134	0.394
K7/FPL	89	0.0129	0.380
K8/FPL	85	0.0132	0.387
K10/FPL	87	0.0142	0.417
K11/FPL	84	0.0126	0.371
K12/FPL	57	0.0145	0.426
F1/PTC	21	0.0220	0.647
F2/FPL	21	0.0097	0.284
F3/FDO	22	0.0041	0.120

Empty columns were first washed with methanol and Milli-Q water. Packed columns were pre-washed with 6 ml of 6 M HCl, then back-washed with Milli-Q water and conditioned with an additional 6 ml of 0.5 M HCl. First, a column calibration was performed using mixtures of dissolved clay fractions of the samples, followed by seawater to evaluate if correct ∂^7Li values were obtained. Finally, the clay fractions of the samples were loaded one or two times. Pre-wash, back-wash and conditioning was always performed in-between every sample loading.

6.4.3. General overview of sample processing

An overview of the different steps, the samples processed and analyses performed on various fractions is provided in Figure 6-3. Starting with the (1) the column calibration, performed with various mixtures of the clay fractions of the samples; proceeding with (2) the performance check, performed with Sargasso seawater samples; and ending with (3) the clay fractions of the samples. The overview is a guideline for this and the next chapter.

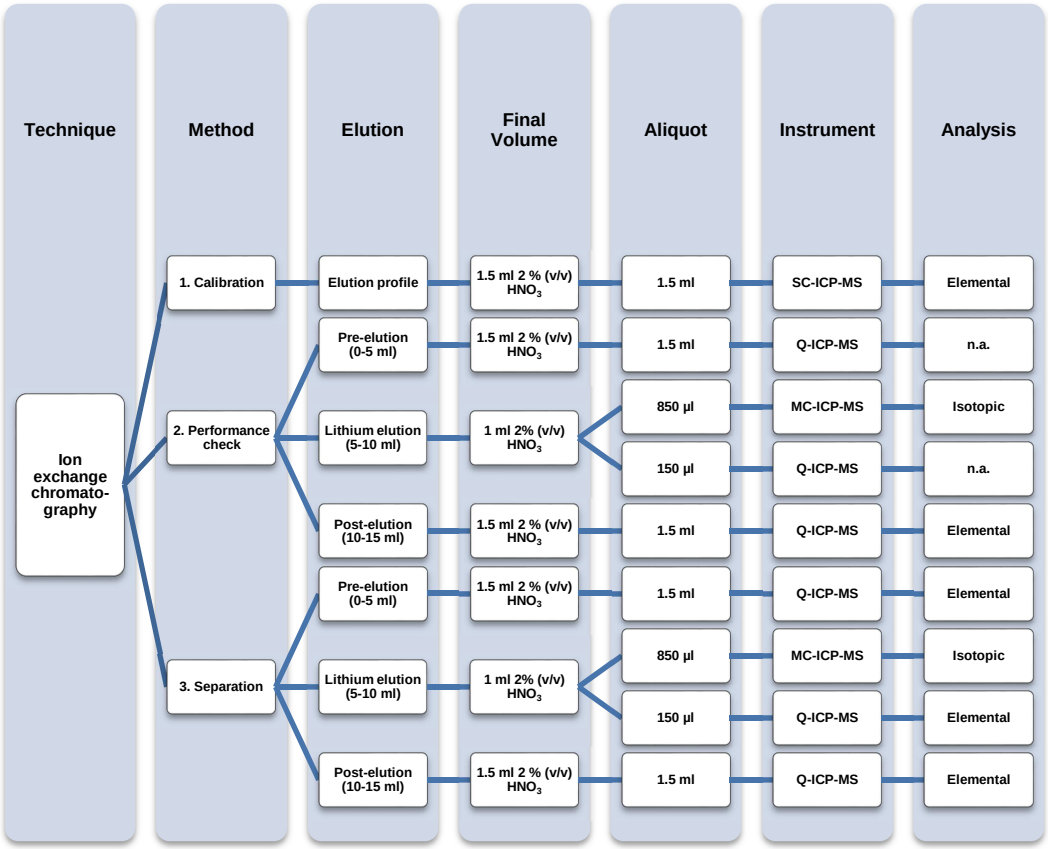

Figure 6-3, graphical overview of column chromatography experiments performed in this work and subsequent analysis of collected fractions

6.4.4. Column Calibration & seawater load

Column calibration is the first step in the procedure of the isolation of lithium from its clay matrix. Column calibration is necessary to determine whether (1) complete separation of Li^+ from Na^+ can be accomplished and (2) the fraction intended for lithium analysis contains 100 % of the loaded Li^+ within that elution volume. In a second experiment, lithium was isolated from seawater in order to compare the obtained ∂^7Li values with the published values.

6.4.5. Column Calibration

6.4.5.1. Experimental

6.4.5.1.1. Column loading

In total, nine columns were loaded with digested clay fractions, *i.e.* three with a mixture of 'P clays' solution, three with a mixture of 'K clays' solutions and three with either F1, F2 or F3 KT boundary clay solution. The solutions of clay fractions were prepared as described in chapter 4. Mixture P was a mixture of 50 µl of each of the digested clay fractions of the samples from the Paleogene (P/FPL) and 50 µl of 0.5 N HCl. Mixture K was a mixture of 50 µl of each of the digested clay fractions of the samples from the Cretaceous (K/FPL), except for the clay fraction of sample K9/FPL, and 100 µl of

0.5 N HCl. Of each mixture, 3 different volumes, 50, 100 and 125 µl, were loaded on three different columns for column calibration.

During column calibration, elution fractions of 0.5 ml or 1 ml (depending on the elution fraction) were collected in 7 or 15 ml acid-cleaned Teflon® beakers. Based on analysis of these individual fractions, an elution profile could be constructed (see further).

The collected elution fractions were evaporated to dryness on a hotplate at 80°C and re-dissolved in 1.5 ml of 0.28 M HNO_3. All steps were performed under class-100 clean lab conditions.

6.4.5.1.2. SC-ICP-MS measurements

Lithium and sodium concentrations in the eluted fractions were determined with a SC-ICP-MS, element XR.

Measurements were performed under class-100 clean lab conditions with a 1250 W RF hot plasma and a Scott-type spray chamber. The sample aspiration rate was 50 µl/min.

6.4.5.2. Results and Discussion:

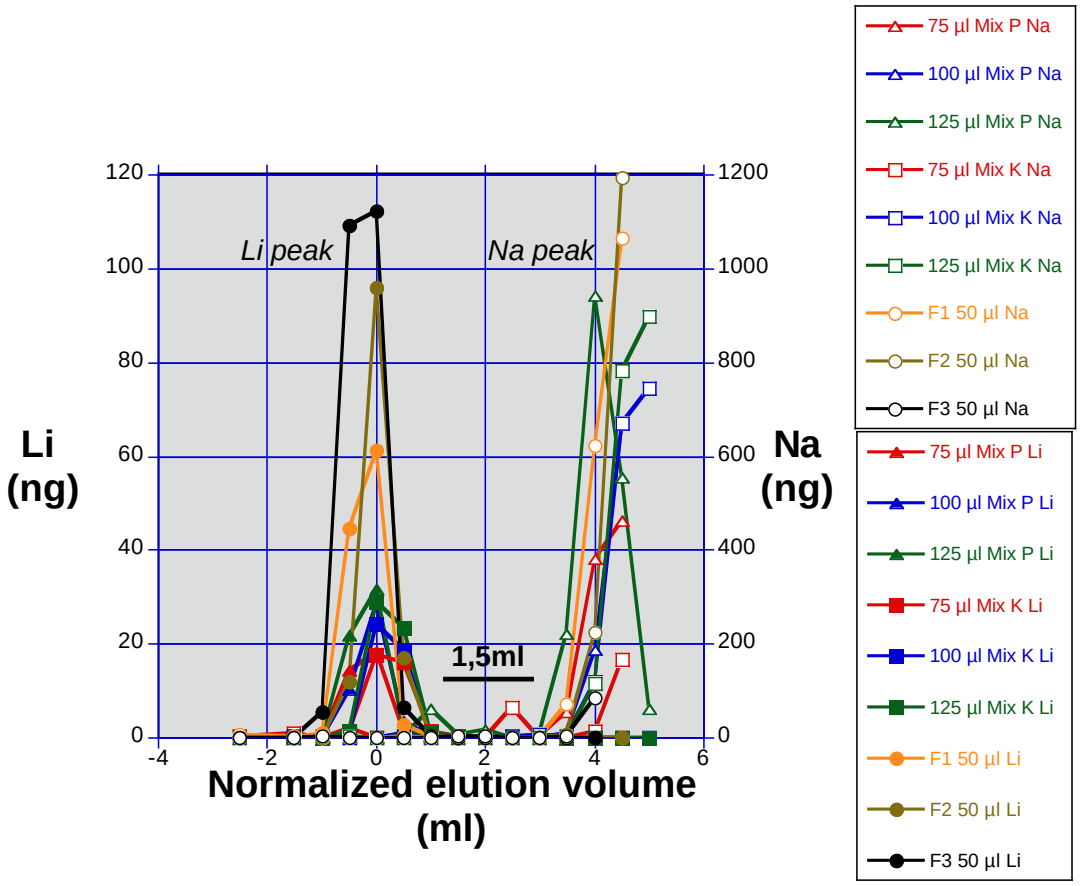

Figure 6-4: elution profile - the peaks are normalized, so that the lithium peak of each column is at volume 0. Open symbols refer to sodium, solid symbols refer to lithium. Triangles refer to samples of mixture P, squares refer to samples of mixture K and circles refer to samples of the K/T boundary.

By performing the column calibration, a detailed picture of the elution profile per column was constructed, as shown in Figure 6-4. It is clear that every column has a minimum separation of 1.5 ml between the lithium and sodium peak, hence complete isolation of lithium was accomplished. From this experiment, it could be concluded that the pre-elution fraction had a volume of 5 ml, the lithium fraction elutes between 5 and 10 ml and the post-elution fraction starts from 10 ml of eluent volume on. No differences were measured between the profiles of the different loads, except for column three (125 µl mixture P), where the sodium peak (open green triangles) eluted earlier during the column calibration. Also, the flow rate of this column was very low and therefore, this column was no longer used in further work.

Due to time constraints, no complete elution profile of the sodium peak was measured. Therefore, no exact values for $\bar{v}_{Na}$ were calculated and no separation factors could be determined, cf. Eq. 6.3.

Columns three and four gave a slight sodium peak in between the lithium and main sodium peak. These small peaks were probably related to the fact that only one aliquot of 6 M HCl was loaded during the pre-wash before the very first sample load, *i.e.* the column calibration.

The columns were pre- and back-washed and conditioned before loading the seawater samples.

6.4.6. Seawater loads

Seawater samples were loaded at two different stages of column chromatography work, *i.e.* once, using all columns, right after the column calibration, and a second time, using three columns, after the columns had been loaded with several clay samples and had been regenerated.

6.4.6.1. Experimental

6.4.6.1.1. Sample treatment

Sargasso seawater was used as sample. The original stock solution contained 175 µg/l lithium, corresponding to ocean water concentration. It was first pre-concentrated 3.5-fold through evaporation on a hotplate. The pre-concentration step was necessary to achieve a small load volume (60 µl) containing a sufficient mass of Li (36.8 ng).

For each replicate, 60 µl of concentrated Sargasso seawater containing approximately 35 ng lithium was loaded onto the columns. Pre-, lithium- and post-elution fractions were collected in acid cleaned Teflon® beakers.

Eluted fractions were evaporated to dryness on a hotplate at 80°C (sub-boiling temperature) and re-dissolved in 1.5 ml of 0.28 M HNO_3. Lithium concentrations were determined in both pre- and post-elution fractions, while sodium concentration was determined in the pre-elution fraction only, using Q-ICP-MS. The lithium isotopic composition of the lithium-elution fraction was determined using a MC-ICP-MS Neptune

6.4.6.2. Results

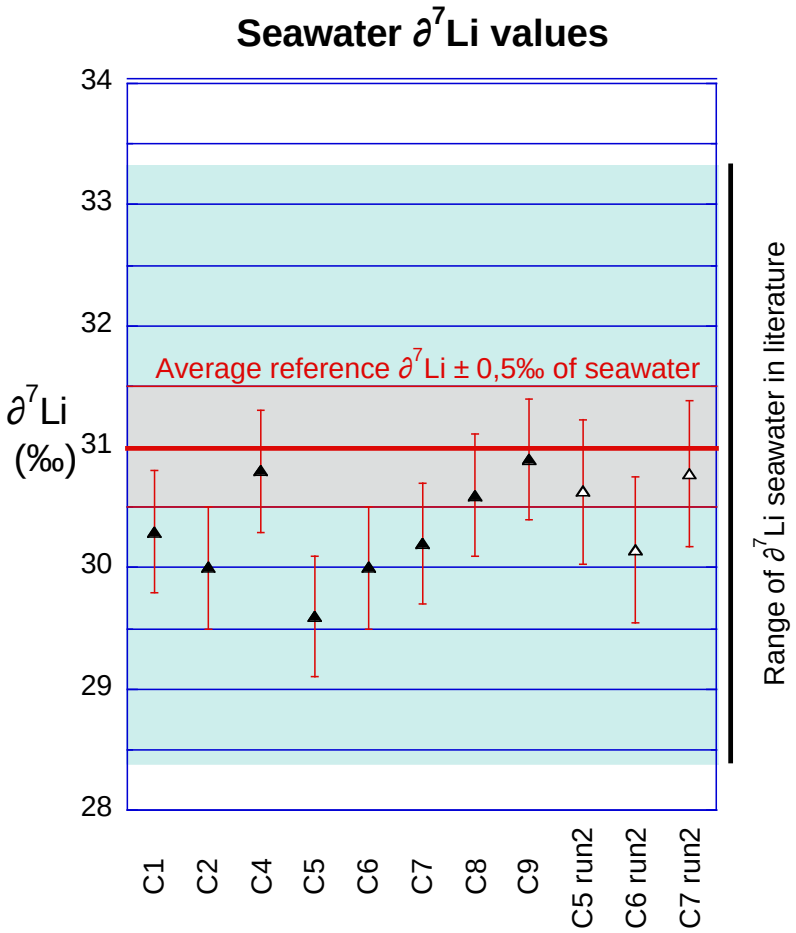

Figure 6-5: ∂^7Li values obtained in Sargasso seawater according to column number.
Solid triangles are columns loaded in run1, open triangles are columns loaded in run 2.
Error bars are two times the instrumental standard deviation (2s)

The ∂^7Li value of current seawater measured by MC-ICP-MS reported in the literature ranges from 29.0 ± 0.6 ‰ to 31.8 ± 1.8 ‰, as indicated by the blue interval in Figure 6-5. The use of different lithium isolation procedures can explain this relatively wide range reported in literature [12]. In general, 31.0 ± 0.5 ‰ is taken as an average reference value, indicated as grey interval in Figure 6-5 [12].

In every pre-elution fraction, the lithium concentration was below the limit of quantification, *i.e.* 0.2 µg/l. The limit of quantification for sodium was 2 µg/l. Significant sodium concentrations in pre-elution fractions of columns C1, C2, C5, C6 were 5.1, 10.0, 71.2 and 16.0 µg/l, respectively.
In every post-elution fraction, except for C5, lithium was below the limit of quantification. The post-elution fraction of C5 contained 0.31 ng of Lithium. This is approximately 0.9 % of the total amount of lithium loaded on the column.

6.4.6.3. Discussion

The ∂^7Li value determined in lithium elution fractions was situated within the range of ∂^7Li values reported in the literature. Only using column C5, a significantly lower ∂^7Li value (29.6 ± 0.5 ‰.) was found for seawater compared to the other columns. A possible explanation could be anomalies, such as air bubbles or breakthrough of sodium, within the deviating column. In addition, approximately 0.9 % of the lithium was eluted in the post-elution fraction. As stated in § 6.3, the last part of the lithium elution peak is expected to be relatively enriched in ^{6}Li. Hence, not capturing this fraction should give a higher ∂^7Li signal in the lithium-elution fraction, but this is in contrast with our result. On the other hand, the pre-elution fraction of C5 contained highest sodium concentration (71 µg/l), which could indicate a breakthrough of sodium and possibly also other elements. Therefore, it is possible that the sodium concentration in the lithium-elution fraction was higher than 5 mg/l. Such high concentrations of sodium in lithium-elution fractions have been shown to result in a negative bias on ∂^7Li values as shown in § 5.4.2. Unfortunately, sodium concentration in the lithium-elution fraction of the seawater samples was not determined.

As seawater can be considered as a very concentrated NaCl solution (± 35 g/l) with extremely high matrix load, it represents a worst case scenario for the clay fractions of the samples.

6.5. Summary of chapter 6

An overview of the theoretical background necessary to understand the fundamentals of a single-step cation exchange chromatography was provided. A lithium recovery of 100 % is crucial to avoid artificial on-column isotope fractionation. To maintain ion selectivity, sample loads should be less than 10 % of the column capacity. The concentration of the inorganic acid has a major influence on the elution volumes of the cations. The separation factor is less influenced by the concentration of the inorganic acid. Mixtures of organic solvents and inorganic acids are able to improve the separation factor, but several negative effects can influence the performance of the column. The theory was applied to the isolation of lithium out of a clay matrix. Furthermore, a detailed description of the columns used for the isolation procedure was given.

The most important conclusion of this chapter was the achievement of a separation of 1.5 ml between the lithium and sodium peak in the elution profile of clay fractions. Based on the column calibration experiment, adequate volumes of the pre-, lithium- and post-elution fractions were determined.

The performance of the chromatographic procedure was evaluated using seawater samples, which can be regarded as a worst case matrix for isolation of lithium from sodium. It was concluded that the chromatographic procedure works satisfactorily. The range in ∂^7Li obtained for seawater values falls within the range of published values. Hence, it was decided that the columns could be used to isolate lithium from the actual clay samples.

7. Analysis of the Furlo Pietralata clay fraction of the samples.

This chapter presents the isotopic composition of the lithium present in the clay fractions of the samples. The results are discussed and a possible interpretation is provided. In addition, the occurrence of memory effects was discovered, a short discussion is provided.

7.1. Experimental

The sample pre-treatment was carried out as described in chapter 5. The isolation of lithium using column chromatography was carried out as described in the previous chapter.

7.1.2. Sample treatment

Of each sample, 50 ng lithium in 0.28 M HCl medium was loaded onto a column. Because each sample contained a different concentration of lithium, the specific volumes loaded varied from sample to sample, within a range of 22 µl to 108 µl. Two replicate digests of the samples P4, P5, P6, K7, K8, K10, F1, F2, F3 were prepared. The total elution volume was 15 ml of 0.5 M HCl, divided into 5 ml fractions of pre-, lithium- and post-elution. All fractions were captured in acid-cleaned Teflon® beakers. The 5 ml fractions were evaporated on a hotplate at 80°C. All evaporations were performed under class 100 clean lab conditions at the department of Earth Sciences of the University of Cambridge. All re-dissolution steps were performed under class 10 clean lab conditions at the department of Analytical Chemistry of Ghent University.

As shown in Figure 6.3, pre- and post-elution fractions were re-dissolved in 1.5 ml of 0.28 M HNO_3. The pre-elution fraction was checked for the absence of lithium and sodium, whereas the post-elution fraction was only used for lithium concentration determination. An *X-Series 2* quadrupole-based ICP-MS instrument was used for the elemental analyses. In both cases, Be (30 µg/l) was added as an internal standard to all blanks, standards and samples. The instrumental parameters used are shown in § 9.7. Lithium elution fractions were re-dissolved in 1 ml of 0.28 M HNO_3. This final sample was divided in two aliquots: one for determining Li and Na concentrations and the other for determining the isotopic composition. The first aliquot, 150 µl, was diluted with 0.28 M HNO_3 to a total volume of 1.5 ml in acid-cleaned 15 ml centrifugation tubes *(VWR International®, trace metal grade).* The remaining 850 µl was directly used for isotopic analysis using the Neptune MC-ICP-MS instrument.

On each of the two MC-ICP-MS measurement days, 50 ml of a 48 µg/l IRMM-016 lithium isotopic standard was prepared in 0.28 M HNO_3 and used as bracketing standard throughout the measurement day. In addition, each measurement sequence contained 8 aliquots of this standard solution for validation purposes. These aliquots were thus considered as additional samples. All results agreed with the reference value of the IRMM-016 isotopic reference material (*i.e.* 0.0 ± 1.1 ‰) within experimental uncertainty. The results and measurement sequence are shown per day in § 9.7.

The precision on determined isotope ratios was determined on a daily basis. It was calculated as two times the standard deviation (s) of the ∂^7Li value obtained for all bracketing standards analysed during a specific day (typically n = 26). Instrumental parameters are shown in § 9.7.

7.2. Results

7.2.1. Memory effects

During MC-ICP-MS measurements, memory effects were discovered, resulting in high background signals varying between 20 mV and 45 mV. In a first attempt to overcome the memory effects, air was introduced into the plasma instead of blank solution, thus creating a dry plasma. An increase in the lithium signal was found during this "burn-off". Afterwards, the blank solution was introduced again and the observed Li signal intensity had decreased. This procedure was tested both during tuning as during an actual measurement series. § 9.7. shows the effect during measurements and during tuning. Unfortunately, memory effects again increased after standard introduction.

7.2.2. Results of the Furlo Pietralata clay fraction of the samples

Table 7-1: concentration of Li in pre-, lithium-, post-elution fractions for both runs. LOQ = 0.2 µg/l. The lithium-elution fractions were 10-fold diluted before analysis.

Lithium concentration

			Pre-elution		Lithium-elution		Post-Elution	
Sample	**Depth (m)**	**Load volume**	**Run 1 Li (µg/l)**	**Run 2 Li (µg/l)**	**Run 1 Li (µg/l)**	**Run 2 Li (µg/l)**	**Run 1 Li (µg/l)**	**Run 2 Li (µg/l)**
P1/FPL	5.0	50 µl	<LOQ	<LOQ	77	62	<LOQ	0.6
P2/FPL	4.0	50 µl	<LOQ	n.a.	62	n.a.	<LOQ	n.a.
P3/FPL	3.0	65 µl	<LOQ	n.a.	46	n.a.	<LOQ	n.a.
P4/FPL	2.0	82 µl	<LOQ	<LOQ	49	49	<LOQ	<LOQ
P5/FPL	1.0	107 µl	<LOQ	n.a.	48	47	<LOQ	<LOQ
P6/FPL	0.1	91 µl	<LOQ	<LOQ	47	47	<LOQ	<LOQ
F2/FPL	0.0	21 µl	<LOQ	<LOQ	50	49	<LOQ	<LOQ
K7/FPL	-0.1	89 µl	<LOQ	<LOQ	48	47	<LOQ	<LOQ
K8/FPL	-1.0	85 µl	<LOQ	<LOQ	48	45	<LOQ	<LOQ
K9/FPL	-2.0	50 µl	<LOQ	n.a.	45	n.a.	n.a.	n.a.
K10/FPL	-3.0	87 µl	<LOQ	<LOQ	47	46	<LOQ	<LOQ
K11/FPL	-4.0	84 µl	<LOQ	n.a.	48	n.a.	<LOQ	n.a.
K12/FPL	-5.0	57 µl	<LOQ	<LOQ	47	46	<LOQ	<LOQ
F1/PTC	0.0	21 µl	<LOQ	<LOQ	47	46	<LOQ	<LOQ
F3/FDO	0.0	22 µl	<LOQ	<LOQ	50	48	<LOQ	<LOQ

Lithium was present below the LOQ in the pre-elution fractions. In the post-elution fractions, lithium was found only in the second replicate of P1/FPL. It was less than 1 % of the total amount of lithium. As stated in §6.3, the last part of the lithium elution peak is enriched in ^{6}Li. Not capturing this fraction should hence result in a slightly higher $\partial^{7}Li$ value in the lithium-elution fraction. The $\partial^{7}Li$ signal of P1/FPL (run 2) could therefore be erroneously heavier.

Sodium concentrations were below the 5,000 µg/l threshold in all lithium fractions of the clay samples. Therefore, no errors in the $\partial^{7}Li$ values were expected due to sodium contamination in the final samples. In §9.7., the amount of lithium present in the elution fractions is shown.

Table 7-2: concentration of Na in lithium-elution fractions. LOQ = 2 µg/l for sodium. Lithium isotopic composition in lithium-elution fraction. Error bars are two times the standard deviation (2s).

Lithium-elution

			Sodium concentration		Lithium isotopic composition	
Sample	**Depth (m)**	**Load volume**	**Run 1 Na (µg/l)**	**Run 2 Na (µg/l)**	**Run 1 $\partial^{7}Li$ (‰)**	**Run 2 $\partial^{7}Li$ (‰)**
P1/FPL	5.0	50 µl	200	<LOQ	-3.5 ± 0.5	-1.8 ± 0.4
P2/FPL	4.0	50 µl	<LOQ	n.a.	-0.9 ± 0.4	n.a.
P3/FPL	3.0	65 µl	<LOQ	n.a.	-2.6 ± 0.5	n.a.
P4/FPL	2.0	82 µl	<LOQ	<LOQ	-2.6 ± 0.5	-2.7 ± 0.5
P5/FPL	1.0	107 µl	<LOQ	<LOQ	-2.7 ± 0.5	-2.3 ± 0.5
P6/FPL	0.1	91 µl	<LOQ	<LOQ	-1.4 ± 0.4	-1.7 ± 0.4
F2/FPL	0.0	21 µl	<LOQ	<LOQ	-4.6 ± 0.5	-3.1 ± 0.5
K7/FPL	-0.1	89 µl	<LOQ	<LOQ	-2.2 ± 0.5	-2.2 ± 0.5
K8/FPL	-1.0	85 µl	<LOQ	<LOQ	-1.7 ± 0.4	-1.6 ± 0.4
K9/FPL	-2.0	50 µl	760	n.a.	-1.6 ± 0.5	n.a.
K10/FPL	-3.0	87 µl	<LOQ	<LOQ	-1.3 ± 0.4	-2.0 ± 0.4
K11/FPL	-4.0	84 µl	<LOQ	n.a.	-2.3 ± 0.5	n.a.
K12/FPL	-5.0	57 µl	<LOQ	112	-2.0 ± 0.5	-1.9 ± 0.4
F1/PTC	0.0	21 µl	710	<LOQ	-6.8 ± 0.5	-4.0 ± 0.5
F3/FDO	0.0	22 µl	<LOQ	<LOQ	-5.1 ± 0.5	-5.6 ± 0.5

Run 1 chromatography
Run 2 chromatography

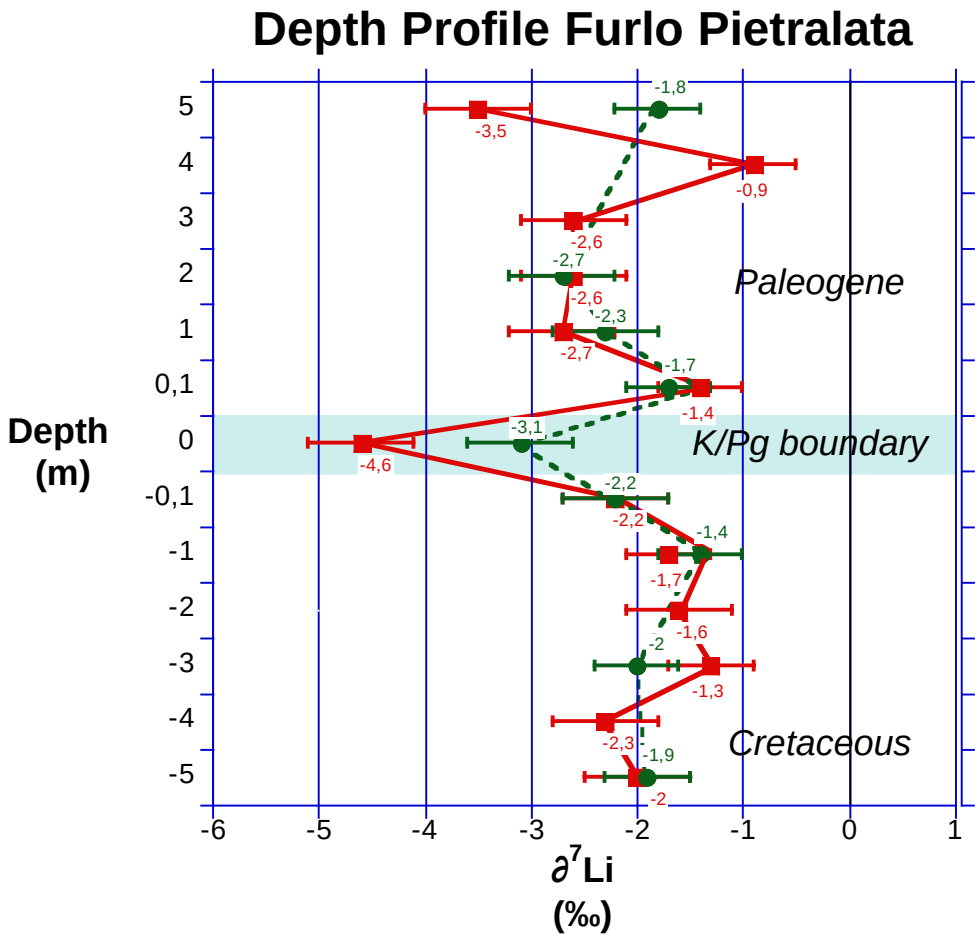

Figure 7-1: Depth profile of Furlo Pietralata clay fraction in terms of ∂^7Li. Red squares represent results of run 1, green circles represent results of run 2. At 0 m, the K/Pg boundary is indicated by the blue background. Below the K/Pg boundary, samples originated from the Cretaceous, above the K/Pg boundary, samples originated from the Paleogene. Precision is two times the standard deviation.

Both run 1 (red squares) and run 2 (green circles) indicated a negative deviation in ∂^7Li exactly at the K/Pg boundary. The negative peak was more pronounced during the first series of samples subjected to ion exchange chromatography (run 1), compared to the second set of samples (run 2). Hence, the analytical uncertainty of the K/Pg boundary samples did not overlap. Unfortunately, no specific reason for this significant difference in ∂^7Li values between the two K/Pg boundary samples can be given, as no breakthrough of sodium, neither fronting or tailing of lithium was observed.

In run 1, a significant difference was observed between the clay of the K/Pg boundary and the clay fraction just above and just below the K/Pg boundary. In run 2, the difference between the clay of the K/Pg boundary and the clay fractions of the Paleogene is significant, but between the Cretaceous and K/Pg clay fractions the error bars overlap.

For the sample taken at + 5 m (P1/FPL), a significant difference between the two duplicates was found. Two facts may be at the basis of this difference. The lithium concentration in P1/FPL (run 1)

was ~54% higher than the concentration of the bracketing standard. This difference in target element concentration could have affected the extent of mass discrimination and thus, the accuracy of the result, as shown by Grégoire et al (1996). [37] and by Sun et al. (1987) [60], cf. § 5.1.2. On the other hand, an elevated presence of lithium was found in the post-elution fraction of run 2 of the clay at +5 m (P1/FPL), as shown in Table 7-1. Therefore, the ∂^7Li signal reported in Figure 7-1 is probably elevated as isotope fractionation results in ^{6}Li being eluted somewhat slower than ^{7}Li, as described in § 6.3. The concentration in run 1 P1/FPL was also slightly elevated compared to the bracketing standard but fitted within the ± 30 % deviation, cf. §5.2.1. The effect of violating the "± 30 % deviation" recommendation was specifically not tested for lithium and therefore further experimental work is required. At all other depths, a sufficiently good agreement was found between the duplicates.
As explained in chapter 4, also two other K/Pg boundary samples from the Umbria-Marche sequence (F1/PTC, F3/FDO) were investigated. A good agreement was found between the two runs of F3/FDO. The boundary samples also showed a negative ∂^7Li shift compared to the values of Paleogene and Cretaceous clay fractions of FPL.
No samples of the Paleogene and Cretaceous originating from PTC and FDO sites are measured, but they are expected to be similar to these of the upper continental crust (0 ± 2 ‰). In addition, when comparing the ∂^7Li values of F1/PCL (-6.7 ± 0.6 ‰; -4.1 ± 0.6 ‰) and F3/FDO (-5.1 ± 0.6 ‰; -5.6 ± 0.6 ‰) to the ∂^7Li values of the upper continental crust (0 ± 2 ‰) [15], a significant negative shift of these K/Pg boundary clays to the upper continental crust is found. Therefore it is expected that these highly negative ∂^7Li values of the K/Pg boundary clays show a negative ∂^7Li spike compared to the corresponding Paleogene and Cretaceous clay fractions, and thus could indicate high weathering intensities. Hence, a specific study of the depth profile of the PTC and FDO locations will indicate if there is also a peak at the K/Pg boundary.

7.3. Geological interpretation

The negative ∂^7Li shift located at the K/Pg boundary is believed to be the result of increased continental weathering. As this increased weathering and the extra-terrestrial impact are of the same age, showed by the iridium anomaly found in the clays by Goderis et al. (2013) [44].

Schulte et al. (2010) [40] described that the impact changed the environmental situation on our planet significantly. The release of toxic and acid gases, extended darkness, climate change and acid rain are believed to result from the impact [12,38,40,46]. High volcanic activity in the Deccan traps (India) is believed to be a complementary source for acid rain [12,40].
It is believed that darkness as consequence of the impact started the shutdown of photosynthesis, leading to a large deforestation further enhancing weathering processes [40]. A decrease in vegetation would have also affected the animals which rely on it, like herbivorous dinosaurs [40].

The negative ∂^7Li shift can only be explained in the context of weathering processes, as ^{7}Li is washed away more easily than ^{6}Li out of the clays. A denudation of the continental surface in combination with acid rain conditions could have resulted in this negative shift.
Our results support the previously described hypothesis of significant changes of the environmental circumstances at the K/Pg boundary [38,40,46].

7.4. Summary of Chapter 7

Memory effects were observed during MC-ICP-MS analyses. A first action to overcome the memory effects was burn-off via the use of dry plasma conditions. Lower blanks were obtained immediately after the dry plasma conditions. During measurements, the blank intensities increased gradually. Further optimization should deal with this memory effect.
The amount of lithium and/or sodium was measured in the pre-, lithium- and post-elution fractions. No lithium-elution fractions contained sodium in concentrations above the 5,000 µg/l threshold value. Both duplicates of K/Pg clay samples indicated a negative in ∂^7Li exactly at the K/Pg boundary. Unfortunately, there is a significant difference between the duplicate results. The negative deviation is a mark of increased continental weathering at the K/Pg boundary. This increased weathering is linked to the extra-terrestrial impact of the same age. A possible hypothesis focuses on the influence of prolonged darkness and acid rain as a possible cause for this negative deviation.

8. Conclusions

8.1. Method development for Lithium isotopic analysis via MC-ICP-MS.

During this work, a method was developed to measure lithium isotope ratios in geological samples via MC-ICP-MS. Various important aspects were studied (1) mass discrimination correction models, (2) adequate choice of the resistance of the amplifiers in view of the lithium concentration in the samples and (3) the influence of sodium on the isotope ratio result obtained.

External correction in a sample-standard bracketing approach gave the most accurate results and best precision and was considered to be the most efficient method to deal with instrumental mass discrimination. As a result, no internal standard, such as boron, was used in further MC-ICP-MS analyses.

The Faraday cups of the MC-ICP-MS were combined with different amplifiers. It was decided to use a 10^{12} Ω amplifier for detection of ^{6}Li, while a 10^{11} Ω amplifier was selected for the ^{7}Li isotope at concentrations of 50 µg/l Li.

Cation exchange chromatography was used to separate lithium from its matrix, but low concentrations of sodium were still present in the lithium-elution fraction of several samples. The sodium tolerance test indicated sufficient resistance against concentrations of sodium up to 5,000 µg/l in samples containing 50 µg/l Li.

8.2. Application to Cretaceous-Paleogene boundary clays from the Umbria-Marche sequence.

During this work, the isotopic composition of lithium present in clay fraction of the samples originating from different localities within the Umbria-Marche sequence, was investigated. The isolation of lithium out of these samples was achieved stepwise. At first, a procedure to separate the clay fraction from the limestone matrix by adding successive batches of diluted HNO_3 was optimized. The ratio of clay to limestone ranged between < 1 % and 88 %. After this separation, the clay fractions were successfully digested in a two-step procedure, making use of an HF/HNO_3 mixture and aqua regia. The isolation of lithium out of the dissolved clays was the most crucial part of this Master thesis. By performing a single-step cation exchange chromatography, lithium could be isolated quantitatively. This separation technique was exceptionally challenging, especially for the low amounts of lithium available. Sufficient knowhow on the isolation technique was not available within the department of Analytical Chemistry of Ghent University at the start of this project. As a result, a ten-day research stay to the University of Cambridge was necessary to learn the technique.

The experimental work involving cation exchange chromatography consisted of three major parts: (1) column calibration, (2) a performance check with seawater and (3) treatment of the actual clay fractions.

The hardest and most crucial part was the column calibration. The column calibration took up 19 hours of non-stop lab work, in order to precondition the columns and to capture a complete elution profile. A separation of at least 1.5 ml between the lithium and sodium elution peaks was achieved. Subsequently, a performance check with Sargasso seawater was carried out to ensure that correct ∂^7Li values were obtained. All columns except for one, passed this test, indicating that the ∂^7Li value obtained matched that reported average reference value in the literature (*i.e.* 31.0 ± 0.5 ‰) within experimental uncertainty. In a final stage, the actual samples were loaded on the columns. Lithium was quantitatively recovered from the clays after the isolation procedure and without significant contamination with sodium.

In the results chapter of this master thesis, a depth profile of clay samples linked to the K/Pg impact event, was documented in view of the ∂^7Li values. A negative shift of ∂^7Li exactly at K/Pg boundary indicated a link between the clays and the impact event. A possible interpretation of this negative shift was described in terms of paleoclimatologic consequences originating from the extra-terrestrial body that hit planet Earth 66 million years ago.

References

[1] P. Claeys and S. Goderis, “Lethal Billiards,” *Nature*, vol. 449, pp. 30–31, 2007.

[2] R. A. Kerr, “A Big Splat in the Asteroid Belt Doomed Earth’s Dinosaurs,” *Science*, vol. 317, p. 1310, 2007.

[3] W. F. Bottke, D. Vokrouhlický, and D. Nesvorný, “An asteroid breakup 160 Myr ago as the probable source of the K/T impactor.,” *Nature*, vol. 449, pp. 48–53, 2007.

[4] V. Reddy, J. A. Sanchez, W. F. Bottke, M. J. Gaffey, L. Le Corre, J. Masiero, and A. K. Mainzer, “Composition of (1696) Nurmela: The second largest member of Baptistina Asteroid Family,” *44th Lunar and Planetary Science Conference*, p. 1093, 2013.

[5] P. R. Renne, A. L. Deino, F. J. Hilgen, K. F. Kuiper, D. F. Mark, W. S. Mitchell, L. E. Morgan, R. Mundil, and J. Smit, “Time scales of critical events around the Cretaceous-Paleogene boundary.,” *Science*, vol. 339, pp. 684–687, 2013.

[6] M. Rehkämper, M. Schönbächler, and R. Andreasen, “Appliciation of Multiple-Collector Inductively Coupled Plasma Mass Spectrometry to Isotopic Analysis in Cosmochemistry,” in *Isotopic analysis Fundamentals and applications using ICP-MS*, F. Vanhaecke and P. Degryse, Eds. 2012, pp. 275–315.

[7] D. Porceli and M. Baskaran, “An overview of Isotope Geochemistry in Environmental Studies,” in *Handbook of environmental isotope geochemistry*, M. Baskaran, Ed. 2011, pp. 11–32.

[8] A. Landais, “Stable Isotopes of N and Ar as tracers to Retrieve Past temperature from Air trapped in Ice Cores.,” in *Handbook of environmental isotope geochemistry*, M. Baskaran, Ed. 2011, pp. 865–886.

[9] P. B. Tomascak, “Developments in the understanding and application of lithium isotopes in the earth and planetary sciences,” *Mineralogy & geochemistry*, vol. 55, pp. 153–195, 2004.

[10] K. W. Burton and N. Vigier, “Lithium Isotopes as Tracers in Marine and Terrestrial Environments,” in *Handbook of environmental isotope geochemistry*, M. Baskaran, Ed. 2011, pp. 41–59.

[11] M. A. Sephton, R. H. James, M. A. Fehr, P. A. Bland, and M. Gounelle, “Lithium isotopes as indicators of meteorite parent body alteration,” *Meteoritics & Planetary Science*, vol. 7, 2013.

[12] S. Misra and P. N. Froelich, “Lithium isotope history of Cenozoic seawater: changes in silicate weathering and reverse weathering.,” *Science*, vol. 335, pp. 818–23, 2012.

[13] L. Chan and J. M. Edmond, “Variation of lithium isotope composition in the marine environment: A preliminary report,” *Geochimica et Cosmochimica Acta*, vol. 7, pp. 909–915, 1988.

[14] H. R. Marschall, P. a. E. Pogge von Strandmann, H.-M. Seitz, T. Elliott, and Y. Niu, “The lithium isotopic composition of orogenic eclogites and deep subducted slabs,” *Earth and Planetary Science Letters*, vol. 262, pp. 563–580, 2007.

[15] R. L. Rudnick, P. B. Tomascak, H. B. Njo, and L. R. Gardner, “Extreme lithium isotopic fractionation during continental weathering revealed in saprolites from South Carolina,” *Chemical Geology*, vol. 212, pp. 45–57, 2004.

[16] C.-F. You and L.-H. Chan, “Precise determination of lithium isotopic composition in low concentration natural samples,” *Geochimica et Cosmochimica Acta*, vol. 60, pp. 909–915, 1996.

[17] M. Wieser, J. Schwieters, and C. Douthitt, “Multi-Collector Inductively Coupled Plasma Mass Spectrometry,” in *Isotopic analysis Fundamentals and applications using ICP-MS*, F. Vanhaecke and P. Degryse, Eds. 2012, pp. 77–91.

[18] F. Vanhaecke, L. Balcaen, and D. Malinovsky, “Use of single-collector and multi-collector ICP-mass spectrometry for isotopic analysis,” *Journal of Analytical Atomic Spectrometry*, vol. 24, pp. 863–886, 2009.

[19] J. Blumberg, “Dartmouth Researchers Say a comet killed the Dinosaurs.” [Online]. Available: http://now.dartmouth.edu/2013/04/dartmouth-researchers-say-a-comet-killed-the-dinosaurs/. [Accessed: 28-May-2013].

[20] R. Thomas, “Part II: the sample introduction system,” in *A beginner’s guide to ICP-MS*, 2001.

[21] A. Montaser, M. G. Minnich, J. A. McLean, L. Huiying, J. A. Caruso, and C. W. McLeod, “Sample introduction in ICPMS,” in *Inductively Coupled Plasma Mass Spectrometry*, A. Montaser, Ed. 1998, pp. 85–224.

[22] R. Thomas, “Part III: The plasma source,” in *A Beginner’s guido to ICP-MS*, 2001.

[23] F. Vanhaecke, “Single-Collector Inductively Coupled Plasma Mass Spectrometry,” in *Isotopic analysis Fundamentals and applications using ICP-MS*, F. Vanhaecke and P. Degryse, Eds. 2012, pp. 31–75.

[24] C. Bouman, *Welcome to the NEPTUNE Multicollector-ICPMS Basic Operator Training*. 2008.

[25] A. Montaser, J. A. McLean, and L. Huiying, “An introduction to ICP spectrometers for elemental analysis,” in *Inductively Coupled Plasma Mass Spectrometry*, 1998, pp. 1–31.

[26] Agilent Technologies, “ICP-MS inductively Coupled Plasma Mass spectrometry A Primer,” 2005. [Online]. Available: http://www.agilenticpms.com/primer/ICP-MS Primer.pdf. [Accessed: 22-May-2013].

[27] H. E. Taylor and J. R. Garbarino, “Analytical applications of inductively coupled plasma mass spectrometry,” in *Inductively Coumpled Plasmas in Analtical Atomic Spectrometry*, A. Montaser and D. W. Golightly, Eds. 1992.

[28] R. Thomas, “PartIV: The interface region,” in *A beginner’s guide to ICP-MS*, 2001.

[29] R. Thomas, “Part V: The Ion Focussing system,” in *A beginner’s guide to ICP-MS*, 2001.

[30] R. Thomas, “Part VII Mass Separation Devices — Double-Focusing Magnetic-Sector Technology,” in *A beginner’s guide to ICP-MS*, 2001.

[31] R. Thomas, “Part VI The Mass Analyzer,” in *A beginner’s guide to ICP-MS*, 2001.

[32] R. Thomas, “Part X Detectors,” in *A beginner’s guide to ICP-MS*, 2001.

[33] Spectro Arcos, “High resolution ICP-CCd Spectrometer for the Most Demanding Elemental Analysis Requirements in Industry, Environmental Protection and Academia,” 2011. [Online]. Available: http://www.potencialzero.com/media/33905/br_arcosen082011.pdf. [Accessed: 23-May-2013].

[34] IUPAC, “analytical compendium.” [Online]. Available: http://iupac.org/publications/analytical_compendium/Cha10sec3219.pdf. [Accessed: 28-May-2013].

[35] National Institute of Standards & Technology, “Standard Reference Material 951 Boric Acid Standard,” 1999.

[36] Institute for Reference Materials and Measurements, “Certificate Isotopic Reference Material IRMM-016,” 2005.

[37] D. C. Gregoire, B. M. Acheson, and R. P. Taylor, “Measurement of lithium isotope ratios by inductively coupled plasma mass spectrometry: Application to geological materials,” *Journal of Analytical Atomic Spectrometry*, vol. 11, pp. 765–772. 1996.

[38] L. W. Alvarez, W. Alvarez, F. Asaro, and V. A. Helen, “Extraterrestrial Cause for the Cretaceous-Tertiary Extinct tion Experimental results and theoretical interpretation,” *Science*, vol. 208, pp. 1095–1108, 1980.

[39] A. Montanari and C. Koeberl, *Impact Stratigraphy The Italian Record*. 2000.

[40] P. Schulte, L. Alegret, I. Arenillas, J. a Arz, P. J. Barton, P. R. Bown, T. J. Bralower, G. L. Christeson, P. Claeys, C. S. Cockell, G. S. Collins, A. Deutsch, T. J. Goldin, K. Goto, J. M. Grajales-Nishimura, R. a F. Grieve, S. P. S. Gulick, K. R. Johnson, W. Kiessling, C. Koeberl, D. a Kring, K. G. MacLeod, T. Matsui, J. Melosh, A. Montanari, J. V Morgan, C. R. Neal, D. J. Nichols, R. D. Norris, E. Pierazzo, G. Ravizza, M. Rebolledo-Vieyra, W. U. Reimold, E. Robin, T. Salge, R. P. Speijer, A. R. Sweet, J. Urrutia-Fucugauchi, V. Vajda, M. T. Whalen, and P. S. Willumsen, “The Chicxulub asteroid impact and mass extinction at the Cretaceous-Paleogene boundary.,” *Science*, vol. 327, pp. 1214–8, Mar. 2010.

[41] A. Montanari and C. Koeberl, “Introduction: Impact Cratering as a Geological process,” in *Impact Stratigraphy The Italian Record*, A. Montanari and C. Koeberl, Eds. 2000, pp. 1–55.

[42] A. R. Hildebrand, G. T. Penfield, D. A. Kring, M. Pilkington, A. C. Z, B. Stein, W. V Boynton, and S. B. Jacobsen, “Geology Chicxulub Crater : A possible Cretaceous / Tertiary boundary impact crater on the Chicxulub Crater : A possible Cretaceous / Tertiary boundary impact crater on the Yucatán Peninsula , Mexico,” *geological society of America*, 1991.

[43] A. Montanari and C. Koeberl, “Important Distal Ejecta Layers and Their Source Craters,” in *Impact Stratigraphy The Italian Record*, 2000, pp. 102–158.

[44] S. Goderis, “Reevalution of siderophile abundances and ratios across the Cretaceous-Paleogene (K-PG) boundary: Implications for the nature of the projectile,” *In press*, 2013.

[45] P. Claeys and W. Kiessling, “Distribution of Chicxulub ejecta at the Cretaceous-Tertiary boundary,” *geological Society of America*, pp. 55–68, 2002.

[46] J. Smit, “Meteorite impact, extinctions and the Cretaceous-Tertiary Boundary*,” *Geologie en Mijnbouw*, vol. 69, pp. 187–204, 1990.

[47] A. Montanari and C. Koeberl, “The Umbria-Marche Sequence,” in *Impact Stratigraphy The Italian Record*, 2000, pp. 158–166.

[48] A. Montanari and C. Koeberl, “Impact Stratigraphy in the U-M sequence,” in *Impact Stratigraphy The Italian Record*, 2000, pp. 166–278.

[49] F. T. Kyte, “A meteorite from the Cretaceous/Tertiary boundary,” *Nature*, vol. 396, pp. 237–239, 1998.

[50] A. Trinquier, J.-L. Birck, and C. Jean Allègre, “The nature of the KT impactor. A 54Cr reappraisal,” *Earth and Planetary Science Letters*, vol. 241, pp. 780–788, 2006.

[51] N. Vigier, A. Decarreau, R. Millot, J. Carignan, S. Petit, and C. France-Lanord, “Quantifying Li isotope fractionation during smectite formation and implications for the Li cycle,” *Geochimica et Cosmochimica Acta*, vol. 72, pp. 780–792, 2008.

[52] R. Millot, N. Vigier, and J. Gaillardet, “Behaviour of lithium and its isotopes during weathering in the Mackenzie Basin, Canada,” *Geochimica et Cosmochimica Acta*, vol. 74, pp. 3897–3912, 2010.

[53] S. Misra and P. N. Froelich, “Measurement of lithium isotope ratios by quadrupole-ICP-MS: application to seawater and natural carbonates,” *Journal of Analytical Atomic Spectrometry*, vol. 24, p. 1524, 2009.

[54] M. Rehkämper, M. Schönbächler, and C. H. Stirling, “Back to Basics Review Multiple Collector ICP-MS : Introduction to Instrumentation , Measurement Techniques and Analytical Capabilities,” *geostandars and geoanalytical research*, vol. 25, pp. 23–40, 2010.

[55] H. Andren, I. Rodushkin, A. Stenberg, D. Malinovsky, and D. C. Baxter, “Sources of mass bias and isotope ratio variation in multi-collector ICP-MS: optimization of instrumental parameters based on experimental observations,” *Journal of Analytical Atomic Spectrometry*, vol. 19, pp. 1217–1224, 2004.

[56] J. Meija, L. Y. Z. Mester, and S. R. E., “5 Correction of Instrumental Mass Discrimination for isotope Ratio Determination with Multi-Collector Inductively Coupled Plasma Mass Spectrometry,” in *Isotopic analysis Fundamentals and applications using ICP-MS*, F. Vanhaecke and P. Degryse, Eds. 2012, pp. 113–137.

[57] D. C. Baxter, I. Rodushkin, and E. Engström, “Isotope abundance ratio measurements by inductively coupled plasma-sector field mass spectrometry,” *Journal of Analytical Atomic Spectrometry*, vol. 27, p. 1355, 2012.

[58] A. S. Al-ammar and R. M. Barnes, “improving isotope ratio precision in inductively coupled plasma quadrupoel mass specrometry by common analyte internal standardization,” *Journal of Analytical Atomic Spectrometry*, vol. 16, pp. 327–332, 2001.

[59] S. D. Tanner, “Space charge in ICP-MS : calculation and implications,” *Spectrochimica Acta Part B-Atomic Spectroscopy*, vol. 47B, pp. 809–823, 1992.

[60] X. F. Sun, B. T. G. Ting, S. H. Zeisel, and M. Jonghorbani, “Accurate measurements of stable isotopes of lithium by inductively coupled plasma mass spectrometry,” *Analyst*, vol. 112, pp. 1223–1228, 1987.

[61] F. Vanhaecke and P. Degryse, *Isotopic analysis Fundamentals and Applications Using ICP-MS*. 2012, pp. 1–529.

[62] F. Vanhaecke, “Massaspectrometrie en isotopenanalyse,” *Cursus, Ugent*, 2012.

[63] T. Hirata, “4. Advances in Laser Ablation-Multi-collector inductively coupled Plasma Mass Spectrometry,” in *Isotopic analysis Fundamentals and applications using ICP-MS*, F. Vanhaecke and P. Degryse, Eds. 2012, pp. 93–112.

[64] N. S. Llyod, J. Schwieters, M. S. A. Horstwood, and R. R. Parrish, “28 particle detectors used in isotope ratio mass spectrometry with applications in geology, environmental science and nuclear forensics,” in *Handbook of particle detection and imaging*, 2012, pp. 685–701.

[65] P. B. Tomascak, R. W. Carlson, and S. B. Shirey, “Accurate and precise determination of Li isotopic compositions by multi-collector sector ICP-MS,” *Chemical Geology*, vol. 158, no. 1–2, pp. 145–154, 1999.

[66] T. Moriguti and E. Nakamura, “High-yield l . ithium separation and the precise isotopic analysis for natural rock and aqueous samples,” *Chemical Geology*, vol. 145, pp. 91–104, 1998.

[67] R. H. James and M. R. Palmer, “The lithium isotope composition of international rock standards,” *Chemical Geology*, vol. 166, no. 3–4, pp. 319–326, 2000.

[68] F. W. E. Strelow, C. J. Liebenberg, and a. H. Victor, “Accurate determination of ten major and minor elements in silicate rocks based on separation by cation exchange chromatography on a single column,” *Analytical Chemistry*, vol. 46, pp. 1409–1414, 1974.

[69] C. a Pohl, J. R. Stillian, and P. E. Jackson, “Factors controlling ion-exchange selectivity in suppressed ion chromatography,” *Journal of Chromatography A*, vol. 789, pp. 29–41, 1997.

[70] F. W. E. Strelow, “An Ion Exchange Selectivity Scale of Cations Based on Equilibrium Distribution Coefficients,” *Analytical Chemistry*, vol. 32, pp. 1185–1188, 1960.

[71] R. A. Bartsch, B. P. Czech, S. I. Kang, L. E. Stewart, W. Walkowiak, W. A. Charewicz, G. S. Heo, and B. Son, “High Lithium Selectivity in Competitive Alkali-Metal Solvent Extraction by Liphilic Crown Carboxylic-Acids,” *journal of the american chemical society*, vol. 107, pp. 4997–4998, 1985.

[72] M. Abe and R. Chitrakar, “Synthetic Inorganic Ion-Exchange Materials . XLV . Recovery of Lithium from Seawater and Hydrothermal Water by Titanium (IV) Antimonate Cation Exchanger Preparation of TiSbA,” vol. 19, pp. 117–128, 1987.

[73] A. Mitsuo, E. Asijati, A. Ichsan, and K. Hayashi, “Ion-Exchange Separation of Lithium from Large Amounts of Sodium , Calcium , and Other Elements by a Double Column of Dowex 50W-X8 and Crystalline Antimonic (V) Acid,” pp. 524–527, 1980.

[74] T. I. Taylor and H. C. Urey, “Fractionation of the Lithium and Potassium Isotopes by Chemical Exchnge with Zeolites,” *Journal of chemical physics*, vol. 6, pp. 429–438, 1938.

[75] E. R. Tompkins and S. W. Mayer, “Ion Exchange as a Separations Method.,” *journal of the american chemical society*, p. 2859, 1947.

[76] F. W. E. Strelow, “Distribution coefficients and ion exchange behavior of 46 elements with a macroreticular cation exchange resin in hydrochloric acid,” *Analytical Chemistry*, vol. 56, pp. 1053–1056, 1984.

[77] BIO RAD, “Analytical Grade Resin Selection Guide,” 2013. [Online]. Available: http://www.bio-rad.com/prd/en/US/PSD/PDP/0c308553-8af9-4991-9f81-660f2298b385/AG-50W-and-AG-MP-50-Cation-Exchange-Resins. [Accessed: 23-Apr-2013].

[78] BIO RAD, “AG® 50W and AG MP-50 caton exchange resins instruction manual,” 2013.

[79] F. W. E. Strelow, R. Ruthild, and C. J. C. Bothma, “Ion Exchange Selectivity Scales for Cations in Nitric Acid and Sulfuric Acid Media with a Sulfonated Polystyrene Resin,” *Analytical Chemistry*, vol. 37, pp. 106–110, 1965.

[80] W. Rieman and H. F. Walton, “Ion exchange in analytical chemistry,” *Analytical Chemistry*, p. 295, 1970.

[81] F. W. E. Strelow, J. H. J. Coetzee, and C. R. Van Zyl, “Separation of Alkali Metals from Alkaline Earths and Other Elements by Cation Exchange Chromatography in Nitric Acid,” *Analytical chemistry*, vol. 40, pp. 196–199, 1968.

[82] F. W. Strelow and H. Sondorp, “Distribution Coefficients and Cation-Exchange Selectives of Elements with AG50W-X8 Resins in Perchloric Acid.,” *Talanta*, vol. 19, pp. 1113–20, 1972.

[83] F. W. E. Strelow, C. H. S. W. Weinert, and T. N. Van Der Walt, “Separation of Lithium from Sodium, Berylium and Other Elements by Cation-exchange Chromatography in Nitric Acid-Methanol,” *analytica Chimica Acta*, vol. 71, pp. 123–132, 1974.

[84] F. W. E. Strelow, A. H. Victor, C. R. Z. Van, and C. Eloff, “Distribution Coefficients and Cation Exchange Behavior of Elements in Hydrochloric Acid-Acetone,” *analytica Chimica Acta*, vol. 43, pp. 389–395, 1971.

[85] A. B. Jeffcoate, T. Elliott, A. Thomas, and C. Bouman, “Precise, small sample size determinations of lithium isotopic compositions of geological reference materials and modern seawater by MC-ICP-MS,” *GEOSTANDARDS AND GEOANALYTICAL RESEARCH*, vol. 28, pp. 161–172, 2004.

[86] P. Gates, “Gas Chromatography Mass Spectrometry (GC/MS),” 2013. [Online]. Available: http://www.bris.ac.uk/nerclsmsf/techniques/gcms.html. [Accessed: 02-Jun-2013].

[87] C. R. Scotese, “The end of the Dinosarus,” 2013. [Online]. Available: http://www.scotese.com/K/t.htm. [Accessed: 29-May-2013].

[88] R. Thomas, *Practical Guide to ICP-MS*. 2004.

Isotopische analyse van Li in kleistalen van de Krijt-Paleogeen grens afkomstig uit Umbria-Marche (Italië): indicatie van extreme verweringsverschijnselen na de meteorietimpact?

T. Croymans[a], K. Van Hoecke[a], S. Misra[b], P. Claeys[c] and F. Vanhaecke[a]

[a] *Vakgroep Analytische Chemie, Universiteit Gent, België*
[b] *Department of Earth Sciences, University of Cambridge, Verenigd Koninkrijk*
[c] *Departement Geologie, Vrije Universiteit Brussel, België*

Lithiumisotopen vervullen, omwille van hun uitgesproken fractionatie, een belangrijke rol in geochemisch en cosmochemisch onderzoek. In dit werk werd een methode ontwikkeld om de isotopische samenstelling van Li in laaggeconcentreerde oplossingen van ~50 µg/l te bepalen via multi-collector ICP-massaspectrometrie (MC-ICP-MS) en vervolgens toegepast op de analyse van kleistalen, afkomstig uit de Umbria-Marche regio (Italië), verbonden met de Krijt Paleogeen (K/Pg) impact. De kleistalen werden eerst afgescheiden uit hun kalksteenmatrix met behulp van 0,14 M HNO_3. De kleien werden vervolgens door zure digestie in oplossing gebarcht. Li werd vervolgens uit de opgeloste kleimatrix geïsoleerd met behulp van kationenuitwisselingschromatografie met BioRad AG 50W-X8 (100-200 mesh size) resin. Kwantitatieve recovery van Li en een complete scheiding van Li en Na werden bekomen. De invloed van verschillende concentraties aan Na op de ∂^7Li waarde, gemeten met MC-ICP-MS in een 50 µg/l Li-oplossing, resulteerde pas in een negatieve shift in de ∂^7Li waarde wanneer de toegevoegde Na-concentratie meer dan 5000 µg/l bedroeg. De ∂^7Li waarden werden bepaald voor kleien afkomstig van een interval van 5 m boven en onder de K/Pg grens. Een negatieve shift van ~2 ‰ werd gevonden in kleistalen afkomstig van de K/Pg grens zelf (-4,6 ± 0,5 ‰ en -3,1 ± 0,5 ‰), ten opzichte van de kleifracties onder (Krijt, tussen -1.3 en -2.3 ± 0,5 ‰) en boven (Paleogeen, tussen -0,9 en -3,5 ‰ ± 0,5 ‰) de K/Pg grens. Deze negatieve shift zou het gevolg kunnen zijn van intensievere verwering als gevolg van de meteorietimpact die 66 miljoen jaar geleden plaatsvond op het Yucatán schiereiland (Mexico). De negatieve shift is een bevestiging van eerdere geologische hypotheses die gewag maken van ontbossingen en zure regen na de meteorietimpact.

1.Introductie

1a. Lithium als indicator voor verweringsverschijnselen.

Lithium heeft twee stabiele isotopen: ^{6}Li (natuurlijke abundantie ~7,5 %) & ^{7}Li (natuurlijke abundantie ~92,5 %). Het relatieve massaverschil tussen deze twee isotopen is ongeveer 16 %. De li isotopenverhouding wordt uitgedrukt als ∂^7Li (‰), cfr. vgl.1. IRMM-016 is Li_2CO_3 isotopisch referentiemateriaal.

$$\partial^7 Li\ (‰) = \left\{\left[\frac{\left(\frac{^7Li}{^6Li}\right)_{staal}}{\left(\frac{^7Li}{^6Li}\right)_{IRMM-016}}\right] - 1\right\} x\ 1000 \qquad (1)$$

Lithium is gekend als een indicator voor verweringsprocessen van verschillende steensoorten [1–5]. Deze processen worden meestal vergezeld van fractionatie tussen de twee isotopen [1–5]. Tijdens het verweringsproces wordt ^{6}Li beter weerhouden in het sediment, terwijl ^{7}Li makkelijker wordt uitgespoeld [4]. Dit verweringsmechanisme is reeds aangetoond op basis van het vergelijken van ∂^7Li waarden in moedergesteenten en hun naburige rivieren, waarbij de rivieren altijd een positievere ∂^7Li waarde vertonen dan het moedergesteente [2]. Misra en Froelich (2012) [6] toonden een stijging in ∂^7Li van +9 ‰ aan in zeewater doorheen de tijd, van het paleogeen tot het heden, wat eveneens wijst op een uitspoeling van ^{7}Li van het continent naar de oceaan.

1b. Geologische achtergrond over het K/Pg impact event.

De Krijt/paleogeen (K/Pg) grens is gelinkt aan de vijfde en meest recente massa-extinctie die plaatsvond op onze planeet [7]. Gedurende lange tijd werd gedacht dat verhoogde vulkanische activiteit aan de oorsprong van deze massa-extinctie, die onder andere het einde van dinosaurussen betekende, lag [8,9]. In 1980 kwamen Alvarez et al. [7] met een hypothese over een extra-terrestrische impact. Zij ontdekten een verhoogde aanwezigheid van Ir en andere platinagroep elementen (PGE) in de kleilaag die 66 miljoen jaar geleden werd afgezet. In 1991 vonden Hildebrandt et al. [10] een impactstructuur die van overeenstemmende ouderdom was als de massa-extinctie. Deze impactstructuur is gelegen op het Yucatán schiereiland (Mexico) [10]. Tegenwoordig gelooft het grootste deel van de wetenschappelijke gemeenschap dat daar een extra-terrestrische impact heeft plaatsgevonden [8]. De koolstofhoudende chondrietmeteoriet, het Chixculub projectiel genoemd, is verondersteld het resultaat te zijn van een asteroïdenbotsing in de asteroïdengordel tussen Mars en Jupiter [11–14]. Deze botsing zou 160 miljoen jaar geleden hebben plaatsgevonden [11,13,14].
Naast de iridium anomalie, zijn ook andere bewijzen aangetroffen op aarde die een impact event ondersteunen: mineralen die schokmetamorfe eigenschappen vertonen, impact glas, impact-afgeleide diamanten en spinel rijk in Ni [8,12,15,16]. De klimatologische gevolgen van de impact zijn tot op heden nog niet volledig ontrafeld. De meteoriet van 10 km doorsnede gaf onder meer aanleiding tot zure regen, globale temperatuursverandering en langdurige duisternis [6–8,16]. Deze langdurige duisternis gaf aanleiding tot verminderde fotosynthese, waardoor grote delen van de op Aarde aanwezige planten en bossen zouden verdwenen zijn, en bijgevolg ook de dieren van wie zij de voedingsbron waren [8]. De wereldwijde kleidepositie op de K/Pg grens is ook verondersteld het gevolg te zijn van deze extra-terrestrische impact [12].

1c. Kolomchromatografie als isolatietechniek

Kationenuitwisselingschromatografie is een veel gebruikte techniek om Li uit geologische stalen af te scheiden [4,5,17]. Deze techniek blijkt enkel representatieve waardes voor de isotopische samenstelling van Li te kunnen bieden als kwantitatieve recovery (100 %) wordt bereikt [18]. Bij de kolomchromatografische scheiding treedt

er isotopenfractionatie op, waardoor ^{6}Li tijdsgemiddeld iets later van de kolom elueert dan ^{7}Li [18,19].

2.Experimenteel

2a. Reagentia voor monstervoorbereiding

Enkelvoudig in-house gedestilleerd HCl werd bereid van pro-analyse graad HCl met behulp van een kwarts sub-boiling destillatiesysteem. Enkelvoudig in-house gedestilleerd HNO_3 werd bereid van pro-analyse graad HNO_3 met behulp van een Teflon sub-boiling destillatiesysteem (Cupola still van *PicoTrace*®).
Trace metal graad HF werd aangekocht van *Fischer*®. Alle verdunningen werden gemaakt met 18,2 MΩ.cm Millli-Q water.

2 b. Reagentia voor kolomchromatografie

De gehele procedure van kolomchromatografie heeft plaatsgevonden aan de Universiteit van Cambridge (VK). Dubbelvoudig gedestilleerd HCl werd bereid van pro analyse graad HCl *(Fischer)* met behulp van een Cupola sub-boiling installatie van PicoTrace®. Alle verdunningen werden gemaakt met 18,2 MΩ.cm Millli-Q water.

2c. Sargasso zeewater voorbereiding

De stockoplossing zeewater bevatte 175 µg/l Li, wat overeenkomt met de normale concentratie in oceaanwater. Deze oplossing werd met een factor 3,5 opgeconcentreerd via evaporatie met behulp van een verwarmingselement. Deze concentratiestap was nodig om een klein volume (~60 µl) met een voldoende massa aan Li (~35 ng) op de kolom te kunnen laden. De gemiddelde $\partial^{7}Li$ waarde van zeewater is 31,0 ± 0,5 ‰ [18].

2d. IRMM-016 standaard voorbereiding

IRMM-016 standaard *(Geel, België)* werd gebruikt als isotopische standaard ($^{7}Li/^{6}Li$ = 12,177 ± 0,013). Li_2CO_3 werd opgelost in 0,14 M HNO_3; concentratiebepaling werd uitgevoerd met behulp van quadrupool ICP-MS (Q-ICP-MS).

2e. Invloed van versterkerweerstand.

IRMM-016 was gebruikt voor de bereiding van 0,5; 5, 50 en 200 µg/l Li standaardoplossingen in 0,28 M HNO_3. Standaard deviatie (s) was bepaald op de resultaten van de stalen na bracketing.

2f. Kleistalen

Kleistalen van dezelfde locatie en site als deze beschreven in Goderis (2013) [12] werden gebruikt. Goderis (2013) [12] heeft hierin een verhoogde concentratie van Ir en andere PGE elementen aangetoond. Deze verhoging wordt wereldwijd teruggevonden en wordt gelinkt met het K/Pg impact event [7,20].

Stalen werden genomen van de Furlo Pietralata site in de Umbria-Marche regio in Italië. Binnen een diepte-inteval van 10 m werd om de meter een staal genomen.

Tien cm boven en onder de K/Pg grens werd eveneens een staal genomen. Als referentiepunt in het diepteprofiel werd de K/Pg grens genomen. Deze wordt doorheen de rest van het artikel gelijk gezet aan diepte 0. Stalen boven de kleilaag zijn afkomstig van het Paleogeen, stalen onder de klei laag zijn afkomstig van het Krijt.
Vervolgens werd een deel van het staal afgezaagd met een diamantzaag. De afgezaagde delen werden gehomogeniseerd in een agaat mortier. Tussen elke twee stalen werd de mortier gereinigd. Er werd 200 mg afgewogen van de stalen afkomstig van het Krijt en het Paleogeen, van het K/Pg staal werd 40 mg afgewogen.
Klei werd van de matrix geïsoleerd met behulp van verschillende addities van 2 ml 0,14 M HNO_3. Na elke additie werd het staal samen met het zuur gevortexed en gedurende 15 tot 20 min in een ultrasoonbad *(5510 Branson®)* geplaatst, vervolgens 10 min gecentrifugeerd met een vaste hoek centrifuge *(Heraeus Sepatech Labofuge 200)* aan 5300 rpm. Het gebruikte zuur werd voor een nieuwe additie verwijderd met behulp van een Pasteur pipet en de procedure werd herhaald. De stalen werden met zuur behandeld tot de kalksteenmatrix volledig verdwenen was. Vervolgens werd de kleirest gedurende 24 uur gedroogd in een oven bij 105 °C. Deze stappen werden uitgevoerd in 15 ml centrifugebuisjes (*VWR international®).* De gedroogde klei werd gewogen en overgebracht in 15 ml Savillex® Teflon® bekers. Bovenstaande stappen werden uitgevoerd in normale labo omstandigheden.
De pure kleifracties werden ontsloten in twee stappen. In een eerste fase werd 3 ml HF:HNO_3 (2:1) mengsel toegevoegd. Deze oplossing werd gedurende 24 uur verwarmd bij 110 °C op een verwarmingsplaat. Vervolgens werd het mengsel tot kamertemperatuur afgekoeld en uitgedampt op 80 °C. In een tweede fase werd 3 ml koningswater toegevoegd aan de uitgedampte fractie. Deze oplossing werd gedurende 24 uur verwarmd bij 95 °C op een verwarmingsplaat, vervolgens tot kamertemperatuur afgekoeld en uitgedampt op 80 °C. De uitgedampte fractie werd ten slotte opgelost in 750 µl 0,24 M HCl en overgebracht naar zuur-gereinigde Eppendorf buisjes. De digestieprocedure werd uitgevoerd onder klasse 10 clean lab condities.

2g. kolomchromatografie

2g.1. Chromatografische kolommen. In eerste instantie werden negen Teflon® kolommen met een Teflon® frit en een volume van 6 ml voorbereid. De kolommen zijn 250 mm hoog en hebben een interne diameter van 3,2 mm. Uiteindelijk werden acht kolommen gebruikt om lithium te scheiden uit de kleimatrix.
In een eerste stap werden de kolommen gespoeld met methanol en vervolgens met Milli-Q water. Vervolgens werden de kolommen gepakt met 2 ml BioRad® AG 50W-X8 hars (100-200 mesh size), gesuspendeerd in Milli-Q water. Het hars heeft een uitwisselingscapaciteit van 1.7 meq/ml.
Voor het laden van de gepakte kolommen werden deze telkens voorgespoeld met 6 M HCl, vervolgens nagespoeld met 0,5 M HCl en geconditioneerd met 6 ml 0.5 M HCl. Deze procedure werd herhaald tussen de behandeling van twee stalen. Na opbrengen van het staal in een maximaal volume van 200 µl, werd elk staal geëlueerd met 15 ml 0,5 M HCl. Er werden 3 fracties opgevangen: (1) de pre-elutie fractie (0-5 ml), (2) de Li-fractie (5-10 ml) en (3) de post-elutie fractie (10-15ml). Het elutievolume van deze fracties werd bepaald via een kolomkalibratie (zie verder). In alle fracties werden het lithiumgehalte bepaald. De pre- en Li-fractie werden tevens ook gecontroleerd op de aanwezigheid van Na.

2g.2. kolomkalibratie In eerste instantie werd elke kolom gekalibreerd met 50 µl en 125 µl van een oplossing van de verschillende gedigesteerde kleifracties. Elke kolom werd geëuleerd met 19 ml 0,5 M HCl, opgevangen in individuele fracties van 0,5 of 1 ml. De kalibratie heeft als doel om te bepalen welk elutievolume Li bevat en om de gewenste scheiding tussen Li en Na te verifiëren.

2.g.3. Performantiecheck met zeewaterstalen: In een volgende stap werd voor elke kolom een performantietest uitgevoerd met 60 µl gepreconcentreerd Sargasso zeewater. Pre-, Li- en post-elutie fracties werden telkens opgevangen. De performantietest was nodig om te bepalen of een correcte ∂^7Li waarde voor het zeewater kon bekomen worden. De performantiecheck werd een tweede keer uitgevoerd voor kolom 5, 6 en 7.

2.g.4. kleistalen van Furlo Pietralata: Uiteindelijk werden de oplossingen (in 0,28 M HCl) van de eigenlijke kleistalen op de kolom geladen. Hierbij werd een hoeveelheid van 50 ng lithium per staal beoogd. De Li-concentratie in elk kleistaal was verschillend, daardoor werden verschillende volumes op de kolom geladen, variërend van 22 µl tot 108 µl. Om de kolomselectiviteit te garanderen mag maximaal 10 % van het uitwisselingsvermogen, uitgedrukt in milli- equivalenten, van de kolom gebruikt worden [21]. De opgebrachte matrix was altijd kleiner dan 1 % van de uitwisselingscapaciteit. Hiervoor werden volgende elementen in rekening gebracht: Li, Na, Mg, Al, P, K, Ca, Sc, Ti, Cr, Mn, Fe, Co, Ni, Cu, Sr en Y.
Van alle afgescheiden klei fracties, behalve degene op -4 m, -2 m, +3 m en +4 m t.o.v. de K/Pg grens, werd ook uit een tweede sub-staal Li geïsoleerd. Standaard deviatie (s) werd bepaald op de resultaten van de bracketing standaarden per meetdag (typisch n= 26).

Alle fracties werden telkens opgevangen in 7 of 15 ml Savillex® Teflon® bekers en uitgedampt bij 80 °C op een verwarmingsplaat. De lithiumfractie werd heropgelost in 1 ml 0.28 M HNO_3, terwijl de pre- en post-elutiefractie werd heropgelost in een totaal volume van 1.5 ml. De gehele kolomchromatografische procedure werd uitgevoerd onder klasse 100 clean-lab condities. Het heroplossen van de gedroogde fracties gebeurde onder klasse 10 clean-lab condities.

2h. Invloed van natriumconcentratie op lithium isotopenverhouding.

In het paragraaf 2 e. werd reeds vermeld dat de scheiding tussen Li en Na cruciaal is. Indien de scheiding niet perfect is, of indien contaminatie optreedt, kan er Na aanwezig zijn in de Li- fractie. Om de invloed van het eventueel aanwezige Na op de Li isotopenverhouding te bestuderen, werden verschillende concentraties (tussen 5 µg/l en 20000 µg/l) aan Na toegevoegd aan 50 µg/l Li oplossingen (IRMM-016) ,. Hiertoe werd een Na 1 g/l van *Inorganic Ventures (Nieuwegein, Nederland)* gebruikt. Standaard deviatie (s) werd bepaald op de resultaten bracketing-standaarden gedurende het experiment (n=25).

2i. Massaspectrometrie

2i.1. MC-ICP-MS

2i.1.1. Instrumenteel: De Li isotopenverhouding in alle stalen werd bepaald met behulp van een Neptune, MC-ICP-MS instrument *(Thermo® scientific, Bremen,*

Duitsland) De ^{7}Li nuclide werd gemeten met de Faraday cup op de H4 positie in combinatie met een 10^{11} Ω versterker en de ^{6}Li nuclide op de L4 Faraday cup in combinatie met een 10^{12} Ω versterker. Een imaginaire massa van 6,526 werd in de centrale cup geplaatst. Er werd gewerkt onder hot plasma (~1290 W) condities. De opnamesnelheid was 100 µl/min. Een kwarts micro-concentrische verstuiver samen met een dubbele kwarts verstuiverkamer, samengesteld uit een cyclonische en een Scott type en verstuiverkamer werd gebruikt voor monsterintrodctie. De kwarts toorts was uitgerust met een platina guard electrode. Zowel sampler als skimmer cone waren van Ni. Een opnametijd van 120 s voor de standaarden en de stalen en 90 s voor de blanco' s werd ingesteld. Na elk staal werd een spoeltijd van 30 s ingelast. Eén meting bestond uit 15 afzonderlijke metingen met een integratietijd van 4,194 s, gescheiden door een overgangstijd van 3,0 s.

2i.1.2. Dagelijkse optimalisatie: Verschillende parameters werden op dagelijkse basis geoptimaliseerd, o.m. centrum van de piek, positie van de toorts, verstuivergasdebiet en plasmagasdebiet. De ^{7}Li signaalintensiteit varieerde in de praktijk tussen 1,2 en 1,4 V voor een 50 µg/l Li oplossing.

2i.1.3. correctie voor massadiscrimatie: Voor correctie voor massadiscrimnatie werd externe correctie, gebaseerd op een standaard-staal-standaard bracketing methode, toegepast. Deze gaf betere waarden dan interne correctiemethodes, gebaseerd op de exponentiële wet, de Russell wet, de methode van Baxter-Woodhead en common analyte internal standardization (CAIS) methode.

Om de invloed van verschillen in analietconcentratie op de massadiscriminatie te vermijden, werd er over gewaakt dat alle stalen en de standaard steeds dezelfde Li-concentratie vertoonden. De gemiddelde ^{6}Li en ^{7}Li intensiteiten in de blanco-oplossingen gemeten voor en na elk staal of standaard, werden afgetrokken van de bekomen ^{6}Li en ^{7}Li signaalintensiteiten voor de stalen en standaarden. De onzekerheid (2s) werd bepaald via de bracketing standaarden geanalyseerd gedurende de volledige meetdag (typisch n = 26).

2i.2. Q-ICP-MS

2i.2.1. Instrumenteel: Li en/of Na concentraties werden bepaald in de pre-, Li- en post-elutie fracties via een X Series 2 Q-ICP-MS instrument, *(Thermo® scientific, Bremen, Duitsland)*. Voor monsterintroductie werd gebruik gemaakt van de combinatie van een kwarts concentrische verstuiver in combinatie met een impact bead verstuiverkamer. De kwarts toorts was uitgerust met een platina guard electrode. De opnamesnelheid was 500 µl/min en gereguleerd via een peristaltische pomp. Zowel sampler als skimmer cone waren van Ni. Het toestel werd geoptimaliseerd zodat aan de vereiste specificaties i.v.m. het voorkomen van dubbel geladen ionen (< 3 %) en oxide-ionen (< 3%) van de fabrikant werd voldaan.

2i.3.SC-ICP-MS

2i.3.1. Instrumenteel: voor kalibratie van elke chromatografische kolom werden de metingen uitgevoerd met een single-collector (SC) element XR sector veld ICP-MS instrument, *(Thermo® scientific, Bremen, Duitsland)* aan het departement van Aardwetenschappen, Universiteit van Cambridge. Metingen zijn uitgevoerd onder klasse 100 clean lab condities. Voor monsterintroductie werd gebruik gemaakt van

een micro-concentrische verstuiver en een Scotttype verstuiverskamer. De monsteropnamesnelheid was 50 µl/min. Bij de metingen werd een 1250 W hot plasma aangewend.

3. **Resultaten en Bespreking**

3 a. Invloed van de versterkerweerstand op de Li- isotopenverhouding gemeten met MC-ICP-MS

Tabel 1. Resultaten van de versterker test, onzekerheid is twee keer de standaarddeviatie (s).

Concentration	**^{7}Li amplifier**	**^{6}Li amplifier**	**∂7Li**	**Uncertainty**
IRMM -016			0.0	1.1
0,5 µg/l	10^{12} Ω amplifier	10^{12} Ω amplifier	-7.5	15.8
5 µg/l	10^{11} Ω amplifier	10^{11} Ω amplifier	0.2	3.9
5 µg/l	10^{12} Ω amplifier	10^{12} Ω amplifier	-0.1	1.7
50 µg/l	10^{11} Ω amplifier	10^{11} Ω amplifier	-0.2	0.3
50 µg/l	10^{12} Ω amplifier	10^{11} Ω amplifier	0.1	0.2
50 µg/l	10^{12} Ω amplifier	10^{12} Ω amplifier	-0.1	0.1
200 µg/l	10^{11} Ω amplifier	10^{11} Ω amplifier	0.0	0.2

Precisies van 0,1 en 0,2 ‰ werden bereikt voor de 50 µg/l oplossingen in combinatie met 10^{12} Ω versterkers voor zowel ^{6}Li als ^{7}Li, en voor ^{6}Li gemeten op een 10^{12} Ω versterker in combinatie met ^{7}Li meting via een 10^{11} Ω versterker. Een resultaat van 0,2 ‰ werd bekomen voor de 200 µg/l lithiumoplossing in combinatie met 10^{11} Ω versterkers. Vanwege de beperkte hoeveelheid lithium aanwezig in de kleistalen, werd geopteerd om 50 µg/l als standaard meetconcentratie te gebruiken. Er werd beslist om een 10^{12} Ω versterker te gebruiken voor ^{6}Li metingen en een 10^{11} Ω versterker voor de ^{7}Li metingen.

3 b. invloed van Na op de Li isotopenverhouding gemeten met MC-ICP-MS

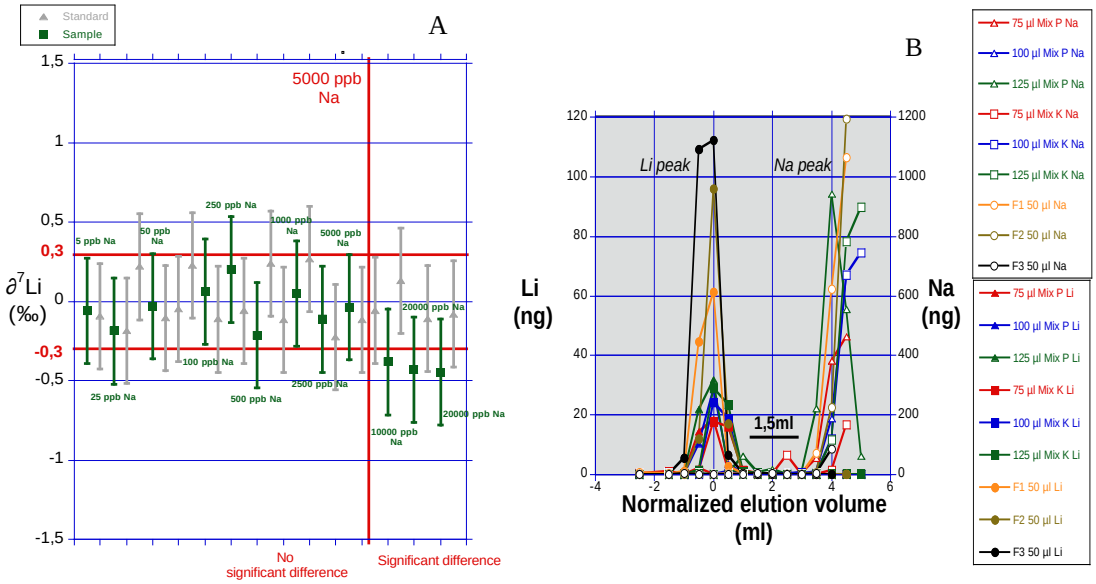

Figuur 1 (A) Na-tolerantie test: Grijze driehoeken geven resultaten voor 50 µg/l IRMM-016 standaarden weer. Groene gevulde vierkanten geven resultaten weer voor 50 µg/L IRMM-016 waaraan verschillende concentraties aan Na – zoals aangeduid in de figuur – werden toegevoegd. Figuur 1 (B) Genormaliseerd elutieprofiel van de negen kolomkalibraties.

Geen significante verschillen konden worden vastgesteld tussen de ∂^7Li waarde voor de "zuivere" standaard enerzijds en de met Na aangerijkte standaarden, anderzijds, tot en met een Na concentratie van 5000 µg/l. Vanaf een concentratie van 10000 µg/l Na was er wel degelijk een invloed te zien. Bij deze hogere concentraties aan Na, worden lagere ∂^7Li waarden verkregen. De foutenvlaggen van de standaarden en de Na-houdende standaarden vertonen wel nog overlap. Dezelfde trend inzake de Li isotopenverhoudingen onder invloed van Na werd ook vastgesteld door Gregoire et al. (1996) [22].

3c. Chromatografische scheiding van lithium

Het elutieprofiel van de negen gekalibreerde kolommen is weergegeven in figuur 1 (B). Het elutievolume werd genormaliseerd, waardoor het volume met maximum piekhoogte voor Li altijd op "0" staat voor elke individuele kolom. Voor de negen kolommen werd een scheiding van minstens 1,5 ml gevonden tussen de Li piek en de Na piek. Het isoleren van lithium uit de kleimatrix is aldus geslaagd. Op basis van de kalibraties werden de volumes van de verschillende elutiefracties bepaald, cf. §2.g.1. Op basis van de kalibratie werd besloten om één van de kolommen (kolom 3) niet verder te gebruiken, aangezien voor deze kolom de Na piek eerder elueerde t.o.v. de andere kolommen. Daarnaast was de elutiesnelheid van deze kolom ook lager in vergelijking met de rest.
Kleine natriumpieken vóór de bulk natriumpiek werden vastgesteld voor kolom 3 en kolom 4. Deze zijn waarschijnlijk te wijten aan het feit dat er voor het allereerste gebruik van de kolommen, *i.e.* de kolomkalibratie, het hars slechts 1 keer met 1 kolomvolume (6 ml) 6 M HCl werd gespoeld.

3d. ∂^7Li waardes voor Sargasso zeewater

Zeewater kan worden beschouwd als worst case scenario voor de kleistalen aangezien in zeewater NaCl (± 35 g/l) in zeer hoge concentratie aanwezig is.

In de literatuur varieert de ∂^7Li waarde voor zeewater van 29,0 ± 0,6 ‰ tot 31,8 ± 1,8 ‰, zoals aangeduid op figuur 2 (B) met het blauwe interval. De verschillende gehanteerde scheidingsmethoden die door verschillende onderzoekers werden gehanteerd verklaren waarschijnlijk deze spreiding [18]. In het algemeen wordt een gemiddelde waarde van 31,0 ± 0,5 ‰ genomen, eveneens aangeduid op figuur 2 (B) met het grijze interval [18]. De binnen dit werk verkregen ∂^7Li waarden voor de Sargasso zeewaterstalen waren gepositioneerd binnen de spreiding van ∂^7Li waarden gevonden binnen de literatuur. Eén waarde, 29,6 ± 0,5 ‰, was lager dan deze van andere kolommen. Meest waarschijnlijke oorzaken hiervoor zouden enerzijds een verlies aan Li en anderzijds contaminatie met Na kunnen zijn.

In de post-elutie fractie, was de Li concentratie altijd beneneden de kwantificatielimiet, *i.e.* 0.2 µg/l, behalve voor kolom 5 (C5). Er werd daar 0,31 ng Li teruggevonden, oftewel ongeveer 0,9 % van de totale hoeveelheid opgebracht lithium.

Echter, lithium dat als laatste van de kolom elueert, is altijd aangerijkt in ^{6}Li [18], [19]. Er zou dus een hoger ∂^{7}Li signaal verwacht worden voor kolom C5, maar in tegenstelling tot deze verwachting werd een lagere waarde gevonden.

In de pre-elutie fracties, werden Na concentraties van 5,1 ; 10,0 ; 71,2 en 16,0 µg/l teruggevonden voor respectievelijk C1, C2, C5 en C6.

Deze lage concentraties in de pre-elutiefracties zouden een voorbode van een het "doorbreken" van Na kunnen geweest zijn. Indien dergelijke doorbraak heeft plaatsgevonden, verwacht men een Na concentratie van hoger dan 5 mg/l in de Li-elutie fractie, wat tot een lagere ∂^{7}Li waarde zou leiden. Helaas werden geen Na concentratiebepalingen uitgevoerd in de lithium-elutie fracties van de zeewaterstalen.

3e. ∂^{7}Li waardes voor de kleistalen van Furlo Pietralata

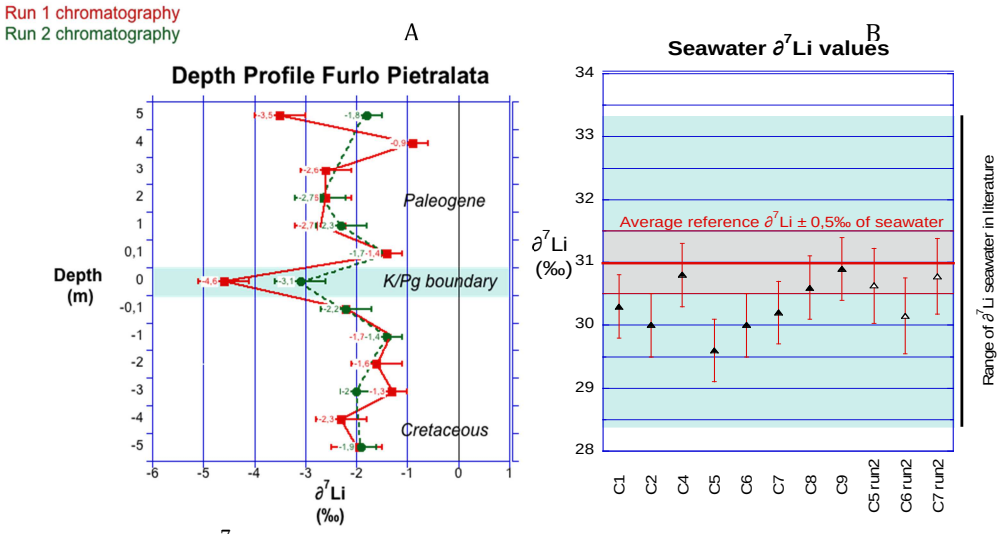

Figuur 2 (A) ∂^{7}Li waardes in functie van de diepte binnen de sequentie. De weergeven precisie is twee keer de standaard afwijking, (B) ∂^{7}Li waardes voor Sargasso zeewaterstalen per individuele kolom Gevulde driehoeken zijn van een eerste chromatografische scheiding, open driehoeken zijn van een additionele chromatografische scheiding.

De kleistalen van het Krijt en Paleogeen vertoonden een ∂^{7}Li waarde tussen -1.3 en -2.3 ± 0,5 ‰, en, tussen -0,9 en -3,5 ‰ ± 0,5 ‰, respectievelijk. Een waarde van 0 ±2 ‰ wordt aangenomen voor de continentale korst[4,18]. Figuur 2 (A) vertoont een negatieve piek in de ∂^{7}Li waarde exact op de K/Pg grens voor beide duplicaatmetingen. De resultaten van deze duplicaatmetingen op de grens verschillen significant van elkaar. Tot op heden is er geen verklaring voor dit verschil. In sommige stalen werd een verhoogde hoeveelheid Na teruggevonden, maar deze was altijd onder de tolereerbare concentratie van 5000 µg/l. In de post-elutie fractie van P1 werd minder dan 1 % van de opgebrachte hoeveelheid Li teruggevonden. Het vertoonde P1 signaal zou dus in werkelijkheid meer negatief kunnen zijn. Alle andere metingen vertoonden wel een gelijkaardige waarde tussen de duplicaatmetingen.

De negatieve ∂^{7}Li shift exact op de K/Pg grens is verondersteld het gevolg te zijn van verhoogde verweringsprocessen. Deze verhoogde verwering en de extra-terrestrische impact zijn van dezelfde ouderdom, zoals aangetoond door de Ir anomalie gevonden in de kleistalen van Goderis (2013) [12]. Zoals omschreven in §1b., zou de impact een

langdurige duisternis hebben veroorzaakt, die aanleiding gaf tot ontbossing en daling van de hoeveelheid planten. Deze daling van vegetatie in combinatie met zure regen kon aanleiding geven tot verhoogde uitspoeling van ^{7}Li uit sedimenten en zou een verklaring bieden voor de negatieve ∂^{7}Li shift.
Hierdoor kunnen onze resultaten een ondersteuning bieden aan de reeds bestaande hypothese van veranderende klimatologische omstandigheden op de K/Pg grens, specifieker: de langdurige duisternis, zure regen en intensievere verwering[7,8,16].

4. Samenvatting

Een methode werd ontwikkeld om de isotopische samenstelling van Li in laag geconcentreerde oplossingen van ~50 µg/l te bepalen via MC-ICP-MS. Deze methode werd vervolgens toegepast op de analyse van kleistalen van op en rond de K/Pg grens. De kleistalen werden geïsoleerd uit hun kalksteenmatrix en succesvol gedigesteerd. Vervolgens werd Li via kationenuitwisselingschromatografie geïsoleerd. Een succesvolle chromatografische scheiding van Li uit kleimatrix werd bereikt met monstervolumes tussen 22 µl en 108 µl, die 50 ng lithium bevatten. De kalibratie vertoonde een scheiding van 1,5 ml tussen de Li en de Na piek. Sargasso zeewaterstalen werden ter validatie geanalyseerd vermits ze kunnen worden beschouwd als een worst case scenario voor de kleistalen, vanwege hun zware matrix. De voor deze zeewaterstalen verkregen ∂^{7}Li waarden bleken onderling consistent binnen 2 ‰ en vertonen een goede overeenkomst met de referentiewaarde voor zeewater. De invloed van Na op de Li isotopenverhouding werd geëvalueerd. Tot en met een concentratie van 5000 µg/l Na wordt geen afwijkend signaal gevonden voor een 50 µg/l lithium oplossing.
Een diepteprofiel rond de K/Pg grens werd opgesteld. Dit diepteprofiel vertoont een negatieve ∂^{7}Li shift exact op de K/Pg grens. Een mogelijke verklaring voor deze negatieve shift is een meer intense continentale verwering ten gevolge van de verdwijning van vegetatie in combinatie met zure regen ten gevolge van de impact van de Chicxulub projectiel.

5.Dankwoord

Een dankwoord aan Joke Belza en Claudio Venturi voor het voorzien van de stalen,
Een dankwoord aan het FWO project en het Bijzonder Onderzoeksfonds (BOF Ugent).

Referenties

[1] P. B. Tomascak, “Developments in the understanding and application of lithium isotopes in the earth and planetary sciences,” *Mineralogy & geochemistry*, vol. 55, pp. 153–195, 2004.

[2] K. W. Burton and N. Vigier, “Lithium Isotopes as Tracers in Marine and Terrestrial Environments,” in *Handbook of environmental isotope geochemistry*, M. Baskaran, Ed. 2011, pp. 41–59.

[3] H. R. Marschall, P. a. E. Pogge von Strandmann, H.-M. Seitz, T. Elliott, and Y. Niu, “The lithium isotopic composition of orogenic eclogites and deep subducted slabs,” *Earth and Planetary Science Letters*, vol. 262, pp. 563–580, 2007.

[4] R. L. Rudnick, P. B. Tomascak, H. B. Njo, and L. R. Gardner, “Extreme lithium isotopic fractionation during continental weathering revealed in saprolites from South Carolina,” *Chemical Geology*, vol. 212, pp. 45–57, 2004.

[5] C.-F. You and L.-H. Chan, “Precise determination of lithium isotopic composition in low concentration natural samples,” *Geochimica et Cosmochimica Acta*, vol. 60, pp. 909–915, 1996.

[6] S. Misra and P. N. Froelich, “Lithium isotope history of Cenozoic seawater: changes in silicate weathering and reverse weathering.,” *Science*, vol. 335, pp. 818–23, 2012.

[7] L. W. Alvarez, W. Alvarez, F. Asaro, and V. A. Helen, “Extraterrestrial Cause for the Cretaceous-Tertiary Extinct tion Experimental results and theoretical interpretation,” *Science*, vol. 208, pp. 1095–1108, 1980.

[8] P. Schulte, L. Alegret, I. Arenillas, J. a Arz, P. J. Barton, P. R. Bown, T. J. Bralower, G. L. Christeson, P. Claeys, C. S. Cockell, G. S. Collins, A. Deutsch, T. J. Goldin, K. Goto, J. M. Grajales-Nishimura, R. a F. Grieve, S. P. S. Gulick, K. R. Johnson, W. Kiessling, C. Koeberl, D. a Kring, K. G. MacLeod, T. Matsui, J. Melosh, A. Montanari, J. V Morgan, C. R. Neal, D. J. Nichols, R. D. Norris, E. Pierazzo, G. Ravizza, M. Rebolledo-Vieyra, W. U. Reimold, E. Robin, T. Salge, R. P. Speijer, A. R. Sweet, J. Urrutia-Fucugauchi, V. Vajda, M. T. Whalen, and P. S. Willumsen, “The Chicxulub asteroid impact and mass extinction at the Cretaceous-Paleogene boundary.,” *Science*, vol. 327, pp. 1214–8, 2010.

[9] A. Montanari and C. Koeberl, *Impact Stratigraphy The Italian Record*. 2000.

[10] A. R. Hildebrand, G. T. Penfield, D. A. Kring, M. Pilkington, A. C. Z, B. Stein, W. V Boynton, and S. B. Jacobsen, “Geology Chicxulub Crater : A possible Cretaceous / Tertiary boundary impact crater on the Chicxulub Crater : A possible Cretaceous / Tertiary boundary impact crater on the Yucatán Peninsula , Mexico,” *geological society of America*, 1991.

[11] P. Claeys and S. Goderis, “Lethal Billiards,” *Nature*, vol. 449, pp. 30–31, 2007.

[12] S. Goderis, “Reevalution of siderophile abundances and ratios across the Cretaceous-Paleogene (K-PG) boundary: Implications for the nature of the projectile,” *In press*, 2013.

[13] W. F. Bottke, D. Vokrouhlický, and D. Nesvorný, “An asteroid breakup 160 Myr ago as the probable source of the K/T impactor.,” *Nature*, vol. 449, pp. 48–53, 2007.

[14] V. Reddy, J. A. Sanchez, W. F. Bottke, M. J. Gaffey, L. Le Corre, J. Masiero, and A. K. Mainzer, “Composition of (1696) Nurmela: The second largest member of Baptistina Asteroid Family,” *44th Lunar and Planetary Science Conference*, p. 1093, 2013.

[15] A. Montanari and C. Koeberl, “Important Distal Ejecta Layers and Their Source Craters,” in *Impact Stratigraphy The Italian Record*, 2000, pp. 102–158.

[16] J. Smit, “Meteorite impact, extinctions and the Cretaceous-Tertiary Boundary*,” *Geologie en Mijnbouw*, vol. 69, pp. 187–204, 1990.

[17] R. H. James and M. R. Palmer, “The lithium isotope composition of international rock standards,” *Chemical Geology*, vol. 166, pp. 319–326, 2000.

[18] S. Misra and P. N. Froelich, “Measurement of lithium isotope ratios by quadrupole-ICP-MS: application to seawater and natural carbonates,” *Journal of Analytical Atomic Spectrometry*, vol. 24, p. 1524, 2009.

[19] T. I. Taylor and H. C. Urey, “Fractionation of the Lithium and Potassium Isotopes by Chemical Exchnge with Zeolites,” *Journal of chemical physics*, vol. 6, pp. 429–438, 1938.

[20] P. Claeys and W. Kiessling, “Distribution of Chicxulub ejecta at the Cretaceous-Tertiary boundary,” *geological Society of America*, pp. 55–68, 2002.

[21] W. Rieman and H. F. Walton, “Ion exchange in analytical chemistry,” *Analytical Chemistry*, p. 295, 1970.

[22] D. C. Gregoire, B. M. Acheson, and R. P. Taylor, “Measurement of lithium isotope ratios by inductively coupled plasma mass spectrometry: Application to geological materials,” *Journal of Analytical Atomic Spectrometry*, vol. 11, pp. 765–772, 1996.

9. Annex per chapter

9.1. Chapter 1: introduction and aim.

/

9.2. Chapter 2: Instrumentation.

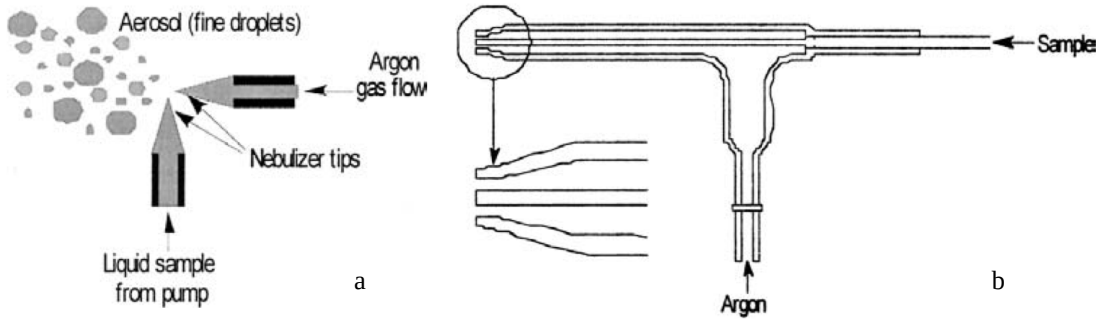

Figure 9-1 from [88]: (a) cross flow nebulizer, (b) concentric nebulizer

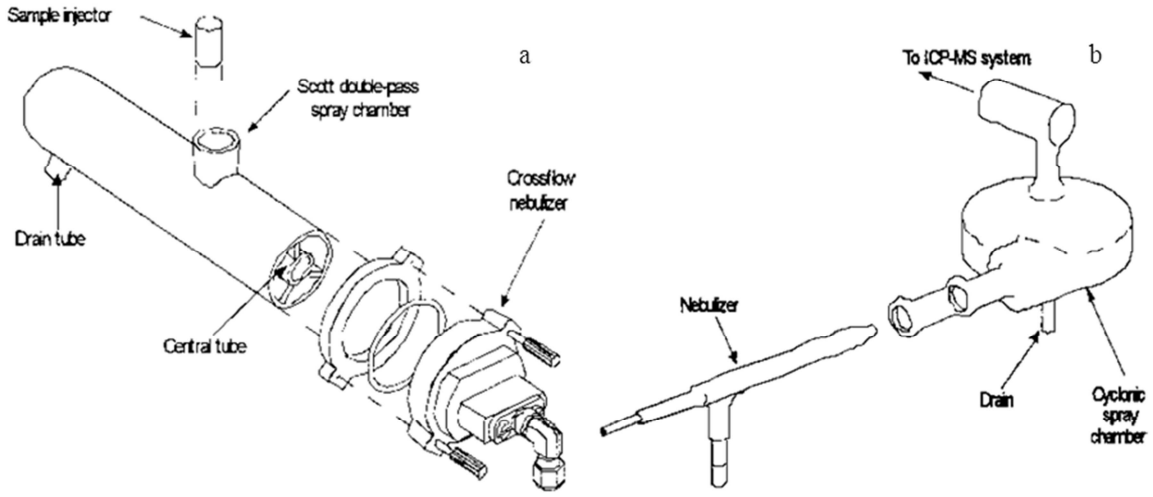

Figure 9-2 figures from [88]: (a) Scott double-pass Scott-type spray chamber, (b) cyclonic spray chamber.

Table 9-1: Neptune MC-ICP-MS instrument settings used during this work. Specific parameter settings of the Neptune are also described per experiment further in this chapter.

Neptune – general

Instrument parameter	Setting
Plasma RF forward Power *	1284 -1296 W
Nebullizer	Micro-concentric (quartz)
Sample uptake rate	100 µl/min
Uptake time sample & standard	120 s
Uptake time blank	90 s
Washout time	30 s
Spray chamber	High-stability unit (cyclonic + Scott-type)
Spray chamber temperature	Room temperature
Torch/Injector	Quartz/Quartz
Shield torch	Platinum
Sampling cone/Skimmer cone	Nickel (1,1 mm)/Nickel (0,8 mm)
X position *	3.4 - 3.9 mm
Y position *	-1.7 - -2.9 mm
Z position *	0.4 - 1.0 mm
Cool gas flow rate	15.5 l/min
Auxilary gas flow rate	0.6 - 0.7 l/min
Sample gas flow rate	1.0 - 1.1 l/min
Integration time	4.194 s
Idle time	3 s
Cup position	
L4	^{6}Li
H4	^{7}Li
Central cup	6.526

* optimized daily for highest signal-to-noise ratio.

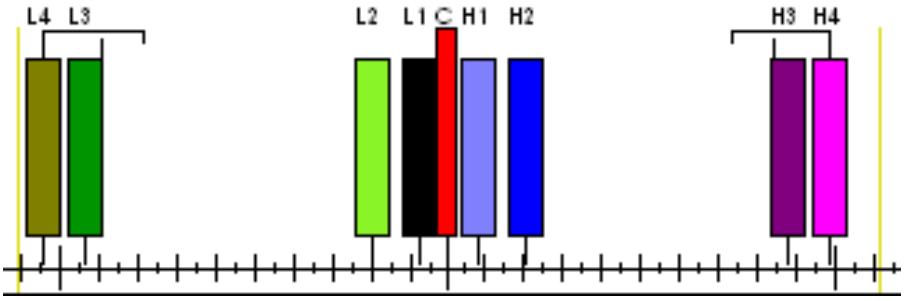

Figure 9-3: cup configuration of MC-ICP-MS. ^{6}Li was measured on position L4. ^{7}Li was measured on position H4.

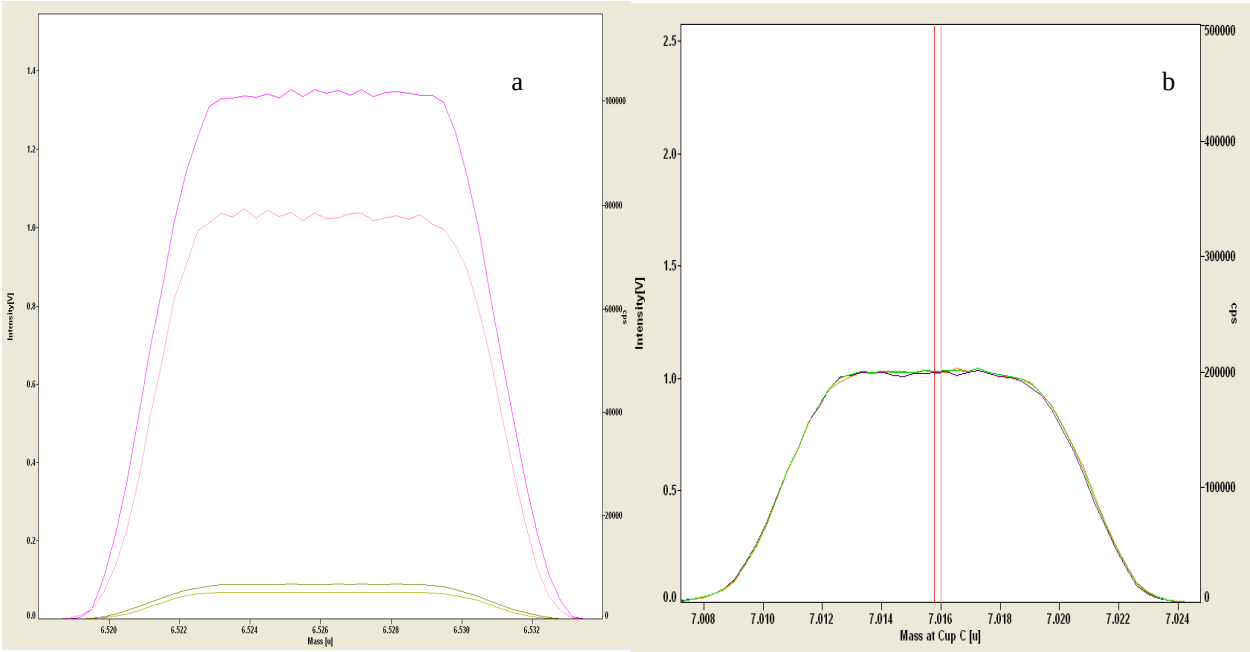

Figure 9-4:Example of: (a) peakscan. Pink signal is the ^{7}Li signal; green signal is the ^{6}Li signal, (b) Peak center.

The intensity and smoothness of the measured signals was verified via a peak scan. Via “Peakcenter” the cups were positioned in the perfect position for measurements of the ion beam intensities of the analyte isotopes.

Table 9-2: X-Series II Q-ICP-MS instrument settings used during this work. Specific parameter settings are also described per experiment further in this chapter.

X series II General

Instrument parameter	Setting
Plasma RF forward Power *	1200 W
Nebullizer	concentric (quartz)
Sample uptake rate	500 µl/min
Uptake time	80 s
Washout time	90 s
Spray chamber	Double-pass Scott-type
Spray chamber temperature	1°C
Torch/Injector	Quartz/quartz
Shield torch	Platinum
Sampling cone / orifice diameter	Nickel/1.1 mm
Skimmer cone / orifice diameter	Nickel/0.75 mm
Horizontal position*	83 - 90 mm
Vertical position*	400 -414 mm
Sampling depth *	104 - 111 mm
Cool gas flow rate *	13.0 l/min
Auxilary gas flow rate *	0.7 l/min
Nebuliser gas flow rate *	0.84 l/min
Dwell time	20 ms
Number of sweeps	200

* Optimized daily for maximum signal-to-noise ratio.

Table 9-3: manufacturer threshold values that need to be achieved before measurements can be started.

Reference values ICP-OES

	Mn	**Pb**	**Pb**	**As**
Wavelength	257.610 nm	168.215 nm	220.351 nm	189.042 nm
BEC	< 0.018 mg/l	< 0.4 mg/l	< 0.5 mg/l	< 0.31 mg/l
Background	> 5,500 cps	> 1,200 cps	> 4,000 cps	> 1,700 cps
Intensity	> 70,000 cps	> 12,000 cps	> 22,000cps	> 15,000 cps
RSD % BG	≤ 1.0 %	≤ 1.8 %	≤ 1.0 %	≤ 1.5 %
RSD % Int.	≤ 0.7 %	≤ 1.0	≤ 1.0 %	≤ 0.7 %

9.3. Chapter 3: Reagents and standards

/

9.4. Chapter 4: Description of K/Pg boundary samples and optimization of isolation and digestion of clay fraction.

Figure 9-5: Picture of clay layer from the FDO site.

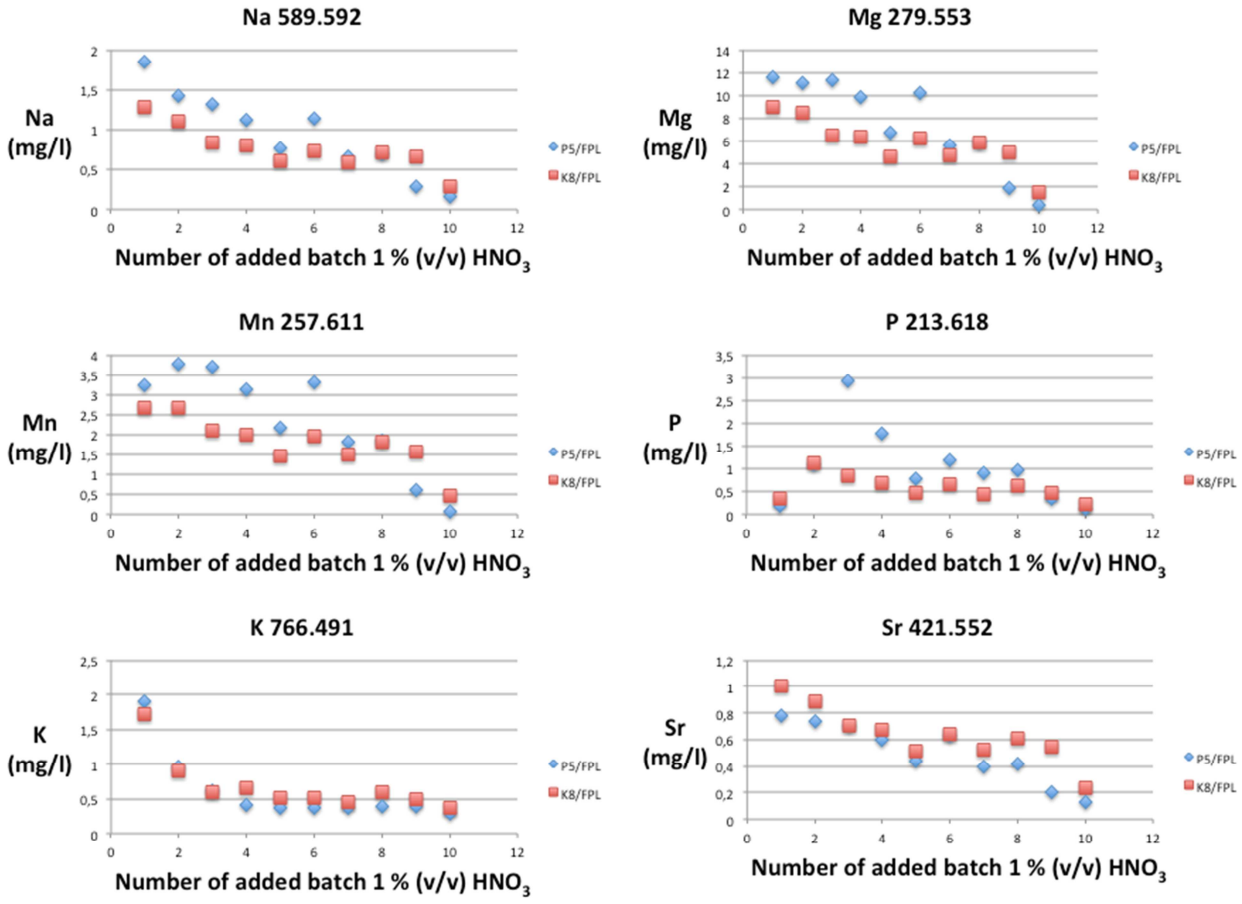

Figure 9-6: Leaching profiles of Na, Mg, Mn, P, K, Sr for the samples P5/FPL and K8/FPL. The emission line chosen for measurement via ICP-OES is mentioned in the title of each leaching profile cf. §4.3.3.

Table 9-4: ICP-OES instrument settings . corresponding to the results discussed in §4.3.3.

Chemical Composition of the clays by ICP-OES

Instrument parameter	**setting**
Plasma RF forward Power *	1400 W
Nebullizer	Cross-flow (quartz)
Sample uptake rate	1 ml/min
Uptake time	90 s
Washout time	90 s
Spray chamber	double-pass Scott-type
Spray chamber temperature	Room temperature
Torch/Injector	Quartz/Quartz
Shield torch	Platinum
Coolant gas flow rate *	12 l/min
Auxilary gas flow rate	0.8 l/min
Nebulizer gas flow rate *	0.84 l/min
Emmision line (nm)	§ 4.3.3.

* optimized daily according to Table 9-3

Table 9-5: ICP-QMS instrument settings corresponding to the results discussed in §4.3.3.

Chemical Composition of the Clays by Q-ICP-MS

Instrument parameter	Setting
Plasma RF forward Power *	1200 W
Nebullizer	Concentric (quartz)
Sample uptake rate	500 µl/min
Uptake time	80 s
Washout time	90 s
Spray chamber	Double-pass Scott-type
Spray chamber temperature	1°C
Torch/Injector	Quartz/Quartz
Shield torch	Platinum
Sampling cone/orifice	Nickel/1.1 mm
Skimmer cone/orifice	Nickel/0.75 mm
Horizontal position *	83 mm
Vertical position *	414 mm
Sampling depth *	104 mm
Cool gas flow rate *	13.0 l/min
Auxilary gas flow rate *	0.7 l/min
Nebuliser gas flow rate *	0.84 l/min
Dwell time	20 ms
Sweeps	200

* optimized daily to check whether the threshold values, set by manufacturer, concerning background, oxides and doubly charged species, were met.

9.5. Chapter 5: Optimization of lithium isotopic analysis by MC-ICP-MS

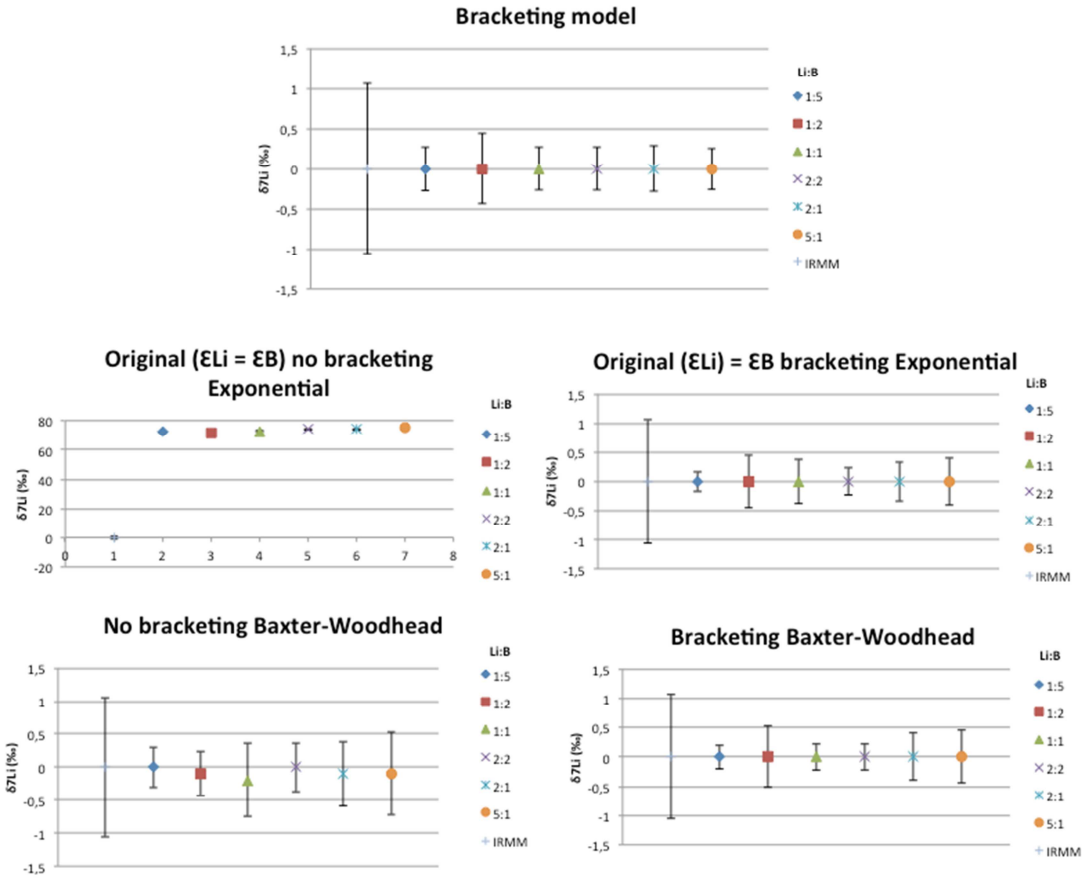

Figure 9-7: Graphical representation of the results obtained via the various correction models tested, as described in § 5.2. See also Figure 9-8.

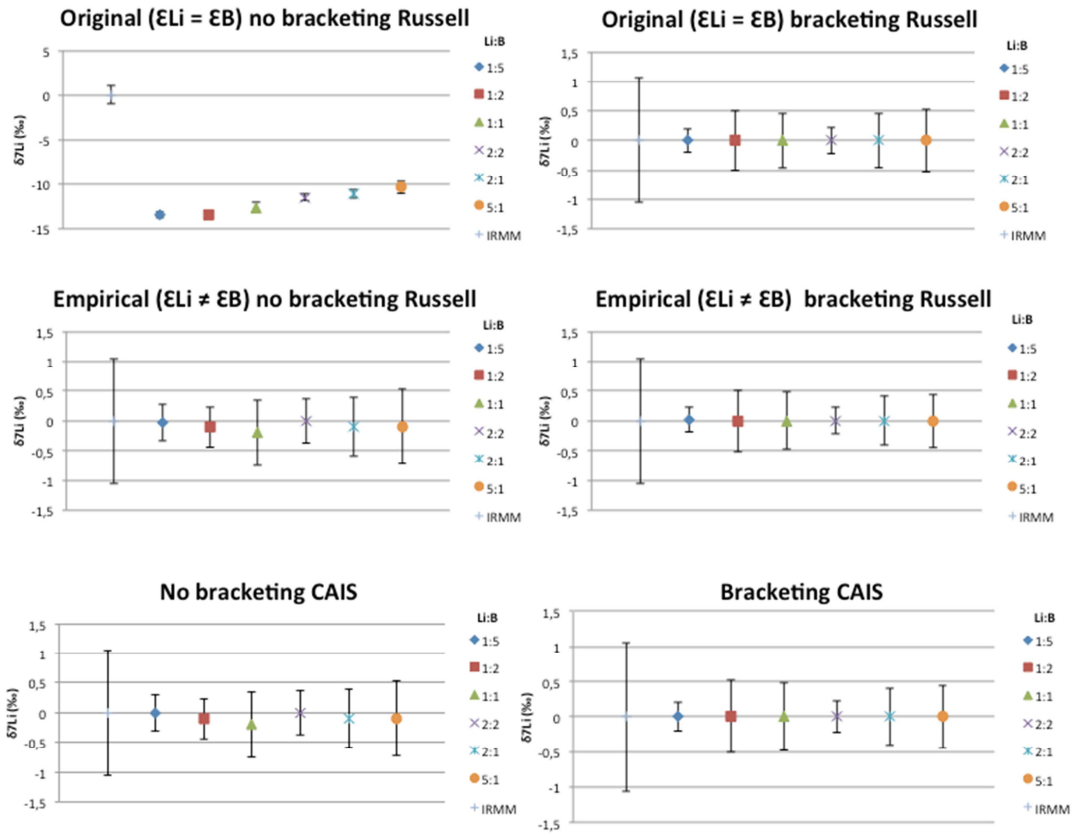

Figure 9-8: continuation of graphical represenatton of the results obtained via the various correction models tested, as described in § 5.2.

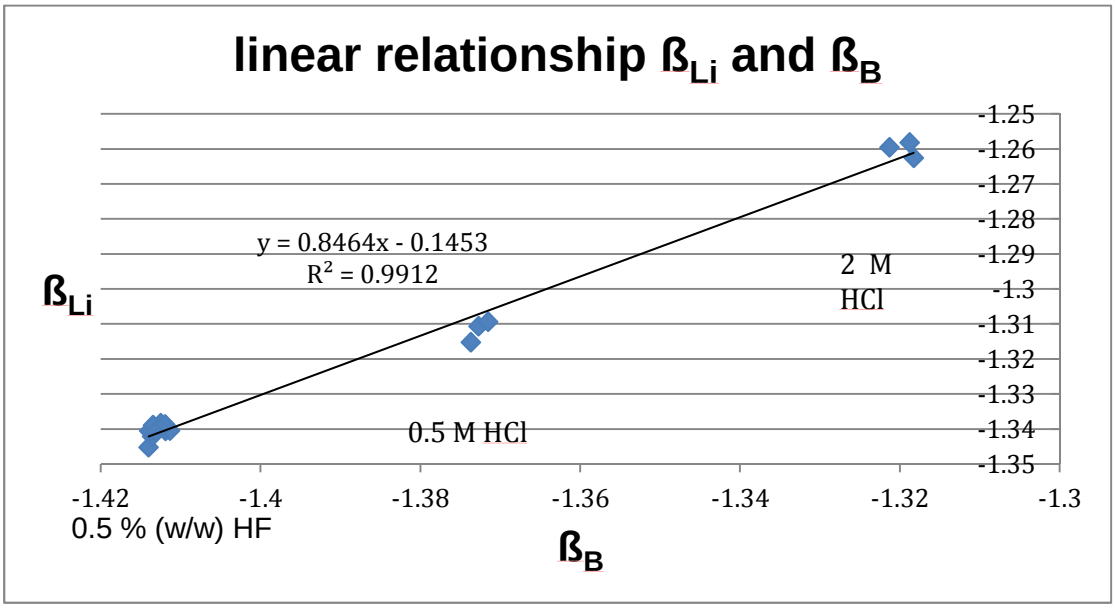

Figure 9-9: example of linear relationship between mass discrimination factors of Li and B established in the context of the empirical Russell law, relied on for internal correction type II.

Table 9-6: MC-ICP-MS settings used during correction model measurements. The corresponding results are discussed in §5.2.3.

Testing of Correction Models by MC-ICP-MS

Instrument parameter	**Setting**
Plasma RF forward Power	1284.0 W
Nebulizer	Micro-concentric (quartz)
Sample uptake rate	100 µl/min
Uptake time sample & standard	120 s
Uptake time blank	90 s
Washout time	30 s
Spray chamber	High-stability unit (cyclonic + Scott-type)
Spray chamber temperature	Room temperature
Torch/Injector	Quartz/Quartz
Shield torch	Platinum
Sampling cone/Orifice	Nickel/1.1 mm
Skimmer cone/Orifice	Nickel/0.8 mm
X position	3.7
Y position	-1.7
Z position	1.0
Cool gas flow rate	15.5 l/min
Auxilary gas flow rate	0.7 l/min
Sample gas flow rate	1.1 l/min
Integration time	4.194 s
Idle time	3 s
Cup position	
L4	^{6}Li
H4	^{7}Li
Central cup	m/z = 6.526
L4	^{10}B
H4	^{11}B

Table 9-7: MC-ICP-MS settings used during amplifier test measurements by MC-ICP-MS. The corresponding esults are discussed in §5.3.2.

Amplifier Test by MC-ICP-MS

Instrument parameter	**Setting**
Plasma RF forward Power	1296.2 W
Nebulizer	Micro-concentric (quartz)
Sample uptake rate	100 µl/min
Uptake time sample & standard	120 s
Uptake time blank	90 s
Washout time	30 s
Spray chamber	High-stability unit (cyclonic + Scott-type)
Spray chamber temperature	Room temperature
Torch/Injector	Quartz/Quartz
Shield torch	Platinum
Sampling cone/Orifice	Nickel/1.1 mm
Skimmer cone/Orifice	Nickel/0.8 mm
X position	3.4
Y position	-2.3
Z position	0.9
Cool gas flow rate	15.5 l/min
Auxilary gas flow rate	0.6 l/min
Sample gas flow rate	1.0 l/min
Integration time	4.194 s
Idle time	3 s
Cup position	
L4	^{6}Li
H4	^{7}Li
Central cup	m/z = 6.526

Table 9-8: MC-ICP-MS settings used during sodium tolerance test measurements by MC-ICP-MS. The corresponding results are discussed in §5.4.2.

Sodium Tolerance Test by MC-ICP-MS

Instrument parameter	**Setting**
Plasma RF forward Power	1286.0 W
Nebulizer	Micro-concentric (quartz)
Sample uptake rate	100 µl/min
Uptake time sample & standard	120 s
Uptake time blank	90 s
Washout time	30 s
Spray chamber	High-stability unit (cyclonic + Scott-type)
Spray chamber temperature	Room temperature
Torch/injector	Quartz/quartz
Shield torch	Platinum
Sampling cone/Orifice	Nickel/1.1 mm
Skimmer cone/Orifice	Nickel/0.8 mm
X position	3.6
Y position	-2.5
Z position	0.6
Cool gas flow rate	15.5 l/min
Auxilary gas flow rate	0.6 l/min
Sample gas flow rate	1.0 l/min
Integration time	4.194
Idle time	3 s
Cup position	
L4	^{6}Li
H4	^{7}Li
Central cup	m/z = 6.526

9.6. Chapter 6: Column Chromatography

Cation	0.1	0.2	0.5	1.0	2.0	3.0	4.0
ZrO^{+2}	$>10^5$	$>10^5$	$\sim10^5$	7250	489	61	14.5
Th^{+4}	$>10^5$	$>10^5$	$\sim10^5$	2049	239	114	67
La^{+3}	$>10^5$	10^5	2480	265.1	48	18.8	10.4
Ce^{+3}	$>10^5$	10^5	2460	264.8	48	18.8	10.5
Y^{+3}	$>10^5$	$>10^4$	1460	144.6	29.7	13.6	8.6
Ba^{+2}	$>10^4$	2930	590	126.9	36	18.5	11.9
Hg^{+} [a]	$>10^4$	7600	640	94.2	33	19.2	13.6
Al^{+3}	8200	1900	318	60.8	12.5	4.7	2.8
Sr^{+2}	4700	1070	217	60.2	17.8	10.0	7.5
Ga^{+3}	$>10^4$	3036	260	42.58	7.75	3.2	0.36
Ca^{+2}	3200	790	151	42.29	12.2	7.3	5.0
Pb^{+2} [a]	$>10^4$	1420	183	35.66	9.8	6.8	4.5
Fe^{+3}	9000	3400	225	35.45	5.2	3.6	2.0
Cr^{+3}	1130	262	73	26.69[b]	7.9	4.8	2.7
Tl^{+} [a]	173	91	41	22.32	9.9	5.8	3.3
Ni^{+2}	1600	450	70	21.85	7.2	4.7	3.1
Co^{+2}	1650	460	72	21.29	6.7	4.2	3.0
Mg^{+2}	1720	530	88	20.99	6.2	3.5	3.5
Mn^{+2}	2230	610	84	20.17	6.0	3.9	2.5
Fe^{+2}	1820	370	66	19.77	4.1	2.7	1.8
Cs^{+1}	182	99	44	19.41	10.4	...	...
UO_2^{+2}	5460	860	102	19.20	7.3	4.9	3.3
Ag^{+} [a]	156	83	35	18.08	7.9	5.4	4.0
Cu^{+2}	1510	420	65	17.50	4.3	2.8	1.8
Hg^{+2} [a]	4700	1090	121	16.85	5.9	3.9	2.8
Zn^{+2}	1850	510	64	16.03	3.7	2.4	1.6
Rb^{+}	120	72	33	15.43	8.1	...	...
K^{+}	106	64	29	13.87	7.4	...	...
Be^{+2}	255	117	42	13.33	5.2	3.3	2.4
Ti^{+4}	$>10^4$	297	39	11.86	3.7	2.4	1.7
V^{+4}		230	44	7.20	...	...	...
Na^{+}	52	28.3	12	5.59	3.6	...	...
Li^{+}	33	18.9	8.1	3.83	2.5	...	...
Sn^{+4}	$\sim10^4$	45	6.2	1.60	1.2	...	...
Cd^{+2}	510	84	6.5	1.54	1.0	0.6	...
V^{+5}	13.9	7.0	5.0	1.10	0.7	0.2	0.3
Mo^{+5}	10.9	4.5	0.3	0.81	0.2	0.4	0.3
Se^{+4}	1.1	0.6	0.8	0.63	1.0	...	0.7
Bi^{+3}	Ppt.	Ppt.	<1.0	1.0	1.0	1.0	1.0
As^{+3}	1.4	1.6	2.2	3.81	2.2	...	...
Sb^{+3}	Ppt.	Ppt.	Ppt.	Ppt.	2.8	...	...
Pt^{+4}	...	...	...	1.4	...	...	...
Au^{+3}	0.5	0.1	0.4	0.84	1.0	0.7	0.2
Hg^{+2}	1.6	0.9	0.5	0.28	0.3	0.2	0.2

[a] Done in nitric acid.
[b] More than one cationic species present.

Figure 9-10: original data from Strelow (1960) [70]. Kd values of different cations as a function of different normalities of HCl

Cation	0.1*N*	0.2*N*	0.5*N*	1.0*N*	2.0*N*	3.0*N*	4.0*N*
Zr(IV)[a]	>10⁴	>10⁴	>10⁴	6500	652	112	30.7
Hf(IV)	>10⁴	>10⁴	>10⁴	2400	166	61	20.8
Th(IV)	>10⁴	>10⁴	>10⁴	1180	123	43.0	24.8
La(III)[a]	>10⁴	>10⁴	1870	267	47.3	17.1	9.1
Ce(III)[a]	>10⁴	>10⁴	1840	246	44.2	15.4	8.2
Yb(III)	>10⁴	>10⁴	1150	193	41.3	16.0	9.0
Er(III)	>10⁴	>10⁴	1100	182	38.2	14.9	8.0
Y(III)[a]	>10⁴	>10⁴	1020	174	35.8	13.9	10.0
Sm(III)	>10⁴	>10⁴	1000	168	29.8	10.9	7.2
Gd(III)	>10⁴	>10⁴	1000	167	29.2	10.8	6.9
In(III)	>10⁴	>10⁴	680	118	23.0	10.1	5.8
Sc(III)	>10⁴	3300	500	116	23.3	11.6	7.6
Cr(III)	5100	1620	418	112	27.8	19.2	10.9
Hg(I)[a]	>10⁴	7600	640	94	33.5	19.2	13.6
Ga(III)	>10⁴	4200	445	94	20.0	9.0	5.8
Al(III)[a]	>10⁴	3900	392	79	16.5	8.0	5.4
Fe(III)[a]	>10⁴	4100	362	74	14.3	6.2	3.1
Ba(II)[a]	5000	1560	271	68	13.0	6.0	3.6
Sr(II)[a]	3100	775	146	39.2	8.8	6.1	4.7
Pb(II)[a]	>10⁴	1420	183	35.7	8.5	5.5	4.5
Ca(II)[a]	1450	480	113	35.3	9.7	4.3	1.8
Cd(II)[a]	1500	392	91	32.8	10.8	6.8	3.4
Co(II)[a]	1260	392	91	28.8	10.1	6.1	4.7
Mn(II)[a]	1240	389	89	28.4	11.4	7.1	3.0
Ni(II)[a]	1140	384	91	28.1	10.3	8.6	7.3
Cu(II)[a]	1080	356	84	26.8	8.6	4.8	3.1
Zn(II)[a]	1020	352	83	25.2	7.5	4.6	3.6
Bi(III)	893	305	79	25.0	7.9	3.7	3.0
U(VI)	659	262	69	24.4	10.7	7.4	6.6
Mg(II)[a]	794	295	71	22.9	9.1	5.8	4.1
Tl(I)[a]	173	91	41.0	22.3	9.9	5.8	3.3
Ag(I)[a]	156	86	36.0	18.1	7.9	5.4	4.0
Hg(II)[a]	4700	1090	121	16.9	5.9	3.9	2.8
Cs(I)	148	81	34.8	16.8	7.6	4.7	3.4
Be(II)[a]	553	183	52	14.8	6.6	4.5	3.1
Ti(IV)[a]	1410	461	71	14.6	6.5	4.5	3.4
V(IV)	495	157	35.6	14.0	4.7	3.0	2.5
Rb(I)	118	68	29.1	13.4	6.6	4.1	2.9
K(I)	99	59	26.2	11.4	5.7	3.5	2.6
Te(IV)[b]	40.3	19.7	8.5	5.0	2.4	0.6	0.2
Pd(II)	97	62	23.5	9.1	3.4	2.7	2.5
Rh(III)	78	44.7	19.5	7.8	4.1	2.1	1.0
Na(I)	54	29.4	12.7	6.3	3.4	2.0	1.3
Li(I)	33.1	18.6	8.0	3.9	2.6	1.7	1.1
V(V)	20.0	10.9	4.9	2.0	1.2	0.8	0.5
Mo(VI)	Ppt.	5.2	2.9	1.6	1.0	0.8	0.6
Nb(V)	11.6	6.3	0.9	0.2	0.1	0.1	0.1
Se(IV)	<0.5	<0.5	<0.5	<0.5	<0.5	<0.5	<0.5
As(III)	<0.1	<0.1	<0.1	<0.1	<0.1	<0.1	<0.1

[a] Coefficients published previously but included to provide complete list.
[b] Determined at $q = 0.2$ because of limited solubility at low acid concentrations.

Figure 9-11 original data from Strelow et al. (1965) [79]. Kd values of different cations in function of different normalities HNO_3

9.7. Chapter 7: Analysis of the Furlo Pietralata clay fraction of the samples.

Table 9-9 MC-ICP-MS settings used during clay sample measurements by MC-ICP-MS. The corresponding results are discussed in §7.2.

	NEPTUNE 09/04	*NEPTUNE 10/04*

Instrument parameter	**Setting**	
Plasma RF forward Power	1287.9 W	1289.9 W
Nebulizer	Micro-concentric (quartz)	Micro-concentric (quartz)
Sample uptake rate	100 µl/min	100 µl/min
Uptake time sample & standard	120 s	120 s
Uptake time blank	90 s	90 s
Washout time	30 s	30 s
Spray chamber	High-stability unit (cyclonic + Scott-type)	High-stability unit (cyclonic + Scott-type)
Spray chamber temperature	Room temperature	Room temperature
Torch/injector	Quartz/quartz	Quartz/quartz
Shield torch	Platinum	Platinum
Sampling cone/orifice	Nickel/1.1 mm	Nickel/1.1 mm
Skimmer cone/orifice	Nickel/0.8 mm	Nickel/0.8 mm
X position	3.7	3.9
Y position	-2.7	-2.8
Z position	0.6	0.4
Cool gas flow rate	15.5 l/min	15.5 l/min
Auxilary gas flow rate	0.6 l/min	0.6 l/min
Sample gas flow rate	1.0 l/min	1.0 l/min
Integration time	4.194 s	4.194 s
Idle time	3 s	3 s
Cup position		
L4	^{6}Li	^{6}Li
H4	^{7}Li	^{7}Li
Central cup	m/z = 6.526	m/z = 6.526

. Table 9-10: Results for the bracketing standards, which were treated as samples during measurement of the clay samples by MC-ICP-MS.

Standards measured as samples		
	09/04	10/04
	∂7LI (‰)	**∂7LI (‰)**
brac A	-0.3 ± 0.5	-0.1 ± 0.4
Brac B	0.0 ± 0.5	0.2 ± 0.4
brac C	0.0 ± 0.5	-0.2 ± 0.4
brac D	0.6 ±0.0	0.1 ± 0.4
brac E	0.0 ± 0.5	-0.1 ± 0.4
brac F	0.0 ± 0.5	0.1 ± 0.4
brac G	0.0 ± 0.5	-0.1 ± 0.4
brac H	0.0 ± 0.5	-0.1 ± 0.4
IRMM	0.0 ± 1,1	0.0 ± 1,1

Table 9-11 Sequence of measurements of the clay samples by MC-ICP-MS. G samples are samples from an another research (not described in this thesis).

Sequence Neptune 09/04						
Sequence number	1	2	3	4	5	6
Sample name	P1E2	K9E2	F3E2	Brac A	Brac B	Brac C
Sequence number	7	8	9	10	11	12
Sample name	P5E2	K11E2	F1E2	Brac D	K7E2	P4B2
Sequence number	13	14	15	16	17	18
Sample name	F2E2	Brac E	Brac F	Brac G	P4E2	F1B2
Sequence number	19	20	21	22	23	24
Sample name	P3E2	Brac H	F3B2	F2B2	P5B2	K7B2

Sequence Neptune 10/04						
Sequence number	1	2	3	4	5	6
Sample name	K12E2	K8E2	P1B2	Brac A	Brac B	Brac C
Sequence number	7	8	9	10	11	12
Sample name	K10E2	P6E2	P2E2	Brac D	K10B2	K12B2
Sequence number	13	14	15	16	17	18
Sample name	K8B2	Brac E	Brac F	Brac G	P6B2	G5E2
Sequence number	19	20	21	22	23	24
Sample name	G2E2	Brac H	G7E2	G6E2	G3E2	G8E2

Table 9-12: Q-ICP-MS settings used during elemental analysis of the pre-,lithium-,post-elution fractions. The corresponding results are discussed in §7.2.2.

Pre-, Lithium and Post-Elution Fraction Determination

Instrument parameter	**Setting**
Plasma RF forward Power	1200 W
Nebulizer	Concentric (quartz)
Sample uptake rate	500 µl/min
Uptake time	80 s
Wash time	90 s
Spray chamber	Double-pass Scott-type
Spray chamber temperature	1°C
Torch/Injector	Quartz/Quartz
Shield torch	Platinum
Sampling cone/Orifice	Nickel/1.1 mm
Skimmer cone/Orifice	Nickel/0.75 mm
Horizontal	90 mm
Vertical	400 mm
Sampling depth	111 mm
Cool gas flow rate	13.0 l/min
Auxilary gas flow rate	0.7 l/min
Nebuliser gas flow rate	0.84 l/min
Dwell time	20 ms
Sweeps	200

Table 9-13: Overview of the amount of lithium in the pre-, lithium-and post elution fractions of the different samples. In addition to the overview presented in §7.2.2.

Amount of Lithium

			Pre-elution		Lithium-elution		Post-Elution	
Sample	**Depth (m)**	**Load volume**	**Run 1 Li (ng)**	**Run 2 Li (ng)**	**Run 1 Li (ng)**	**Run 2 Li (ng)**	**Run 1 Li (ng)**	**Run 2 Li (ng)**
P1/FPL	5	50 µl	<LOQ	<LOQ	77	62	<LOQ	0.9
P2/FPL	4	50 µl	<LOQ	n.a.	62	n.a.	<LOQ	n.a.
P3/FPL	3	65 µl	<LOQ	n.a.	46	n.a.	<LOQ	n.a.
P4/FPL	2	82 µl	<LOQ	<LOQ	49	49	<LOQ	<LOQ
P5/FPL	1	107 µl	<LOQ	n.a.	48	47	<LOQ	<LOQ
P6/FPL	0.1	91 µl	<LOQ	<LOQ	47	47	<LOQ	<LOQ
F2/FPL	0	21µl	<LOQ	<LOQ	50	49	<LOQ	<LOQ
K7/FPL	-0.1	89 µl	<LOQ	<LOQ	48	47	<LOQ	<LOQ
K8/FPL	-1	85 µl	<LOQ	<LOQ	48	45	<LOQ	<LOQ
K9/FPL	-2	50 µl	<LOQ	n.a.	45	n.a.		
K10/FPL	-3	87 µl	<LOQ	<LOQ	47	46	<LOQ	<LOQ
K11/FPL	-4	84 µl	<LOQ	n.a.	48	n.a.	<LOQ	n.a.
K12/FPL	-5	57 µl	<LOQ	<LOQ	47	46	<LOQ	<LOQ
F1/PTL	0	21 µl	<LOQ	<LOQ	47	46	<LOQ	<LOQ
F3/FDO	0	22 µl	<LOQ	<LOQ	50	48	<LOQ	<LOQ

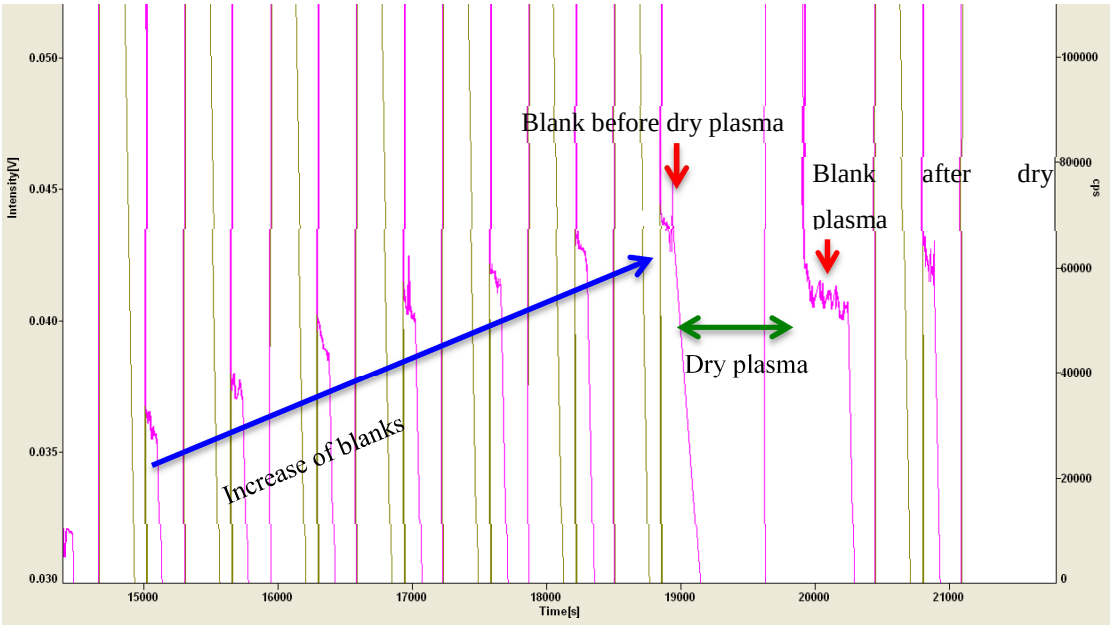

Figure 9-12: Effect of dry plasma on blanks, during measurement of samples on the MC-ICP-MS. The pink signal is the ^{7}Li signal; the green signal is the ^{6}Li signal. A decrease in the blank intensity is obtained after 10 minutes of dry plasma conditions.

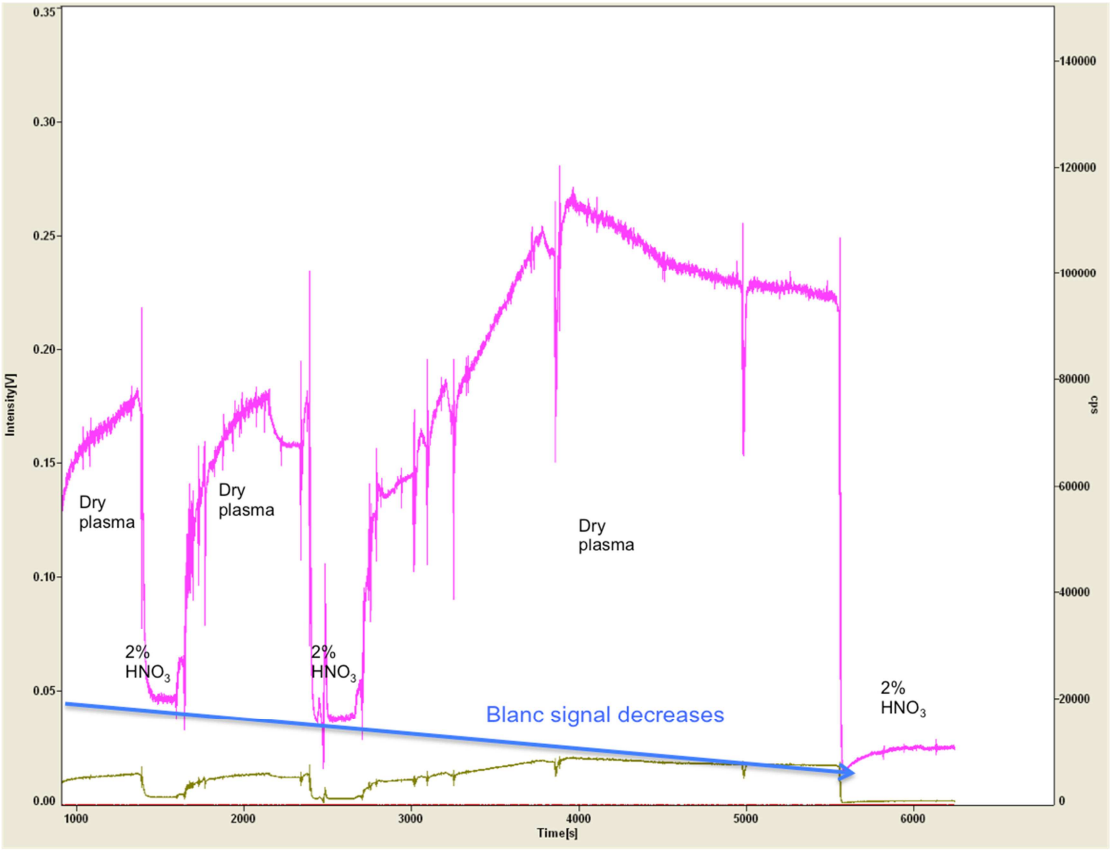

Figure 9-13 Effect of dry plasma on blanks. The pink signal is the ^{7}Li signal; the green signal is the ^{6}Li signal. A decrease in the blank intensity is observed after dry plasma conditions. During the operation of the plasma under dry plasma conditions, an increase in the signal intensity is observed for both isotopes.